FY09

Engineering Research & Technology Report

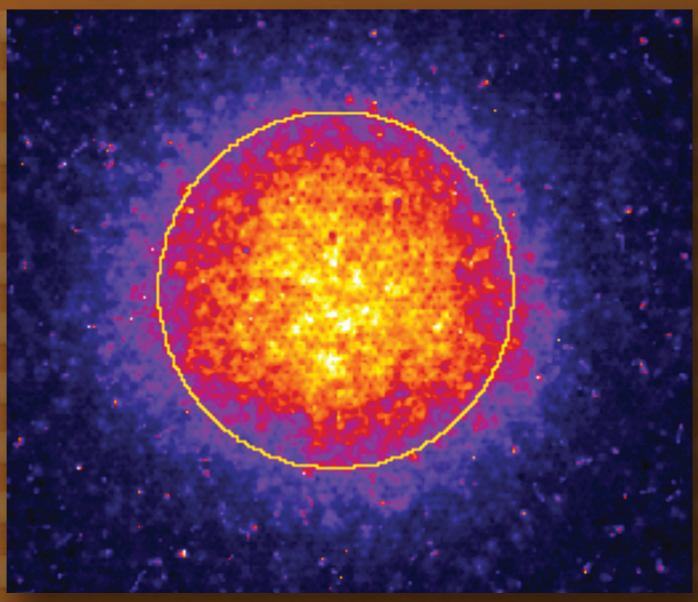

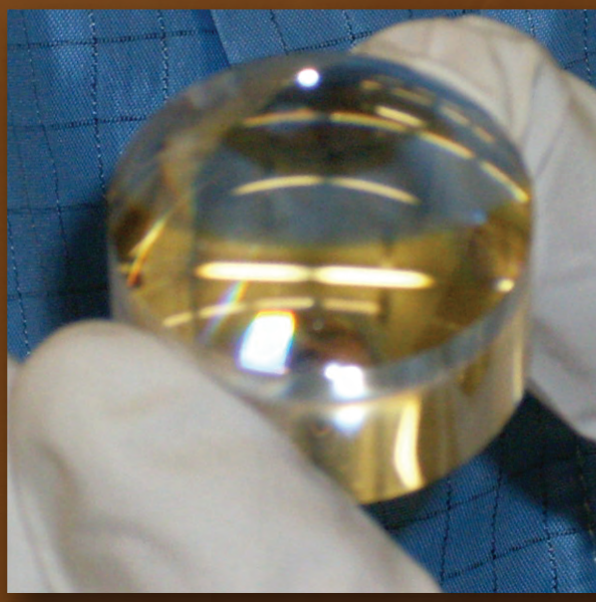

April 2010

Lawrence Livermore National Laboratory

LLNL-TR-438632

Acknowledgments

Scientific Editors
Camille Minichino
Don McNichols

Graphic Designers
Jeffrey B. Bonivert
Lucy C. Dobson
Kathy J. McCullough
Debbie A. Ortega

FY09

Engineering Research & Technology Report

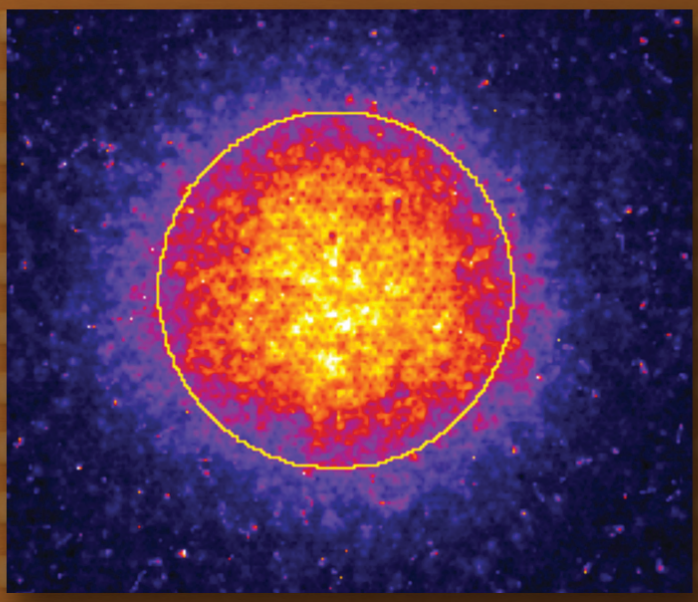

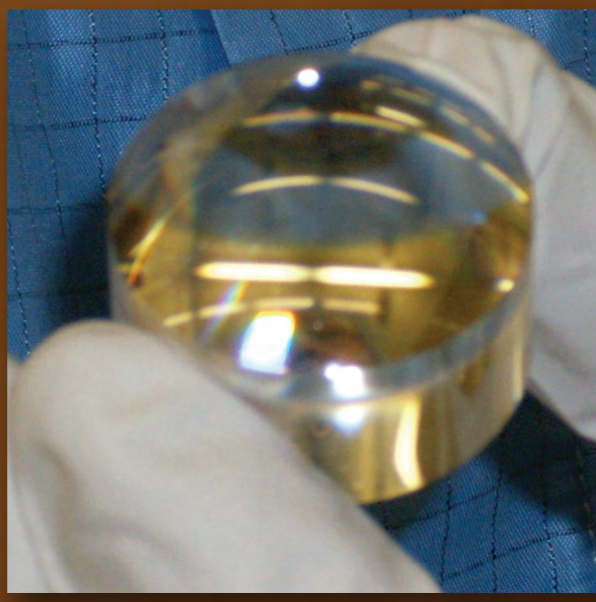

April 2010

Lawrence Livermore National Laboratory

LLNL-TR-438632

A Message From

Monya A. Lane
Associate Director for Engineering

This report summarizes key research, development, and technology accomplishments in Lawrence Livermore National Laboratory's Engineering Directorate for FY2009. These efforts exemplify Engineering's more than 50-year history of developing and applying the technology innovations needed for the Laboratory's national security missions. A partner in every major program and project at the Laboratory throughout its existence, Engineering executes this role with a highly-skilled workforce and capabilities developed through both internal and external sources. These accomplishments embody Engineering's mission: "Enable program success today and ensure the Laboratory's vitality tomorrow."

New in this year's report is a section featuring several compelling descriptions of significant engineering innovation. These innovations range from a revolutionary retinal prosthesis to new illicit material detection technologies to an ultra-precise robotic laser target assembly machine. All are examples of the forward-looking application of creative, groundbreaking engineering to pressing national problems and challenging customer requirements, resulting in new engineering capabilities.

Engineering's mission is carried out through both fundamental research and technology development. Research is the vehicle for creating competencies that are cutting-edge, or require discovery-class groundwork to be fully understood. Our technology efforts enable research breakthroughs, and also benefit from such breakthroughs, leading to broader application of technologies to a variety of Laboratory needs. The term commonly used for technology-based projects is "reduction to practice." As we pursue this two-pronged approach, an enormous range of technological capabilities results.

The balance of the report comprises short articles highlighting our work in research and technology, organized into thematic technical areas: Engineering Modeling and Simulation; Micro/Nano-Devices and Structures; Measurement Technologies; Engineering Systems for Knowledge and Inference; and Energy Manipulation. Our investments in these areas serve not only known programmatic requirements of today and tomorrow, but also anticipate the breakthrough engineering innovations that will be needed in the future.

Engineering Modeling and Simulation efforts focus on the research, development, and deployment of computational technologies that provide the foundational capabilities to address most facets of Engineering's mission. Current activities range from fundamental advances to enable accurate modeling of full-scale DOE and DoD systems performing at their limits, to advances for treating photonic and microfluidic systems.

FY2009 research projects encompassed material studies and models for low symmetry materials and materials under extreme pressures; and multiphysics coupling of electromagnetics with structural mechanics to simulate systems such as electromagnetic railguns. Technology projects included enhancements, verification, and validation of engineering simulation tools and capabilities; and progress in visualization and data management tools.

Micro/Nano-Devices and Structures encompass technology efforts that fuel the commercial growth of microelectronics and sensors, while simultaneously customizing these technologies for unique, noncommercial applications that are mission-specific to the Laboratory and DOE. The Laboratory's R&D talent and unique fabrication facilities have enabled highly innovative and custom solutions to technology needs in Stockpile Monitoring and Stewardship, Homeland Security, and Intelligence.

FY2009 research projects included systems for defense against biothreats and for the manipulation of biomolecules

and viruses; research to measure and understand the effects of osteoarthritis at the cellular level; studies of transport behavior and crystal-driven neutron sources; and the exploration of advanced detectors for identifying nuclear material. Technology projects included applications of lasers and optical sensors and new capabilities for micro- and nano-fabrication.

Measurement Technologies comprise activities in nondestructive characterization, metrology, sensor systems, and ultrafast technologies for advanced diagnostics. The advances in this area are essential for the future experimental needs in Inertial Confinement Fusion, High-Energy-Density Physics, Weapons, and Department of Homeland Security programs.

FY2009 research featured advanced algorithms for illicit radionuclide detection; x-ray array sources for nondestructive evaluation; and standing wave probes for micrometer-scale metrology. Technology projects included new error budgeting tools for nondestructive evaluation systems and component implementation for prompt diagnostics of key single-shot experiments.

Engineering Systems for Knowledge and Inference, an emerging focus area for Engineering as well as for the country at large, encompasses a wide variety of technologies. The goal is to generate new understanding or knowledge of situations, thereby allowing anticipation or prediction of possible outcomes. With this knowledge, a more comprehensive solution may be possible for problems as complex as the prediction of disease outbreaks or advance warning of terrorist threats.

FY2009 research efforts were centered on the extraction of information from unstructured text and advancing classification methods for a variety of applications. Technology efforts included adversarial modeling and prototyping a system to aggregate entity extraction algorithms.

Energy Manipulation, a long-time focus that is receiving increased emphasis due to newly emerging applications, encompasses the fundamental understanding and technology deployment for many modern pulsed-power applications. This area has broad applications for magnetic flux compression generators, components for modern accelerators, and high-performance apparatus for high-energy-density physics experiments.

FY2009 research focused on an ultra-high velocity railgun for material equation-of-state research and computational tools to aid in designing high-voltage vacuum insulators for pulsed power machines.

Contents

Introduction

Engineering Innovations

Engineering Modeling and Simulation

Micro/Nano-Devices and Structures

Measurement Technologies

Engineering Systems for Knowledge and Inference

Energy Manipulation

Next-Generation Compact High-Intensity Neutron Sources for Remote Detection

Vincent Tang
(925) 422-0126
tang23@llnl.gov

Advanced LLNL compact accelerator technology could provide the warfighter with unprecedented remote sensing capability.

One of the most challenging problems in national security is development of the capability to identify hidden threats, such as improvised explosive devices (IEDs) or shielded special nuclear materials (SNM), in the field at large standoff distances. The applications for such a capability range from counter-terrorism to treaty verification. At the conventional level, easy-to-produce, hard-to-detect, and destructive IEDs are likely to remain a key threat to U.S. forces for the foreseeable future.

Actively interrogating possible threats using neutron bombardment is a potential solution that could provide significant standoff or remote identification capability in the field, thus helping to neutralize these dangers. Figure 1 illustrates the concept: penetrating neutrons from a source bombard the unknown threat and induce nuclear reactions that emit characteristic gamma rays or neutrons. This induced radiation can be detected and used to identify the unknown material. For example, for IED detection, the quantity

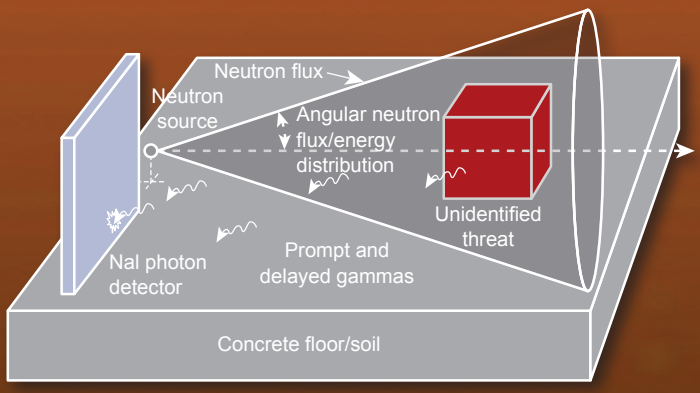

Figure 1. **(Left) Neutron pulses penetrate shielding and produce gammas through (n, n') or (n, γ) reactions, or neutrons from induced fission in SNM. This produced radiation can be used to identify materials in the threat. (Right) Possible concept-of-operation involving standoff detection of IEDs.**

Figure 2. (Left) A conventional ~10-m-scale 7-MV DC accelerator. (Right) The Compact Directional Neutron Source seeks to achieve similar voltages at the ~ scale to enable portable operation. A test accelerator column utilizing LLNL advanced high-gradient insulator technology designed for MV potential is being assembled.

of different MeV-level characteristic gammas emitted via inelastic neutron scattering reactions off carbon, nitrogen, and oxygen nuclei in the threat can be used to determine the unknown material's ratios of these elements. These ratios are known for a wide variety of organics and are good identifying markers for IEDs since explosives typically contain significant amounts of nitrogen. From a system point of view, the difficulty with achieving significant standoff distances stems from the size of conventional neutron generators and detectors, which are required to overcome signal-to-noise ratios that typically scale inversely with distance to the fourth power. The ideal neutron source would emit forward-directed and mono-energetic neutrons in order to maximize the signal-to-noise ratio and yet be compact enough for field operation. Because of physics considerations, directional sources typically require large accelerators operating at multi-MV potentials.

At LLNL, we are developing both isotropic and directional next-generation neutron sources centered on two new remote detection concepts of operation (CONOPs). For the directional source, we seek to shrink MV-level DC accelerators for making directional neutrons by an order of magnitude in order to achieve field portability. For the isotropic source, we aim to develop a self-contained, lightweight, palm-scale device operating at a ~100-kV potential. Such a device could easily be delivered to the unknown threat, thus maintaining user standoff. Since for this situation the source would be exceptionally close to the threat, an isotropic rather than directional source could be used. In both concepts, the sources would produce neutrons with energies in the MeV range and enable operation scenarios not possible before because of size constraints.

The Compact Directional Neutron Source (funded by the Defense Advanced Research Projects Agency) aims to take advantage of the D-D fusion reaction at greater than 4 MeV D ion beam energies to achieve forward-directed neutron output. The project is developing high DC-gradient accelerator technology to shrink conventional sources to achieve field portability. We are advancing new, compact piezoelectric power supplies; insulator technologies; and new, pulsed high-current ion sources in an integrated manner to achieve these objectives. Figure 2 provides a dramatic size comparison of existing technology against an experimental accelerator column using high-gradient insulator technology; the goal is to achieve DC

gradients greater than ~4 MV/m, which would enable field operation. We have so far achieved ~2 MV/m and multi-MeV neutron output with a greater than 3:1 forward flux directionality and have identified a technical path to the required 4 MV/m DC gradient.

For the isotropic approach, the LLNL Crystal Driven Neutron Source project exploits ~cm-scale pyroelectric crystals for producing ~100-kV-level voltages, with gradients in excess of 10 MV/m, for use in a novel, self-contained, palm-size D-T fusion-based isotropic 14.1-MeV neutron source. Figure 3 illustrates these pyrofusion sources schematically and also shows the LLNL pulseable pyrofusion "neutron flare" concept. By studying these novel high-voltage sources and mating them to advanced microelectromechanical systems (MEMS)-scaled ion sources, we have demonstrated pyrofusion operation with pulsed neutron output. Figure 4 shows our pyrofusion experiment using a micro-gap flashover ion source, and also depicts our ongoing development of nanoscale field-emitter ion sources. Our pyrofusion source holds records in neutron yields and is the first to show pulsed output, with peak rates greater than 10^{10} D-D neutrons per second. As a next step, we seek to further develop these sources to achieve average D-T neutron rates greater than 10^{7} per second while maintaining pulsing capability. At this level, significant opportunities exist for practical applications.

As we continue to develop our neutron source technologies, we will integrate them into system experiments designed to test our proposed CONOPs for standoff detection. Ultimately, we expect our leading high DC-gradient accelerator research to enable new possibilities for remote detection, thus providing critically needed solutions to the warfighter as well as answering key national security challenges.

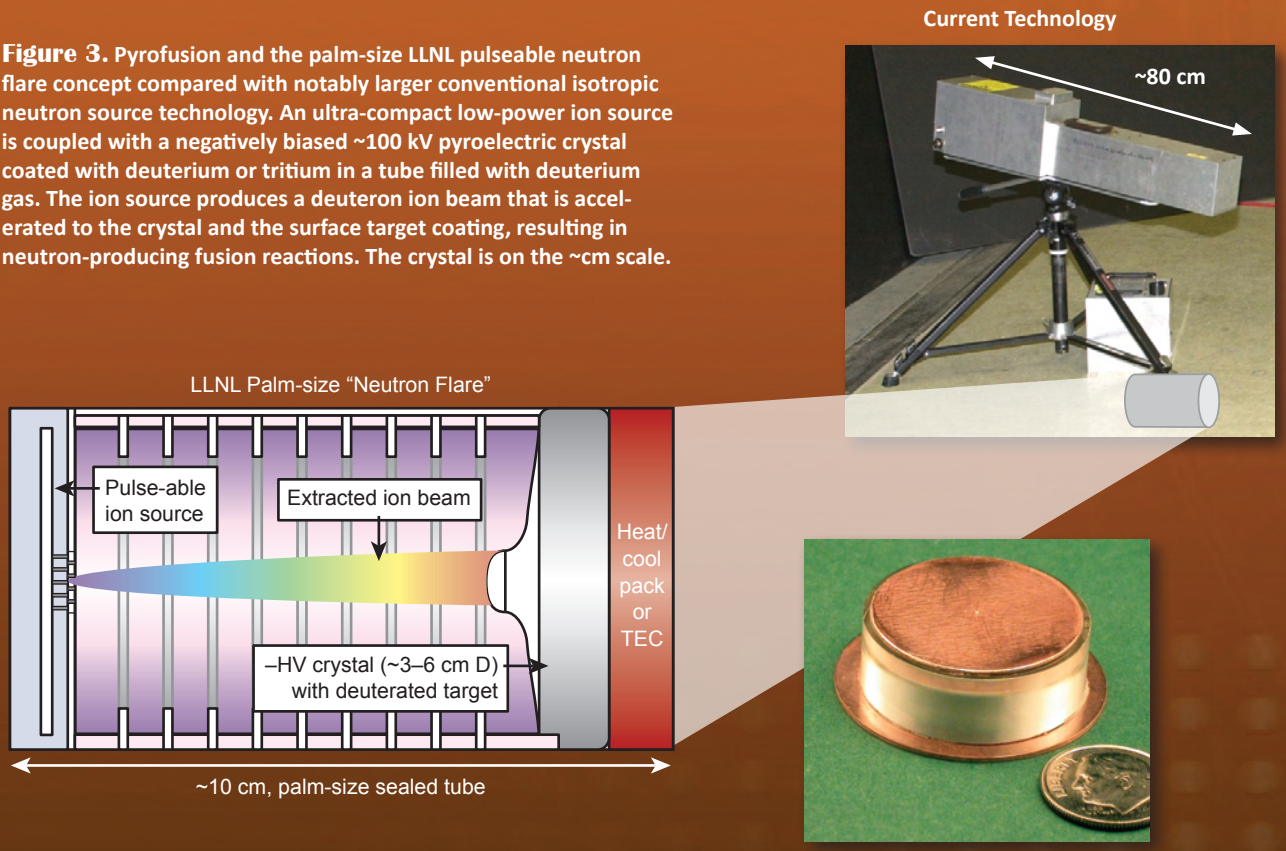

Figure 3. **Pyrofusion and the palm-size LLNL pulseable neutron flare concept compared with notably larger conventional isotropic neutron source technology. An ultra-compact low-power ion source is coupled with a negatively biased ~100 kV pyroelectric crystal coated with deuterium or tritium in a tube filled with deuterium gas. The ion source produces a deuteron ion beam that is accelerated to the crystal and the surface target coating, resulting in neutron-producing fusion reactions. The crystal is on the ~cm scale.**

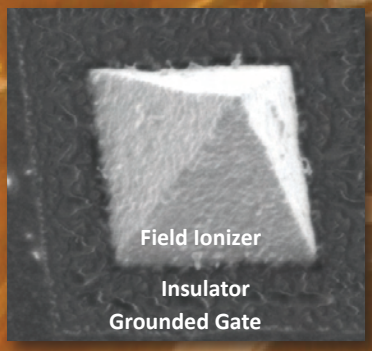

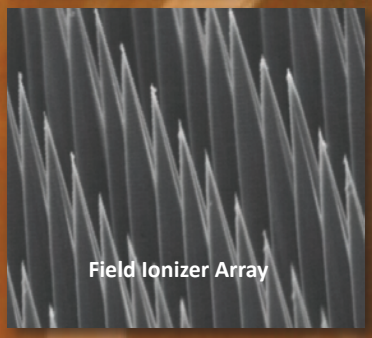

Figure 4. (Right) The LLNL pyrofusion experiment. The experiment produced the first pulsed pyrofusion neutrons with peak rates greater than 10^{10} D-D n/s and ~100-ns pulse widths. (Above) MEMs field ionizer arrays under development for efficient nanoscale ion sources for coupling to our pyroelectric accelerator.

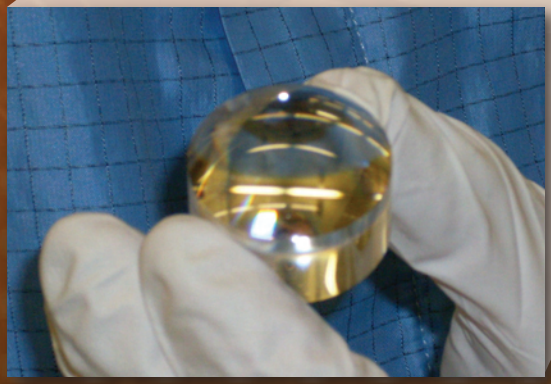

Artificial Retina: a Biocompatible Retinal Prosthesis

Satinderpall S. Pannu
(925) 422-5095
pannu1@llnl.gov

A retinal prosthesis co-developed by LLNL can provide at least partial sight to blind persons—even those who have been sightless for decades.

Millions of people worldwide suffer from ocular diseases that degrade the retina, the light-processing component of the eye, causing debilitating blindness. This sad fact is made more sobering when we consider that as our population continues to age, the number of Americans blinded by conditions such as age-related macular degeneration (AMD) and retinitis pigmentosa (RP) will increase. Fortunately, advanced technology is offering real hope to many who are or will be afflicted with blindness. A team of Lawrence Livermore National Laboratory (LLNL), four other national laboratories, four universities, and Second Sight® Medical Products, Inc., has developed a long-term retinal prosthesis that can function for years inside the harsh biological environment of the eye, restoring partial sight to those who may have been blind for decades.

In a human eye, light enters through the pupil, passes through the retina, and stimulates a layer of photoreceptor cells. The healthy human retina contains approximately 100 million photoreceptors. These and other specialized cells convert the optical signals into electrical signals that are processed and then transmitted to the brain, which interprets them as a visual image. Diseases such as AMD and RP destroy many of the photoreceptors, causing blindness. To restore sight, the Artificial Retina system converts images from a digital camera into controlled electrical impulses that can stimulate the retina's remaining specialized cells, thus taking the place of the destroyed photoreceptors (Figure 1).

The Artificial Retina system consists of a tiny video camera and transmitter mounted in sunglasses, a visual processing unit (VPU) and a battery pack worn on the belt that powers the entire device (Figure 2), and a retinal implant that stimulates the retinal tissue (Figure 3). LLNL contributes three major components for the Artificial Retina implant: a thin-film electrode array

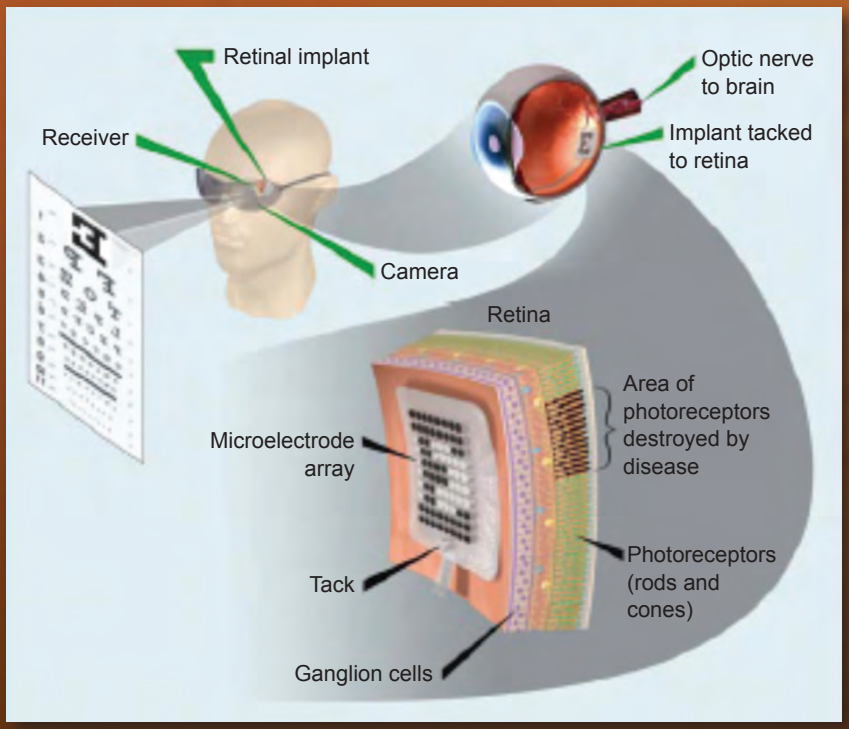

Figure 1. A schematic overview of the Artificial Retina system.

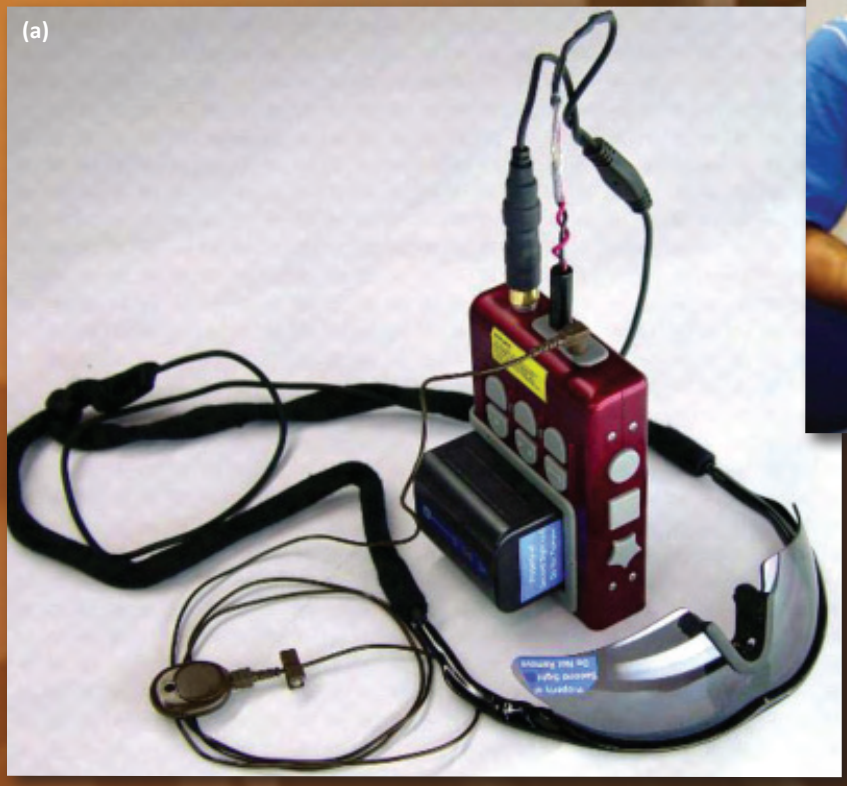

Figure 2. (a) The visual processor unit and the glasses with the embedded video camera. (b) A person wearing the visual processing unit and the glasses.

Figure 3. An overview of the 200+ electrode Artificial Retina implant. The thin-film electrode array is at the left end of the device, and the biocompatible electronics package is at the right.

that contains the neural electrodes; a biocompatible electronics package that contains the electronics for stimulating the retina; and an ocular surgical tool that will enable the insertion, attachment, and reinsertion of the thin-film electrode array. LLNL is also responsible for the system integration and assembly of these components to fabricate the complete implantable Artificial Retina system.

To develop neural electrode arrays with sufficient pixels to generate useful vision, a scalable approach had to be used. LLNL made the development process more economical by leveraging batch fabrication technologies from the semiconductor industry. In particular, photolithographic technology, thin-film metalization, reactive ion etching, and electroplating were required to fabricate these neural electrode arrays since their critical dimensions are on the order of micrometers. In addition, these thin-film electrode arrays were required to conform to the complex curvature of the retinal tissue. This requirement necessitated that the electrode arrays be fabricated on flexible polymers. Since these polymers are not typically used in the semiconductor industry, new technology and processes were developed using existing semiconductor equipment. These technologies enable the production of low-cost, batch-fabricated, high-density thin-film electrode arrays (Figure 4).

The Artificial Retina's biocompatible package contains the microelectronics required to stimulate the neural tissues as well as demodulate the radio frequency power and telemetry signals sent from the external camera and visual processing unit. It was particularly challenging to develop a biocompatible package that (a) was an order of magnitude smaller in volume than existing implantable medical packages and (b) increased the number of electrical feed-throughs required for communication to the thin-film microelectrode array by several orders of magnitude. Another challenge was that the compact size of the electronics package made it difficult to mechanically and electrically interconnect the microelectronics inside. The biocompatible electronics package also must withstand the harsh in-vivo environment within the human body for more than 10 years. To achieve this time span, the package had to be hermetic, *i.e.*, prevent all transfer of moisture or gases between the volume inside the package and the human body. In conjunction with Second Sight® Medical Products, Inc., LLNL has developed the fabrication

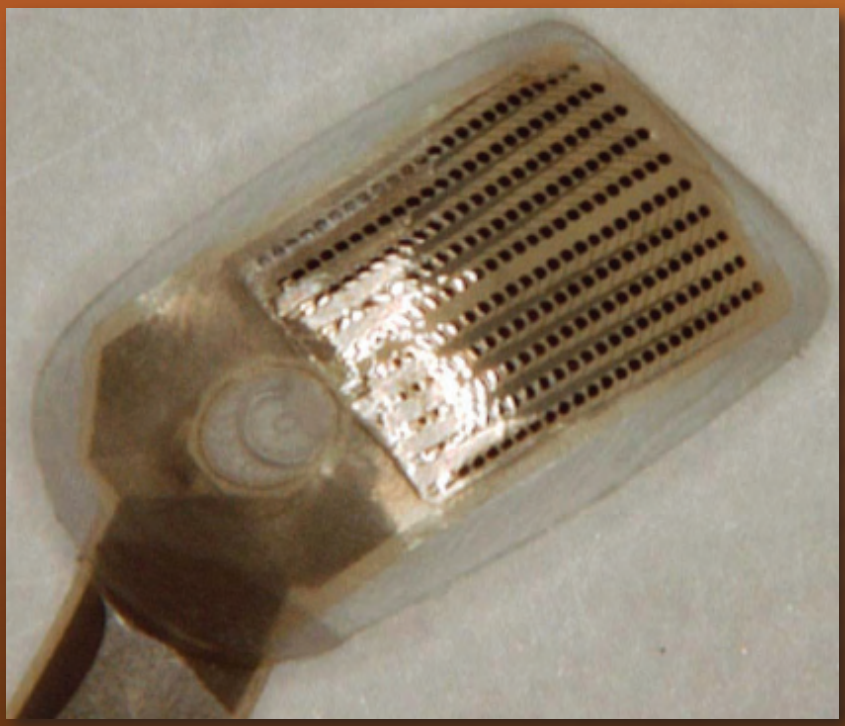

Figure 4. Close-up of the 200+ electrode array, which is attached to the retinal wall. This version should enable patients to recognize faces. Additional research and development will produce Artificial Retinas with 1000+ electrodes, which will provide better facial recognition and could enable reading.

Figure 5. Overview of the new ocular surgical tool required for retinal prosthesis removal and replacement. This ocular surgical tool is designed to fit onto a standard surgical handle.

and assembly technology needed to satisfy these requirements.

LLNL also designed a technology to remove and replace the existing thin-film electrode arrays. This technology makes it easier for patients to upgrade to newer versions of the Artificial Retina as they become available. For example, a 60-electrode Artificial Retina can be removed and replaced with a 200+ electrode version. We developed an ocular surgical instrument (Figure 5) that can be used to insert and remove the thin-film electrode array. This ocular surgical tool is used to place the thin-film electrode array onto a traditional retinal tack, or to remove it from the retinal tack.

System integration for the Artificial Retina involved developing high-density electrical interconnects between the thin-film electrode array and the biocompatible electronics package. These high-density interconnects must be insulated with a non-conductive film to prevent moisture, ionic, and biological contamination from causing device failure. Again, the density of electrical interconnects was at least an order of magnitude greater than existing technology. Special packaging technologies were developed to accomplish the electrical and mechanical interconnect between the electronics package and the thin-film electrode array.

The Artificial Retina is the only retinal stimulator currently undergoing large-scale, long-term (chronic) clinical trials. It is also the only retinal stimulator with a fully portable external system and an implant that can withstand daily use for many years. Patients in clinical trial use the Artificial Retina systems outside clinical settings at home and in public venues. In contrast, retinal stimulators developed by other groups have been used only for short-term research that restricted subjects to a clinical setting. In addition, other retinal stimulators have not demonstrated long lifetimes. The Artificial Retina is designed to last in excess of 10 years with daily use.

By increasing the number of channels by 10 times and decreasing its size by 10 times, the latest version of the Artificial Retina has 100 times greater channel density when compared to state-of-the-art commercialized neural stimulators such as cochlear implants. This achievement in implant design is a quantum leap in the implantable medical device industry and will enable a new generation of biological interface systems to be developed. Recognizing its significance, in 2009 R&D Magazine awarded the Artificial Retina technology not only a prestigious R&D 100 award, but also the Editors' Award, the utmost achievement in developing new technology.

The research and development of the long-term interface represented by the Artificial Retina challenges the limits of engineering, physics, chemistry, and biology. The successful integration of these profoundly different elements (biological tissue versus electronic and mechanical systems) has the potential to usher in a new era of sensors and actuators, not only for biomedical applications but also for a wide range of hybrid surveillance systems, including environmental sensors, and for plant and bacteria studies.

Thermal Neutron Sensor Technology to Detect Illicit Nuclear Materials

Rebecca J. Nikolić
(925) 423-7389
nikolic1@llnl.gov

Micro- and nanotechnology advances are enabling a revolutionary new microscale, solid-state system for developing sensors to detect illicit special nuclear materials.

In the years since September 11, 2001, significant progress has been made to help ensure our country remains safe from any future attack. One scenario especially has haunted our national security planners: the detonation of an improvised radiological or nuclear device. As concerns about nuclear materials falling into the wrong hands have increased, so have efforts to develop new generations of sensors to detect these materials. One important research area seeks to improve the efficiency and adaptability of devices used to detect illicit special nuclear materials.

For many homeland security and nonproliferation efforts, semiconductor materials such as silicon can be used to custom-make 3-D microstructured sensors. Since nuclear materials release gamma and neutron energy, experts within Engineering's Center for Micro and Nano Technology (CMNT) are working to develop nano- and microsize sensing and detection devices for both types of radiation.

Neutron detectors are employed in a wide range of applications, including scanning air and ship cargoes, monitoring spent nuclear fuel, neutron imaging, monitoring ports of entry, and active interrogation of suspicious items. For certain applications, detectors must be inexpensive and robust, operate at ambient temperature, provide high detection efficiency, and be small enough for use in covert operations. Current detector technologies are limited in their ability to meet all of these requirements simultaneously. For example, many current gamma-ray detectors operate properly only at cryogenically cooled temperatures, a factor that significantly increases the overall system size. Devices used in the field for thermal neutron detection typically operate with tubes filled with Helium-3 (^{3}He) gas, a design with some inherent limitations. Such instruments are large, require high voltage to operate, and are sensitive to vibration. Additionally, ^{3}He is difficult to obtain and supplies of this important material are fast declining.

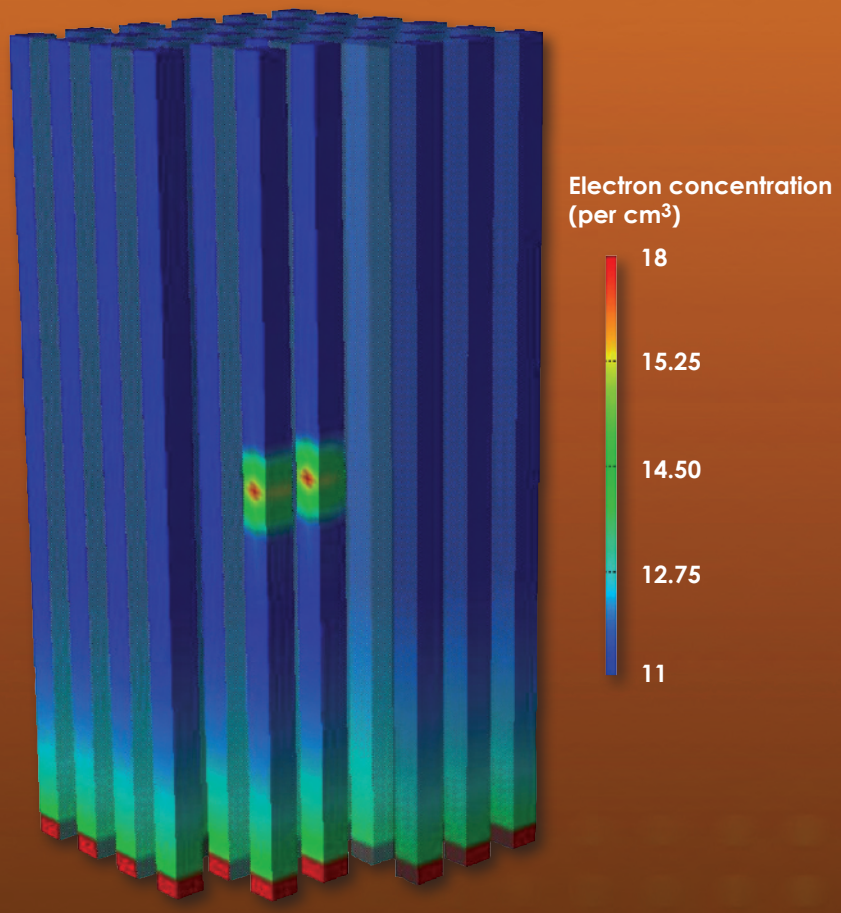

Figure 1. The simulated electron concentration in a 50-µm-tall pillar array 100 ps after the interaction of a neutron with the detector is shown (some areas have been removed for a better view of the interaction point).

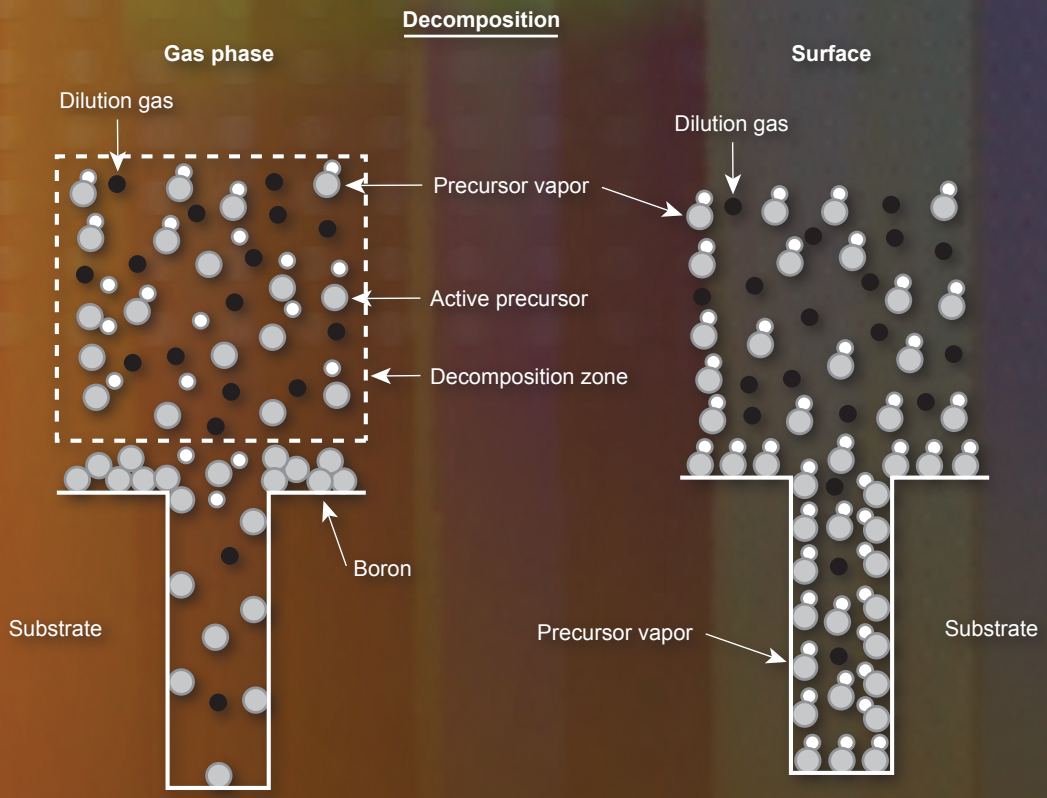

Figure 2. Schematic drawing showing gas phase versus surface decomposition. Surface decomposition is needed for conformal coating of boron within the pillar array.

Micro- and nanotechnology advances are enabling a revolutionary ^{3}He-tube replacement technology. A research team led by engineer Rebecca Nikolić has demonstrated that a microscale, solid-state system can be fabricated to produce high-efficiency thermal neutron detectors. The Livermore team's device, called the Pillar Detector, promises to achieve more than twice the efficiency of conventional thermal neutron detectors used in the field without the fieldability issues that challenge gaseous detectors.

Instead of gaseous ^{3}He, the Pillar Detector relies on a carefully constructed platform of 3-D etched silicon pillars that are interspersed with Boron-10 (^{10}B). We can adjust the pillar etch depth to provide a thicker boron layer for high neutron capture. We can also adjust the spacing between the pillars so the alpha particles don't have to travel far, which provides the device with high efficiency." The LLNL team is collaborating with the University of Nebraska at Lincoln, which uses chemical vapor deposition to fill the pillars with ^{10}B. Recently, the team demonstrated a thermal neutron efficiency of 20%, which is the largest efficiency reported to date for a semiconductor-based thermal neutron detector using ^{10}B as the converter material.

Designing the pillar-structured thermal neutron detector required understanding the complicated multistep reactions that take place between a neutron striking the Pillar Detector and the current pulse that provides the electrical signal. Three different simulation tools were needed to unravel the physics that take place. A particle transport simulation (Figure 1) shows the electron concentration in a 50-µm-tall pillar array 100 ps after the interaction of a neutron with the detector. By combining results from multiple models, an optimized pillar structure was carefully designed. With the design established, the 3-D structure could be fabricated.

Conformal filling of high-aspect-ratio silicon micropillar structures with ^{10}B film was developed using low-pressure chemical vapor deposition (LPCVD) with decaborane. For this work, it was necessary for the ^{10}B to decompose on the surface of the pillar array instead of in the gas phase. If decomposition occurs in the gas phase, the boron coating will reside at the top of the pillars and a poor fill factor will result, as shown schematically in Figure 2. A high volume of ^{10}B is needed to efficiently capture the thermal neutrons.

Just as there was a lack of available processes for boron deposition, there was also a void in boron etching processes. Previous work to remove boron with plasmas had been reported, where plasmas were used to clean thermonuclear reactor chambers in which boron was used as a protective coating. In a similar vein, we developed an Electron Cyclotron Resonance (ECR) plasma etch approach based on fluorine chemistries. Figure 3 shows the processing progression to fabricate the Pillar Detector.

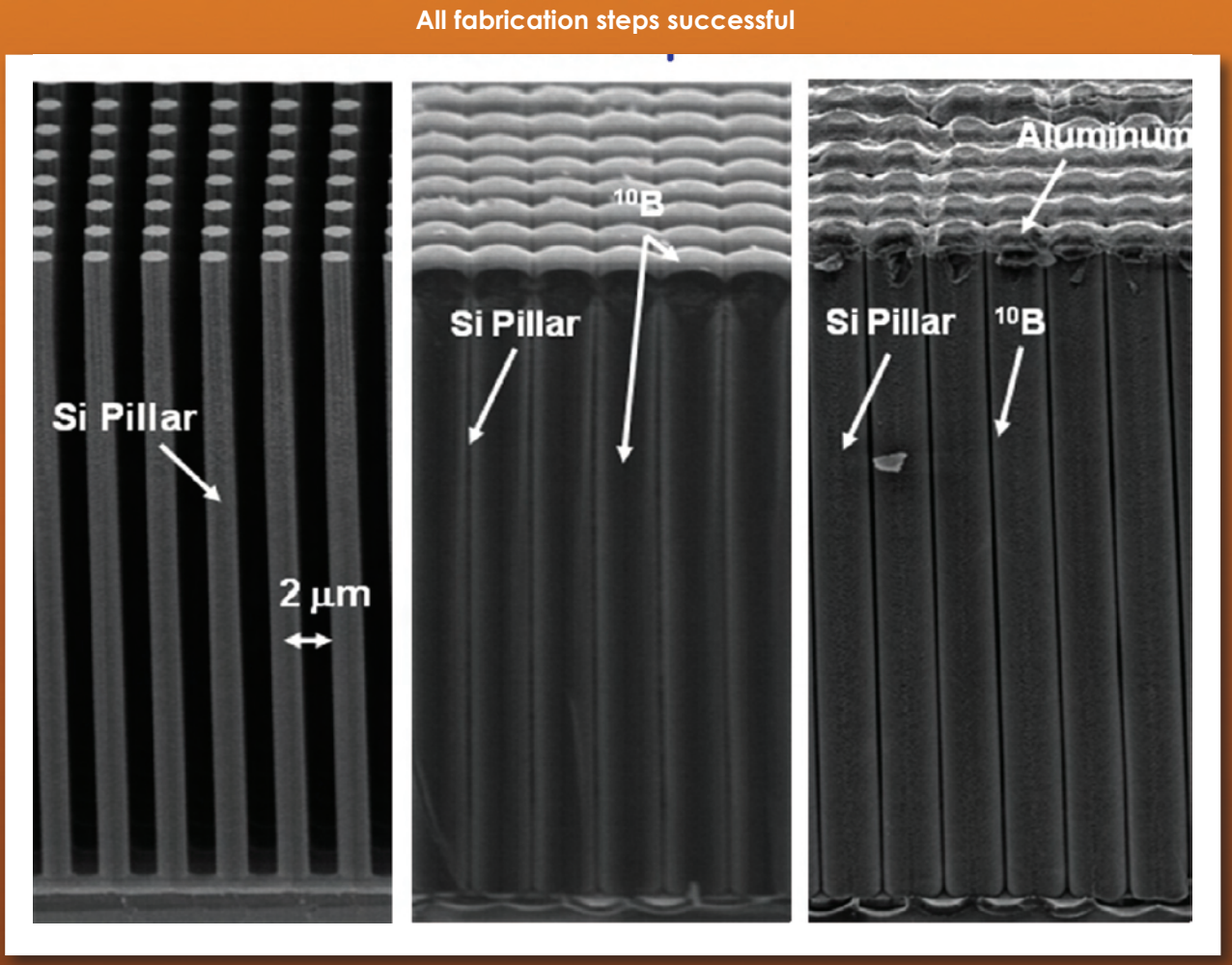

Figure 3. Progression of fabrication steps needed for the pillar processing.

Eventually, the LLNL pillar design is expected to provide over 50% efficiency and operate at low power (Figure 4). Because the silicon wafers can be cut to any size, a detector of any size can be produced, thus meeting the needs of many different end users. In almost every way, the three-dimensional silicon–boron wafer is superior to the ^{3}He tube. The wafer device requires less than three volts for operation, and newer designs may require even less. In addition, this highly effective detector will have less than 5 percent the physical volume of the standard ^{3}He detector for the same efficiency. The pillar-structured thermal neutron detector could prove to be the enabling technology for the next generation of radiation detection devices used as part of the effort to keep our homeland safe.

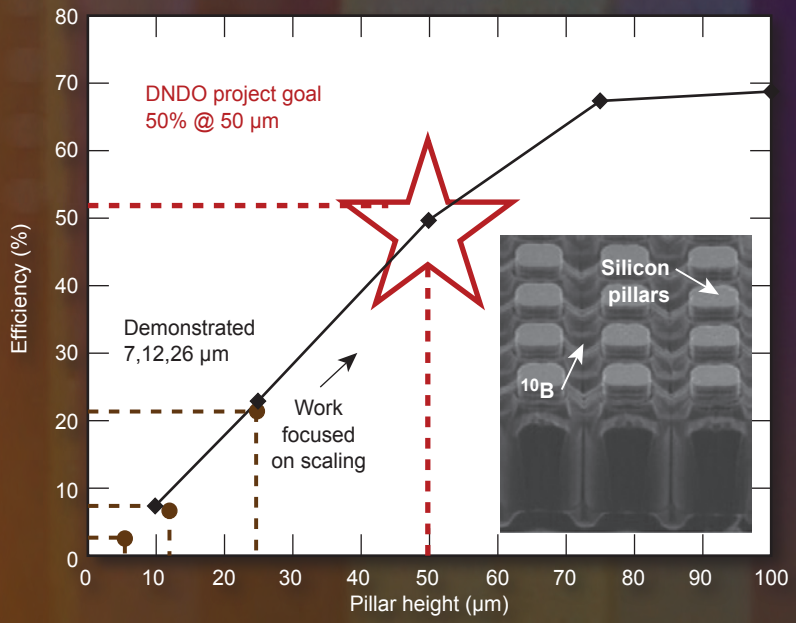

Figure 4. **The team is now funded by the Department of Homeland Security to scale the device to 50% thermal neutron detection efficiency.**

A Precision Robotic Assembly Machine for Building Nuclear Fusion Ignition Targets

Richard C. Montesanti
(925) 424-5605
montesanti1@llnl.gov

Delivering unprecedented accuracy, efficiency, and repeatability for micrometer-scale laser target assembly, this machine can be adapted to build other complex miniature systems.

The primary goal of the world's largest and most energetic laser, the National Ignition Facility (NIF), is to achieve a self-sustaining nuclear fusion burn with energy gain in a laboratory setting. One of the keys to attaining this goal is the production of targets that meet extraordinarily demanding specifications in materials fabrication, machining, and assembly. As shown in Figure 1, many of the target components are designed to slip-fit together with micrometer-scale clearances, and the dimensional accuracy of a fully

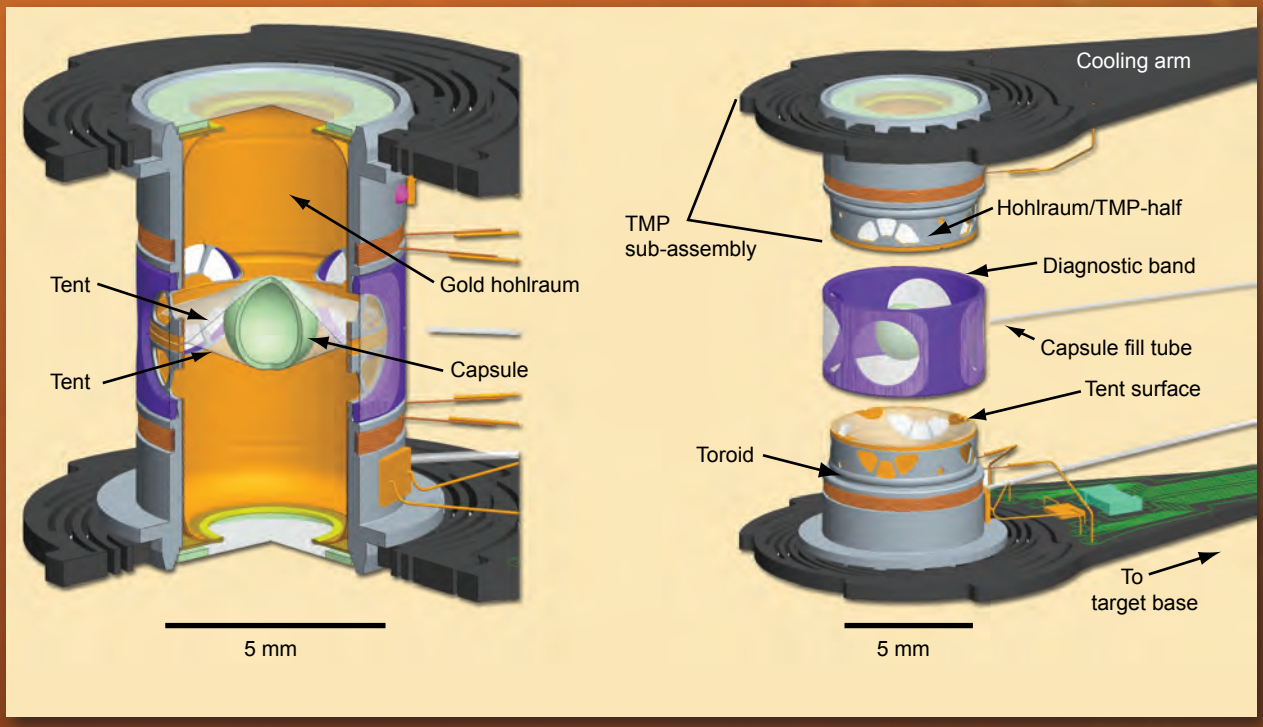

Figure 1. Model of a fusion ignition target showing the major components.

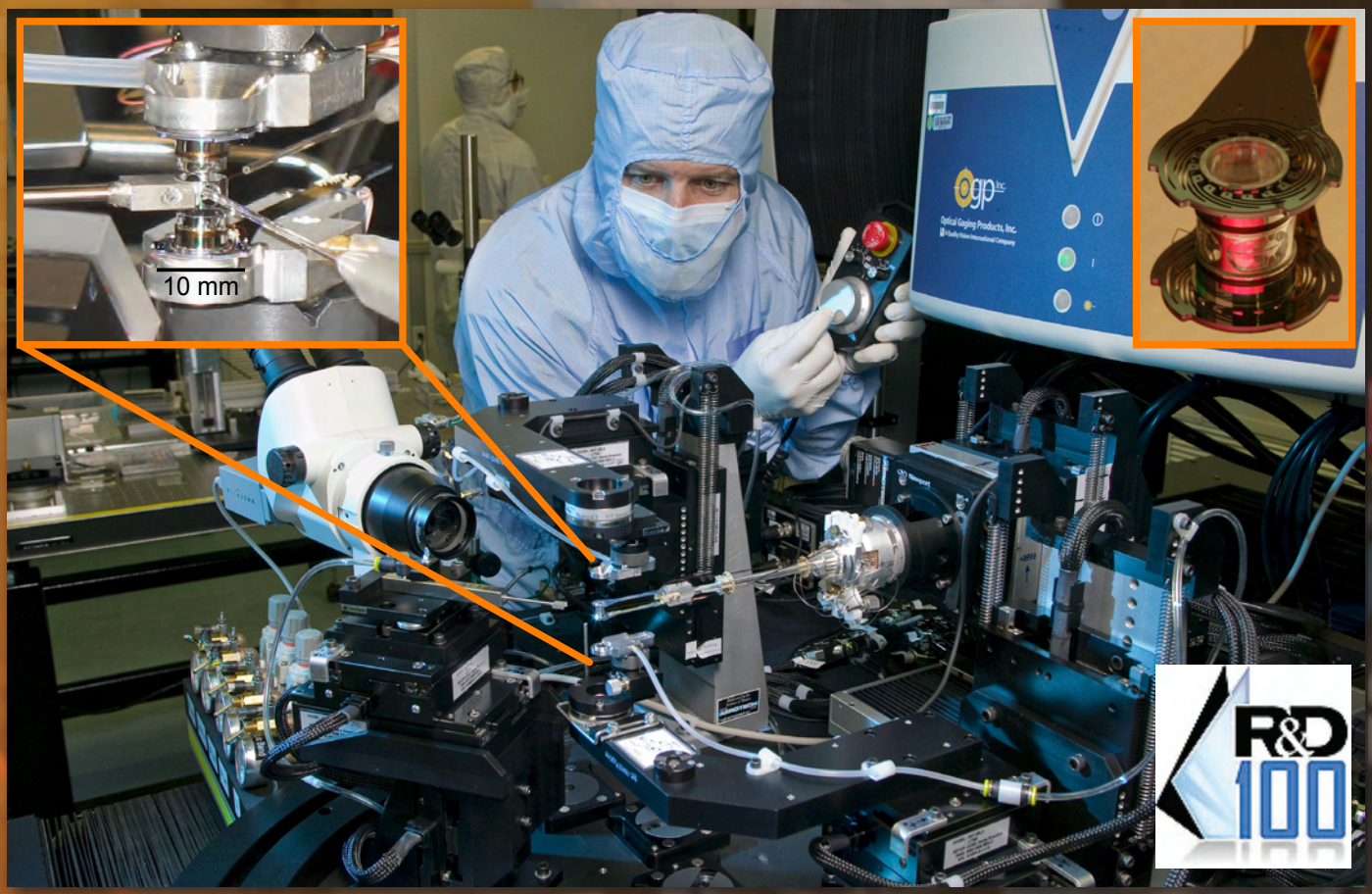

Figure 2. The Precision Robotic Assembly Machine releasing a laser fusion target that was just assembled. Target components being assembled (left inset). A completed target (right inset).

assembled target is in the range of 2–20 micrometers. Historically, building laser fusion targets depended on a significant amount of hand-crafting skill and technique involving microscopes and manually driven fixtures, a methodology that resulted in unacceptable variability in target quality. The Precision Robotic Assembly Machine (Figure 2) is the first fully engineered system for assembling NIF targets, and its use has removed the risk to fusion ignition experiments posed by targets of variable quality. The machine provides unprecedented accuracy and efficiency, and a ten-fold reduction in manpower needed to assemble laser fusion targets.

The Precision Robotic Assembly Machine operates in a class-1000 clean room, and consists of an

LLNL-developed manipulator system integrated with an optical coordinate-measuring machine (OCMM). Figure 3 shows a close-up view of the manipulator system, which can be reconfigured to accommodate different laser fusion target designs. Nineteen motorized and 10 manual degrees of freedom provide simultaneous manipulation of five objects in a 1-cubic-cm operating arena with 100-nm precision and micrometer accuracy. A unique attribute of the machine is its ability to stitch together multiple millimeter-scale operating arenas over distances spanning tens of centimeters with micrometer-level accuracy. Sensors embedded in the manipulator system provide 100-mg resolution force and gram-millimeter resolution torque feedback of the contact loads between components being assembled with micrometer-level or no clearance. The OCMM has a machine-vision system, laser-based distance-measuring probe, and touch-probe that provide micrometer-level accuracy measurements. Auxiliary mirrors provide the OCMM with multiple viewing directions of the target. The vision and measurement systems of the OCMM are used to guide the initial approach and alignment of the target components, and to measure the relative position and orientation of the components. The force and torque feedback is used to guide the final approach, alignment, and mating of the delicate target components.

The Precision Robotic Assembly Machine transforms the way laser-driven fusion ignition targets are built so that one person can assemble a high-quality target in one day, and repeat that quality every time. The vision was to create a system that would allow a target assembly technician to build a target in a manner similar to how a surgeon uses a surgical robot to perform a delicate operation: the operator provides top-level control of the machine, initiating and controlling the movement of the motorized precision instruments. Hand movements that are precise in the millimeter-scale realm are scaled to precision in the 100-nanometer realm, and innovative use of force feedback with 100-mg resolution allows the operator to "feel" the delicate components being assembled and adjust accordingly. The machine has enabled every operator to build fusion targets with an equally high level of finesse and repeatability. This accomplishment is more remarkable considering it was achieved, from early concepts to a working machine that assembled targets that met specification, in only 14 months.

Figure 3. Close-up view of the manipulator system, with a target being assembled.

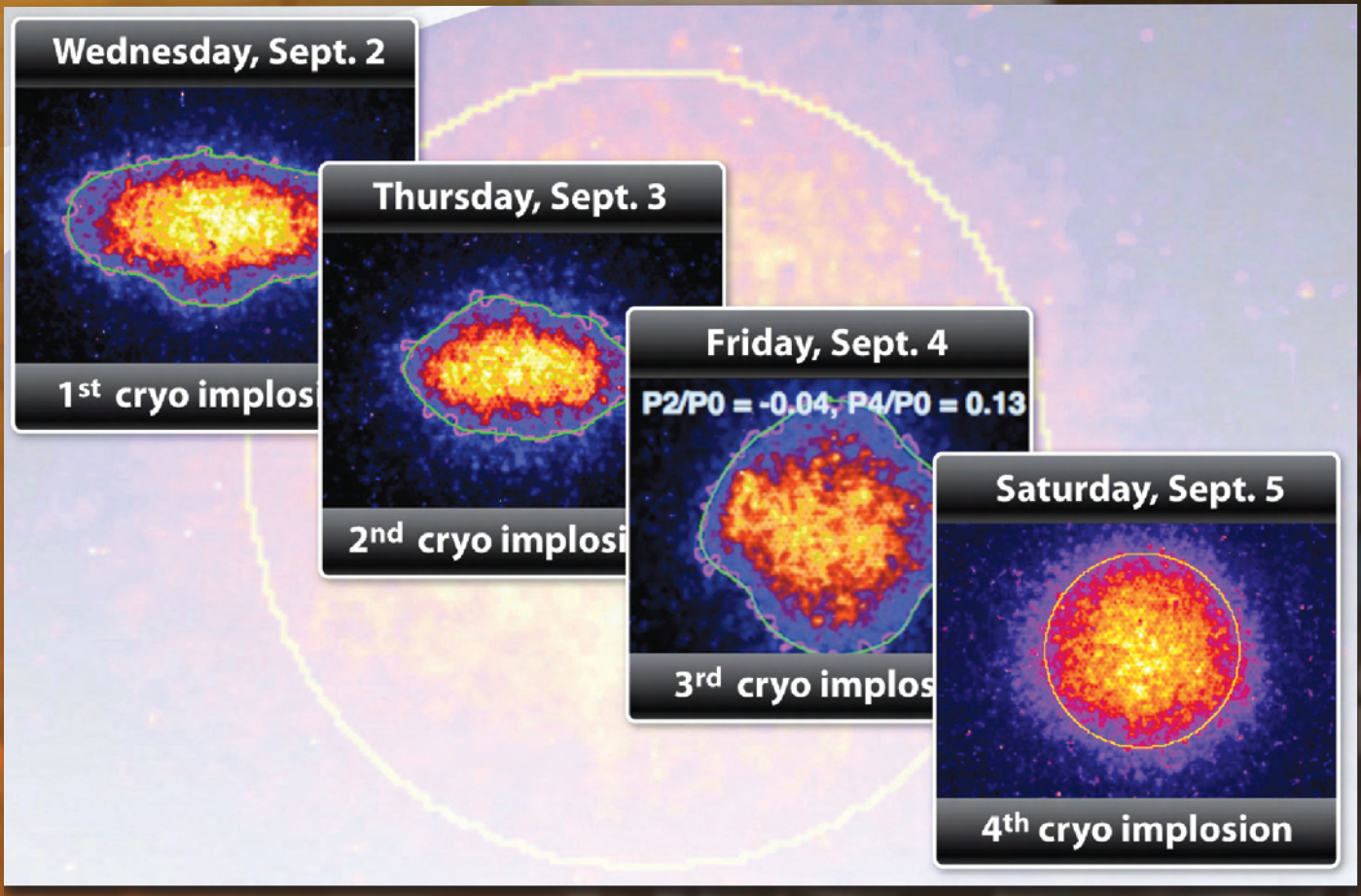

Figure 4. X-ray images of the imploding fuel capsule for four sequential cryogenic target shots at the NIF in September 2009.

The value of reliable, repeatable, and consistent production of high-quality, precision ignition targets for the National Ignition Campaign was demonstrated recently. Figure 4 shows the x-ray images of the imploding fuel capsule in four different targets built with the machine. The desired spherical shape of the fourth shot was achieved by using data from the previous three shots to incrementally adjust the laser beams. This use of the NIF to step-wise converge on a desired symmetrical capsule implosion was a momentous accomplishment for the National Ignition Campaign, and was made possible in large part because of the repeatable, high-accuracy targets built with the Precision Robotic Assembly Machine.

The Precision Robotic Assembly Machine provides a balance between the earlier method of manually assembling a target and a fully automated system. Certain aspects of the target assembly process, such as alignment of components and measurements of that alignment, are being automated. To the extent that each target is slightly different from the ones before it—just as each person undergoing the same surgical procedure is slightly different—the operator stays in the loop as the top-level controller. As targets for a sustained campaign converge on being identical to each other, the level of target assembly automation can be increased by adding a machine-based, top-level control system.

Laser-driven fusion targets for the NIF program are a first application for the Precision Robotic Assembly Machine, which can be adapted to build other complex miniature systems. The multiple technologies integrated into the machine bridge the gap between building miniature- and man-sized machines. The machine could provide a key enabling platform for significant advances in the discovery and manufacture of centimeter-scale systems that integrate millimeter- and micrometer-scale optical, electrical, mechanical, and biological subsystems.

Improved Aviation Security via Technology Advancements

Harry E. Martz, Jr.
(925) 423-4269
martz2@llnl.gov

Efforts to improve and advance airport baggage and passenger screening systems by applying advanced technology are paving the way for safer air travel.

In the years following the September 11, 2001 attacks, commercial passenger flights have continued to be high-priority targets for attempted terrorist strikes using explosives. From failed "shoe bomber" Richard Reid in December 2001, to the foiled plot to attack multiple flights using smuggled liquid explosives during summer 2006, to the attempted "underwear bomber" on Christmas Day 2009, terrorists have shown considerable ingenuity in trying to sneak explosive devices onto planes. Defending against such efforts is a high priority for the Transportation Security Administration (TSA) and the Department of Homeland Security (DHS). DHS has contracted LLNL to assist in the development and procurement processes for advanced technology for improved aviation security. President Obama has asked the national labs, including LLNL, to increase their efforts related to national security (Figure 1).

Prior to 9/11, screening devices at airports (e.g., metal detectors and baggage x-ray scanners) were employed primarily to detect knives and guns. After 9/11, additional devices were deployed to detect explosives in checked baggage. This additional equipment included specially designed computed tomography (CT) scanners for detecting bulk explosives as well as equipment for detecting explosive traces. In response to some of the previously noted attempted attacks, pilot programs have been undertaken to install equipment to detect threats in shoes, find liquid explosives in carry-on baggage, and find threats concealed under passengers' clothing.

Current explosives detection systems operate by scanning for certain material characteristics, such as the mass and atomic number of explosive components. However, some innocuous materials share the same characteristics found in threats, resulting in imprecise scanning results and many false alarms. These false alarms necessitate additional manual screening of baggage, passengers, and other divested objects, leading to greater labor expense, operator fatigue, additional space requirements to conduct added screening, and passenger inconvenience. The demonstrated ingenuity of terrorists emphasizes the need for detecting even more potential threats, which might cause even more false alarms.

There is a great need to improve the accuracy of presently deployed detection equipment, identify additional material characteristics that can be used to differentiate threats from non-threats, and discover additional methods for examining passengers and baggage that can lead to development of next-generation equipment. DHS asked LLNL to work

Figure 1. Portion of the Presidential Memorandum of December 29, 2009, directing the National Laboratories to assist in reviewing and improving aviation security.

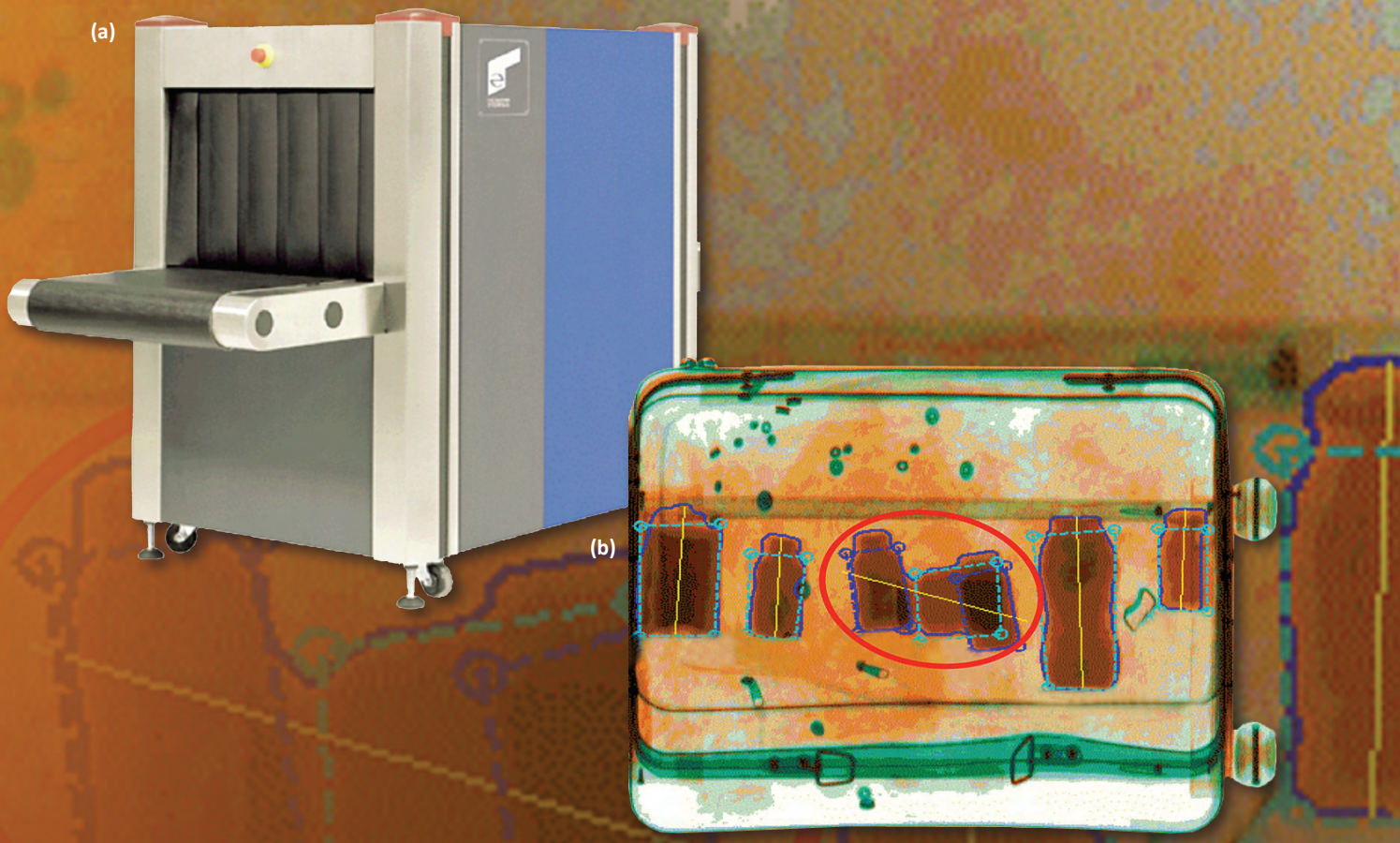

Figure 2. (a) An example of an x-ray carry-on luggage inspection system. (b) A sample x-ray scan image showing threats and non-threats in bottles in a suitcase. The dashed bounding boxes are keys provided by LLNL. The solid dark blue outlines are the segmentation boundaries from a third-party algorithm. The yellow line is the major axis of a detected item. Red ovals highlight overlapping objects.

on these goals and their component challenges based on our unique experience and understanding in the areas of algorithm development and materials characterization. This experience and understanding comes from LLNL's long history of researching, developing, and applying similar techniques in our weapons and stockpile stewardship work. In adapting this knowledge to airport security, DHS has requested that our work be applicable to checked baggage, carry-on baggage and divested objects at checkpoints, whole-body imaging (now known as advanced imaging technology), and standoff detection.

The results of our work are helping to inform third-party vendors, who manufacture detection systems, and the TSA, who will use the knowledge to make policy decisions.

In order to increase the accuracy of current commercial detection equipment, it must be made "smarter" and more sensitive. For x-ray scanning equipment, we are conducting fundamental research to characterize the x-ray properties of threats (i.e., explosives and their various component materials) and prevalent non-threat materials (i.e., bottled water, food items, toiletries, etc.) and store the results in a database (see Figure 2). This data is then being used to predict the impact on false alarm rates when newly identified threat materials need to be detected. The results are also used to find additional features that can aid in distinguishing threats from non-threats. Ultimately, in partnership with government agencies, vendors, and third parties, this information will be used to develop advanced algorithms such as automated target recognition (ATR) and reconstruction algorithms.

In one example of the application of this research, LLNL scanned explosives on two commercial x-ray projection scanners at Tyndall Air Force Base in Florida. The resulting images were archived in LLNL's database and then provided to several third parties along with a technical statement of work. The third parties developed ATRs, which were independently evaluated by LLNL. At least two of the third parties are now working with vendors to commercialize their ATRs so that they can be incorporated into a new generation of x-ray scanners.

The precision of the features used by an ATR is a function of the quality of the images generated by a scanner. The CT-based security scanners presently deployed rely mainly on image reconstruction algorithms that were developed for medical imaging applications; hence, these algorithms have not been optimized for use in an airport security setting. As shown in Figure 3, streak artifacts can reduce performance in CT images of scanned baggage. To increase accuracy, LLNL is investigating two

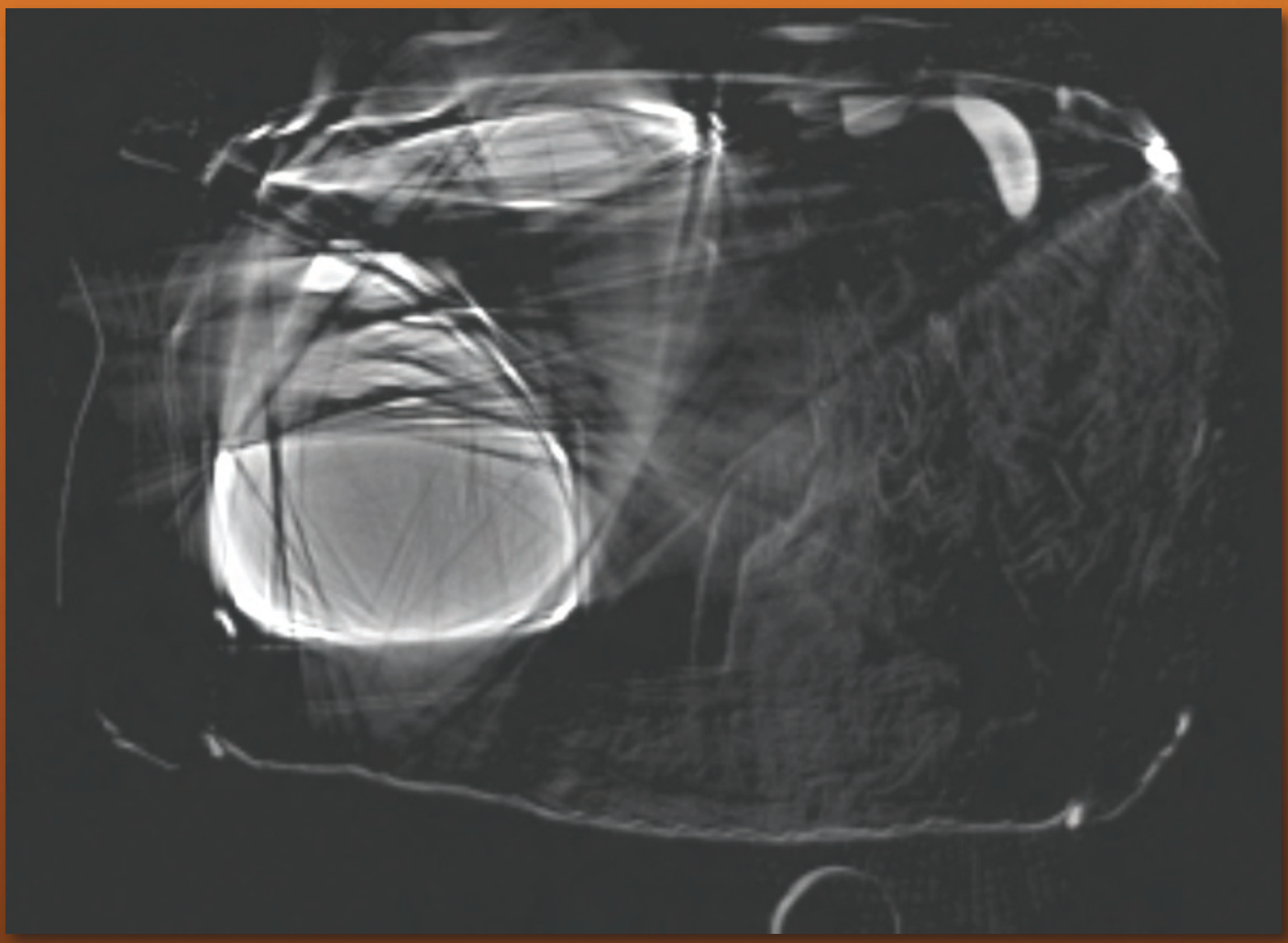

Figure 3. Streak artifacts can be a problem in CT images, as shown above.

iterative image reconstruction methods that can help reduce, if not eliminate, streaks. Our efforts have helped speed and improve both methods, and both can be used to reduce streak artifacts and improve the quality of images derived from scanner data (Figure 4).

As work in both government and commercial arenas continues to improve scanner technology, LLNL is helping to codify standards for these devices, providing technical guidance to a standards organization to develop a common format for data and images from security scanners. We are also pinpointing capability gaps in current equipment and actively reviewing literature and patents and engaging with colleagues at other national labs, academia, and industry to identify new technologies that could improve existing equipment or lead to new scanning methods. This work is enabling TSA, DHS, and airport security officials in their efforts to stay a step ahead of terrorists.

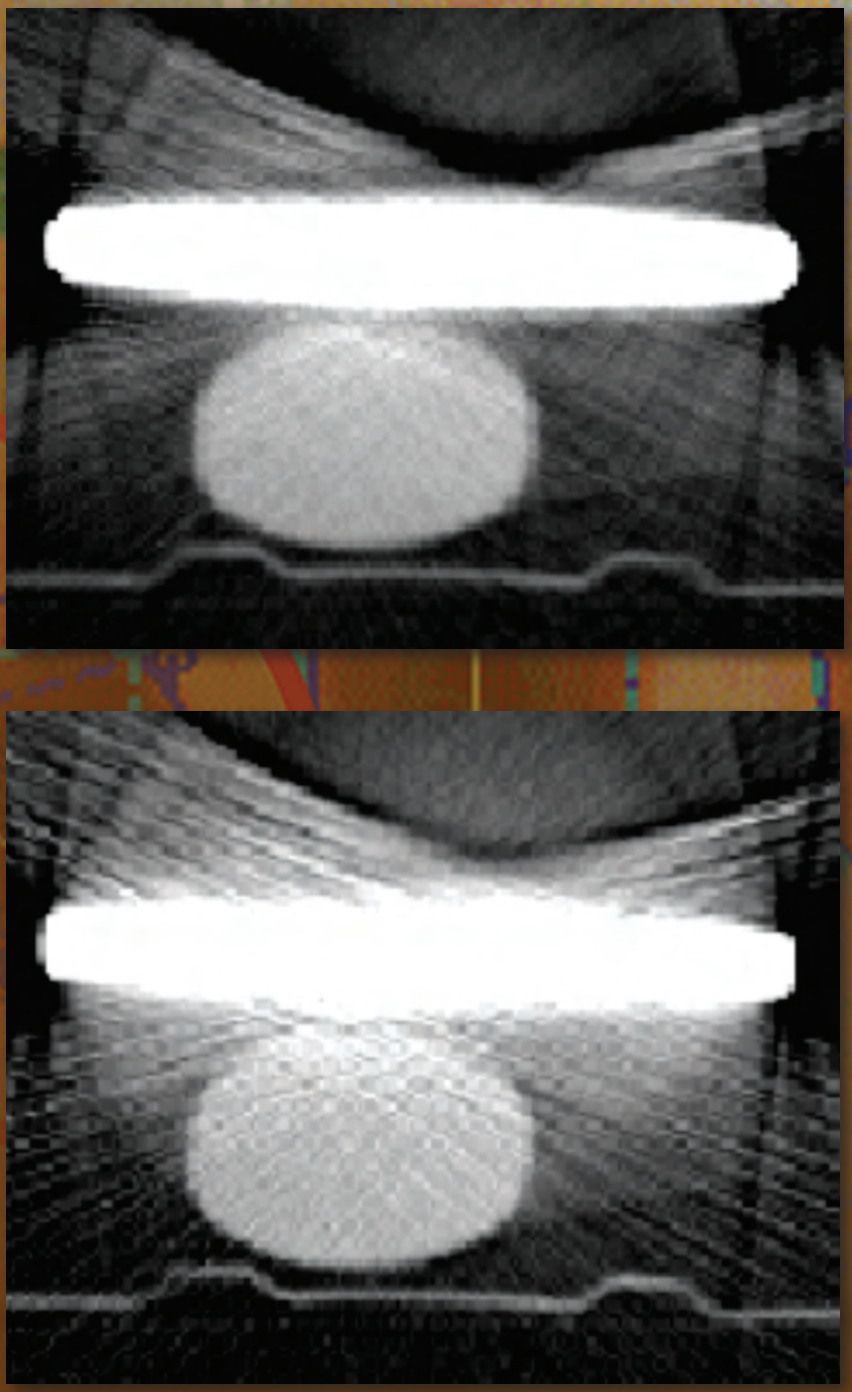

Figure 4. We are investigating iterative image reconstruction methods, such as an adjoint method (top) and traditional Filtered Back Projection (bottom). Both of these techniques reduce streak artifacts, improving the quality of scanner data and enabling more accurate results.

Engineering Modeling & Simulation

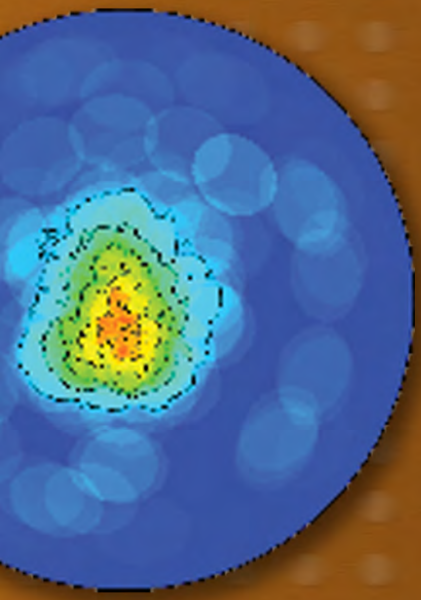

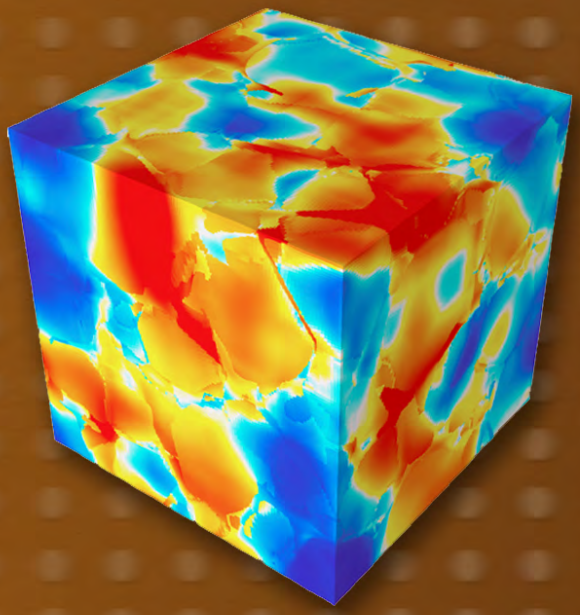

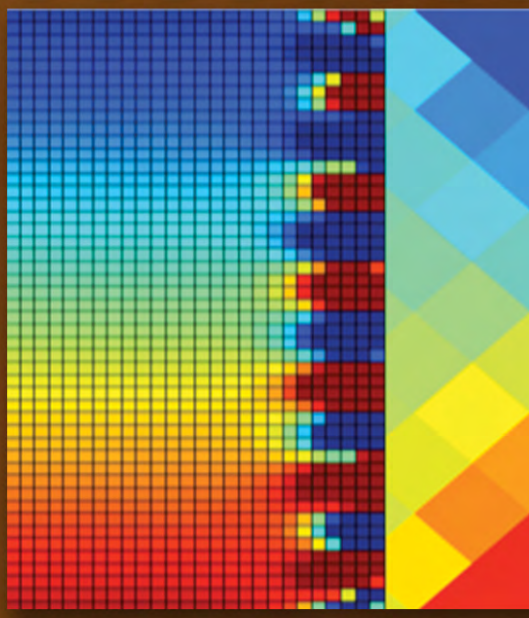

Deformation of Low Symmetry and Multiphase Materials

Nathan R. Barton
(925) 422-9426
barton22@llnl.gov

Materials composed of low symmetry crystals or of multiple solid phases exhibit heterogeneous deformation at the microstructural scale, often including deformation by mechanical twinning. Such heterogeneous deformation produces significant challenges in efforts to construct macroscale constitutive models, and necessitates careful attention in connecting to suitable experimental data. Heterogeneity at the microstructural scale also produces stress concentration that can lead to fracture or influence the onset and progress of phase transformations. We have developed an approach that explicitly incorporates effects of microstructure and deformation heterogeneity in a framework suited to analysis of engineering scale components.

Applications involving fully developed plastic flow are targeted. Basing polycrystal level models directly on experimentally measured microstructures, we build on recently developed technologies for effectively combining microscale plasticity simulations with macroscale models. This results in effective macroscale models for materials whose behavior is difficult to predict using conventional approaches. New capabilities capture the impact of microstructure, and thus material processing, on the performance of engineering scale components. For example, phenomena such as shear localization arise naturally.

Project Goals

Our overarching goal is to produce effective macroscale models through novel homogenization methods for a challenging class of materials. The immediate application space includes a wide set of engineering simulations, ranging from forming operations to dynamic loading scenarios. Figures 1 and 2 show example applications, with

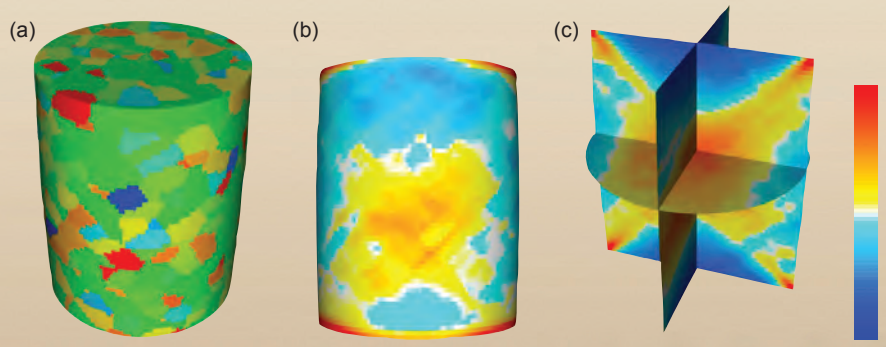

Figure 1. Results from a simulated Ti-6Al-4V compression test. (a) Long-range ordering of the microstructure associated with prior beta grain structure at elevated temperature. Strain localization patterns are shown in plots of the plastic strain rate (b) on the surface of the sample, and (c) on slices through the sample.

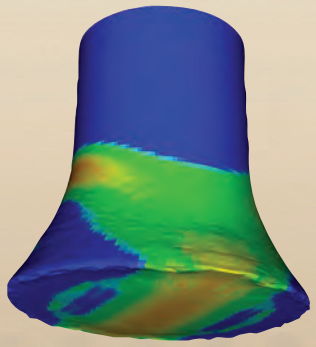

Figure 2. Simulation of a Taylor cylinder impact experiment showing plastic strain rate localization and the influence of plastic anisotropy, with coarse-scale and fine-scale state descriptors distributed as in Fig. 1.

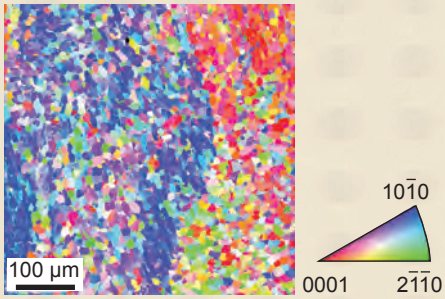

Figure 3. Electron backscatter diffraction data, showing lattice orientation in the α phase of a Ti-6Al-4V sample. The plot is colored according to the crystal plane normal to the sample surface.

computations informed by experimental data including measured microstructural information for the multiphase Ti-6%Al-4%V (Ti-6Al-4V) alloy (Fig. 3). Initial development focused on Ti-6Al-4V, given its widespread use and the availability of relevant experimental data. Software is developed in a component-oriented fashion, making use of tools that enhance parallel load balancing through task parallelism.

Relevance to LLNL Mission

The project aligns directly with the processing for performance and fracture components of the Engineering Simulation Roadmap and with Stockpile Stewardship Science needs identified in the more recently articulated LLNL Science and Technology Roadmap. Through the advancement of high-fidelity simulations and novel computational methods, the effort also aligns with high-performance computing and simulations aspects of LLNL's Science, Technology, and Engineering Pillars. We provide a more predictive modeling framework for a programmatically important class of materials, helping to close an identified capability gap.

FY2009 Accomplishments and Results

In FY2009 we focused on increasing model fidelity by accounting for more detailed evolution of the state within the polycrystalline material. Within the efficient multiscale framework, we developed a method for evolving the probability density distribution of crystal lattice orientation based on finite elements over orientation space and discrete harmonics (Fig. 4). Evolution is governed by a partial differential equation over a non-Euclidean space, with nonlocal terms from twinning. The polycrystal level model can be either a simpler Taylor calculation or the Visco-Plastic Self-Consistent (VPSC) scheme developed at Los Alamos National Laboratory (LANL), which has been calibrated to a variety of materials of interest.

Deformation heterogeneity has been captured by discretizing individual grains in a polycrystal (Fig. 5), though this approach is computationally expensive and is not yet amenable to treating deformation by twinning. Twinning can be captured using a VPSC based approach, which also includes grain level deformation heterogeneity in the polycrystalline material.

Related References

1. Barton, N. R., J. V. Bernier, and J. K. Edmiston, "Bringing Together Computational and Experimental Capabilities at the Crystal Scale," invited presentation at *Shock Compression in Condensed Matter – 2009*.
2. Barton, N. R., J. Knap, A. Arsenlis, R. Becker, R. D. Horning, and D. R. Jefferson, "Embedded Polycrystal Plasticity and Adaptive Sampling," *International Journal of Plasticity*, **24**, pp. 242–266, 2008.
3. Bernier, J. V., N. R. Barton, and J. Knap, "Polycrystal Plasticity Based Predictions of Strain Localization in Metal Forming," *Journal of Engineering Materials and Technology*, **130**, 2008.
4. Barton, N. R., "Novel Algorithms in Computational Materials Science: Enabling Adaptive Sampling," *ASCR PI Meeting, U.S. DOE Office of Science HPCSW*, 2008.
5. Barton, N. R., J. V. Bernier, R. A. Lebensohn, and A. D. Rollett, "Chapter 11: Direct 3D Simulation of Plastic Flow from EBSD Data," in Electron Backscatter Diffraction in Materials Science, 2nd edition, Springer, 2009.

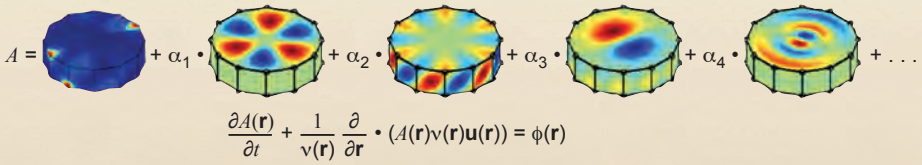

Figure 4. Schematic of the expansion of the probability distribution of crystal orientations in terms of discrete harmonics for the case of hexagonal crystal symmetry, such as in beryllium, magnesium, and zirconium.

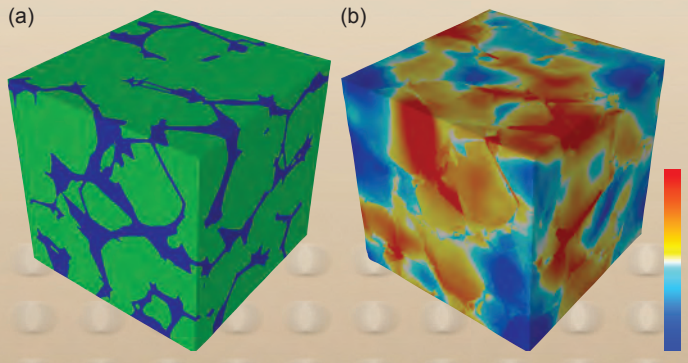

Figure 5. Finite element calculation performed using ALE3D, showing (a) phase distribution and (b) strain localization with the average plastic strain rate seen in the white/gray areas.

Integrated Analysis and Simulation Software Tools for Calibration and Validation of Crystal-Scale Material Models

Joel V. Bernier
(925) 423-3708
bernier2@llnl.gov

Novel diffraction-based methods for experimental mechanics are providing unprecedented levels of detail in the coevolution of microstructure and micromechanical state in deforming crystalline materials, such as structural metals, ceramics, and rock. Engineers at LLNL are concurrently working on novel constitutive models and simulation frameworks with increasing levels of physical detail, advancing the state of computational mechanics. There is, however, a dearth of fundamental software tools suitable for integrating experimental and simulated data.

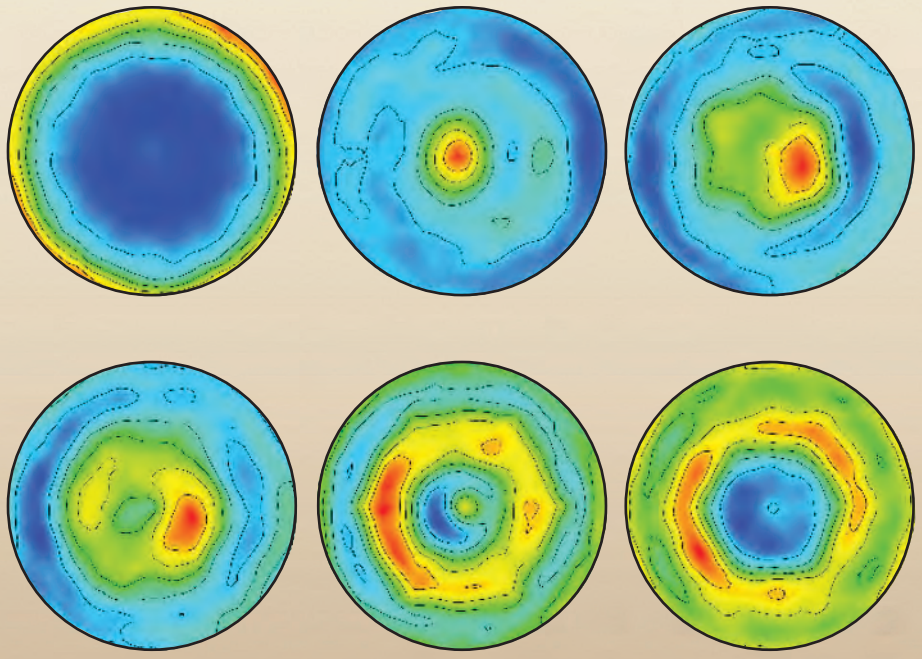

Figure 1. Reconstructed pole figures for a specimen of magnesium alloy AZ31 prior to an *in situ* deformation experiment. The underlying orientation distribution function was obtained by inverting experimental data onto a finite element mesh over the orientation space. The indices by row from the top left are: {001}, {100}, {110}, {111}, {112}, {113}. The color map indicates multiples of the uniform distribution with blue at 0 and red at 3; this normalization implies that the mean value of each pole figure is unity.

Of the few tools that exist, most were generated on *ad hoc* bases and lack the robustness and modularity necessary to make them more widely applicable and accessible to new users. This hampers critical validation and verification procedures for advanced material models, as well as collaborations seeking to leverage LLNL simulation codes. The goal of this project is to bridge this gap by producing an open-source software toolkit for reducing and analyzing data from both experiments and simulations.

Project Goals

This project is a continuation of an FY2008 effort that focused on producing the core software library. The functionalities include:

1. Experimental diffraction data reduction for flat panel detectors:
   a. Calibration;
   b. Lattice strain extraction;
   c. Pole figure inversion (quantitative texture analysis); and
   d. Strain pole figure inversion (quantitative strain/stress analysis).
2. Simulation data reduction:
   a. Data extraction from ALE3D;
   b. Discrete orientation distributions (quantitative texture analysis); and
   c. Lattice strain/stress distributions (strain partitioning/localization, phase transformations).
3. Material Point Simulator (MPS): lightweight material model evaluation using mean field theories.
4. Model parameter optimization: general harness for running the MPS or ALE3D within a nonlinear optimization framework.

The goals of the FY2009 effort were twofold: 1) to produce user interfaces for calibrating flat panel detectors (as used at synchrotron user facilities),

running the MPS, and viewing pole figures and orientation distribution functions; and 2) to refine the core software routines based on user feedback. This software has been released for unlimited distribution.

Relevance to LLNL Mission

This contribution supports ongoing work under LLNL's Engineering Simulation and Measurement Technology Roadmaps. Specifically, this software toolkit will supplement simulation efforts toward understanding the fracture and strength of metals, as well as experimental characterization of relevant microstructural features, such as orientation distributions and intergranular stresses. In addition, the software will benefit users of materials science beamlines at synchrotron user facilities throughout the DOE complex, such as at the Advanced Light Source at Lawrence Berkeley National Laboratory, and the Advanced Photon Source at Argonne National Laboratory. Clear, simple interfaces, graphical where applicable, are critical to the accessibility and utility of this toolkit.

FY2009 Accomplishments and Results

We are able to exercise material models using the MPS as well as ALE3D, extract the relevant history variables, and create data metrics such as orientation distributions, which are readily comparable to experimental results. The user interface provides graphical output as the simulation runs, updating any number of specified responses such as stress-strain response, pole figures, and phase/twin volume fractions.

Figure 1 shows screenshots of the basal plane pole figure, stress-strain time history, and twin volume fraction time history for a virtual magnesium sample subject to uniaxial compression. Similar distributions can be constructed from experimental data, which may in turn be used to verify the model performance. A framework for parameter optimization using the MPS is provided as well.

The software toolkit produced under this project comprises a library of core routines that facilitate several fundamental data visualization analysis tasks, including simple graphical user interfaces suitable for non-expert users.

Figure 2 shows calibration results for an elasto-viscoplastic constitutive model for magnesium.

Related References

1. Bernier, J. V., M. P. Miller, and D. E. Boyce, *J. Appl. Cryst.,* **39**, pp. 697–713, 2006.
2. Barton, N. R., J. V. Bernier, and J. K. Edmiston, *Proceedings of the 9th Conference of the American Physical Society Topical Group on Shock Compression in Condensed Matter*, pp. 73–78, 2009.

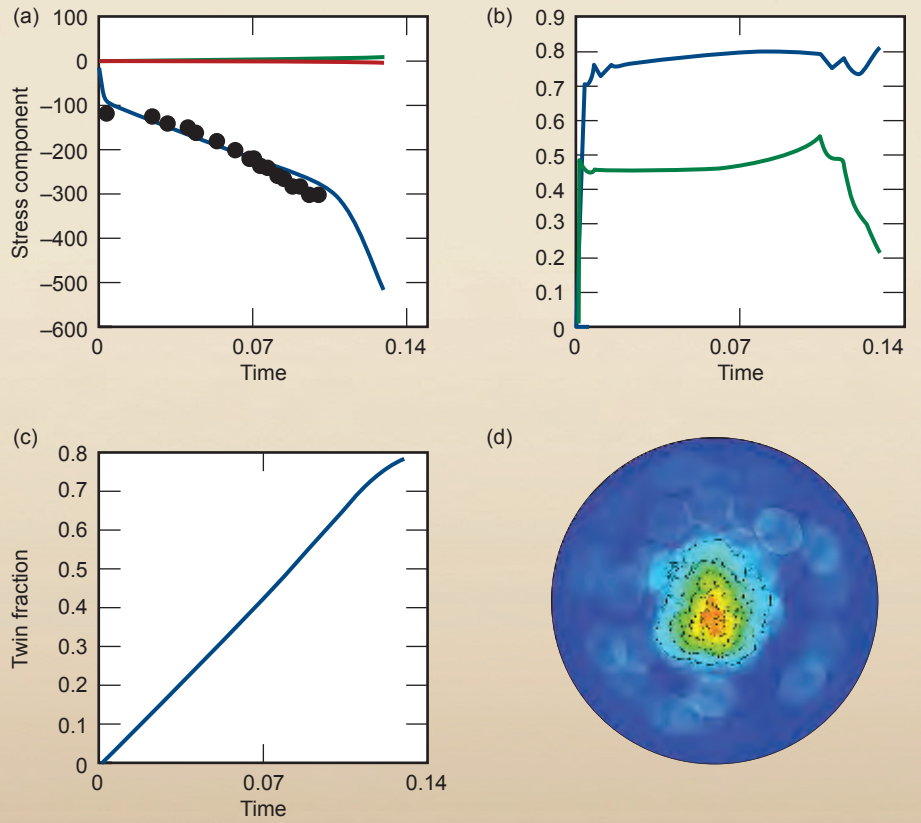

Figure 2. Calibration results for an elasto-viscoplastic constitutive model for magnesium that captures the {1012} <1011> twinning mechanism using the material point simulator. An aggregate of 1302 crystals representing the preferred orientation described by the pole figures in Fig. 1 was subject to uniaxial compression using a Taylor linking assumption (uniform deformation rate). (a) Aggregate averaged normal stress components (red and green are perpendicular to the compression axis; blue is parallel). The black points represent experimental data. (b) Decreases in effective plastic deformation rate. (c) Evolution of twin volume fraction with deformation. (d) Simulated basal {001} plane pole figure using the same scale as in Fig. 1.

Plasticity at High Pressures and Strain Rates using Oblique-Impact Isentropic-Compression Experiments

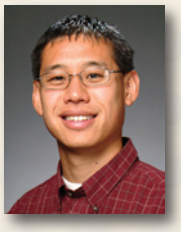

Jeffrey N. Florando
(925) 422-0698
florando1@llnl.gov

Various aspects of LLNL's national security mission depend on accurate computer code simulations of materials in high strain-rate plastic flow (*i. e.*, nonreversible deformation) under conditions of high hydrostatic pressures. While progress has been made in recent years, especially at the extreme cases of pressure and strain rate, there is still an uncertainty in understanding the strength of materials under conditions of combined high strain rate (10^4 to 10^6 s^{-1}) and high pressure (1 to 100 GPa).

Current strength models used in simulations include some physically based models such as the Mechanical Threshold Stress formulation, which has over 20 parameters. The uncertainty in the values for these parameters as well as values for the parameters in other physically based models is under question due to the inherent difficulties in conducting and extracting high-quality experimental data in the high pressure and high strain rate regimes. The experimental studies of material strength at these pressure and strain rate regimes will further the understanding of the underlying physical strength mechanisms needed for accurate material strength models.

Project Goals

The goal of this project is to develop an oblique-impact compression experiment using windowed interferometry (Fig. 1) to measure the strength of materials under a condition of combined high strain rate (10^4 to 10^6 s^{-1}) and high pressure (1 to 100 GPa). The oblique impact allows for a measurement of the strength properties under pressure, and by using windowed interferometry, the pressure is maintained during the measurement and higher pressures can potentially be achieved. The strength data will then be used to refine and enhance current strength models. When completed, this work will increase the Laboratory's ability to develop predictive strength models for use in computer code simulations.

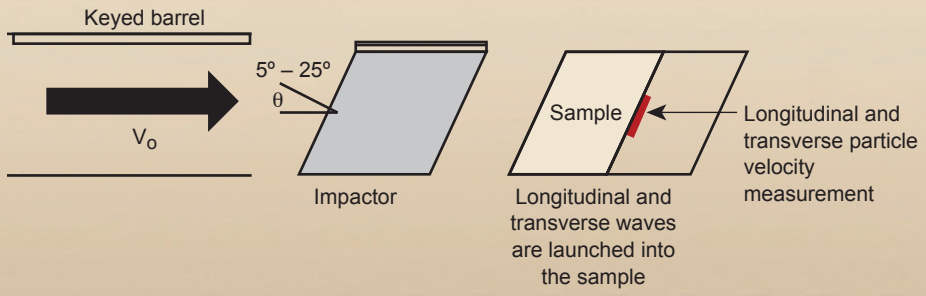

Figure 1. Oblique-Impact compression experiment using windowed interferometry.

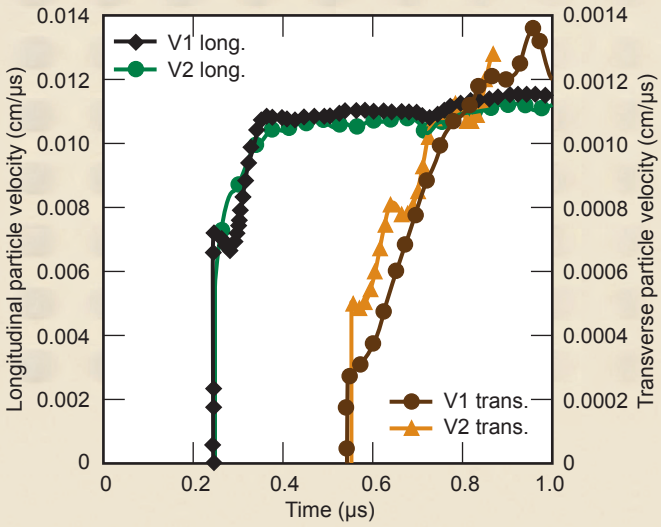

Figure 2. Experimental longitudinal and transverse waves measured at the vanadium/sapphire interface for two samples.

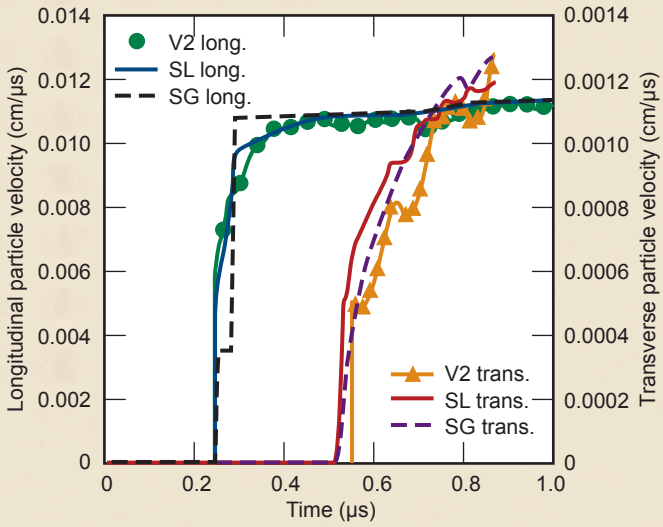

Figure 3. Comparison between the experimental data and the simulations results using two strength models, the Steinberg-Lund (SL) and the Steinberg-Guinan (SG) models.

Relevance to LLNL Mission

This experiment, including understanding and simulating the strength of materials under dynamic loading conditions, is directly aligned with the Materials Pillar within LLNL's Science and Technology Five Year Strategic Roadmap. In addition, this work intersects with the roadmap's Stockpile Stewardship Science thrust area.

FY2009 Accomplishments and Results

In this fiscal year, we have performed experiments on vanadium (V) samples, which allowed us to achieve a more reproducible velocity signal than previous experiments on copper. In addition, simulations were performed using ALE3D to examine how different strength models compare with the experimental data.

Experimental results. We have performed experiments on V samples backed by a sapphire window on the 2-in. keyed-barrel gas gun at Brown University. The results from the two experiments, both using a 1.5-mm-thick sample backed by a 10-mm sapphire window, are shown in Fig. 2. The samples were impacted at 200 m/s with a Ta-10% W target. In comparison to previous data, the transverse velocity signals are much smoother with less noise. While there is a slight discrepancy between the two experiments in the initial portion of the transverse wave signals, the fact that the transverse velocities reach a similar level at later times is indicative that the strength of the two materials is nominally the same.

Simulation results. The experimental results have been compared with the simulation results using two models, the Steinberg-Guinan (SG) model, and the Steinberg-Lund (SL) model, as shown in Fig. 3. With both models the experimental results can be reproduced by using parameters that predict a flow stress of approximately 600 MPa at the time of the arrival of the transverse wave. The main difference between the two models is that the SG is strain rate independent while the SL model has strain rate dependency built into the model. The strain rate dependence in the SL model allows the model to better match the experimental longitudinal wave data, as well as the sharp increase seen in the experimental data when the transverse wave arrives.

Related References

1. Remington, *et al., Mat. Sci. and Tech.*, **22**, p. 474, 2006.
2. Follansbee, P. S., and U. F. Kocks, *Acta Metall.*, **36**, p. 81, 1988.
3. Clifton, R. J., and R. W. Klopp, ASM Handbook 9th ed., **8**, p. 230, 1985.
4. Espinosa, H. D., *Rev. of Sci. Instruments*, **67**, p. 3931, 1996.
5. Florando, J. N., *et al., Proceedings of the American Physical Society Topical Group on Shock Compression of Condensed Matter*, 2009.

Advanced Composite Modeling Capabilities for ALE3D

Michael J. King
(925) 422-0627
king74@llnl.gov

Composite structures are increasingly being used in advanced weapon and armor systems, as well as in a variety of other applications. We had previously implemented several composite material models in ALE3D (a 3-D arbitrary Lagrangian-Eulerian, or ALE, multiphysics LLNL hydrocode) by porting constitutive models from DYNA3D (an explicit 3-D structural dynamics code). Over the past two years, we extended our composite modeling capabilities by adding more realistic failure mechanisms, implementing strain-driven progressive damage, implementing layer-specific damage, and creating tools for estimating homogenized composite material properties (Fig. 1). We also began investigation of finite deformation kinematics necessary for modeling many anisotropic composite materials and initiated experimental work studying thermal dependence, degradation, and damage of composites.

Project Goals

Our goal is to be able to efficiently model composite materials under a wide variety of environments, including large and/or high velocity deformations. Specific goals include:

1. capturing the failure modes specific to different types of composites with different layups, such as fiber breakage, fiber buckling, and through-thickness crush;
2. modeling states of partial damage, and allowing damage to evolve progressively within an ALE framework;
3. capturing the damage to individual layers or fiber families;
4. accurately modeling finite deformations of composites in an ALE framework; and
5. incorporating thermal sensitivity of composite properties and thermally-driven or thermally-assisted damage.

In addition, we require experimental characterization of composite material properties, tools for rapidly estimating appropriate properties of layups, and experimental validation of our models.

Relevance to LLNL Mission

Modeling composite structures before, during, and after failure is necessary for many LLNL programs. Applications include next-generation composite munitions; magazines, damage containment, and insensitive munitions; pressure vessels; rocket motors; and armors. By extending our modeling capabilities to composites, this work enhances LLNL's core competency in simulation of engineering structures under extreme loading conditions.

FY2009 Accomplishments and Results

Implementation of multilayer damage mechanics was a key accomplishment. Previous composite material models were homogenized—a single damage criterion was established for the entire composite layup, and damage to any layer affected strength in every direction. This approach is inaccurate for composites with a relatively small number of fiber families (*e.g.*, woven Kevlar composites). The new multilayer damage mechanics represents a generalization of the homogenization techniques used in previous models. The kinematic formulation assumes in-plane isostrain and out-of-plane

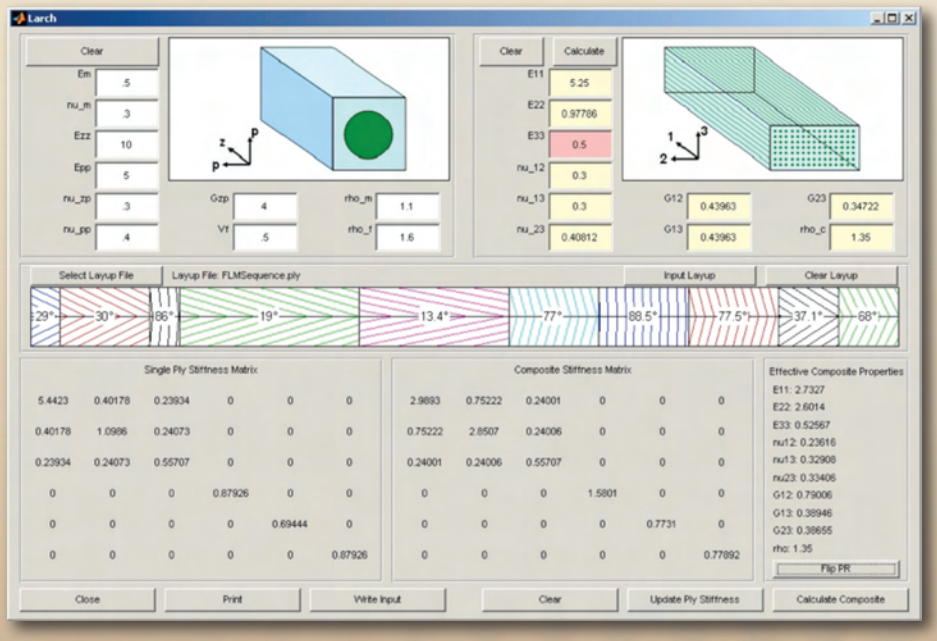

Figure 1. User interface for the LLNL Analytical fiber Reinforced Composite Homogenizer (LARCH), a tool for rapidly estimating composite properties from the properties of its components and layup.

isostress across all layers. The strain and damage in each layer evolves separately according to this kinematic framework. Delamination is also supported. In this manner, it is possible to track the effects of different levels of damage to different fiber families and predict the progressive failure of the entire composite (Fig. 2). This model was implemented into the ALE3D version 4.10 release and is extensively documented in its manual.

Finite deformation in an ALE framework was also explored. Large strains and rotations are challenging to capture in an ALE framework because tensors like a deformation gradient are difficult to maintain accurately in the presence of advection. Several potential algorithms were identified that may prove effective, including modified stretch tensors and quaternions to track material deformations. This study has laid the groundwork for these algorithms to be implemented and tested in future work.

Finally, we have initiated a study of the thermal response of composites. Composite properties (especially strength) change at temperature, and sufficient time at temperature can induce damage, through softening or charring of the composite matrix. In FY2009, a related project began experiments to measure these behaviors, consisting of axial compression-to-failure tests on composite tubes held at a given temperature after a prescribed thermal history (Fig. 3). This data will enable thermal dependence and damage of carbon fiber composites to be implemented into models in the future.

Future work in this field can entail implementing, testing, and improving the finite deformation algorithms, adding thermal effects into the material models, or focus on modeling ply-by-ply mechanics to accurately simulate the localized bending response of thin composite structures.

Related References

1. Chang, F., and K. Chang, "A Progressive Damage Model for Laminated Composites Containing Stress Concentrations," *Journal of Composite Materials*, **21**, pp. 831–855, 1987.
2. Christensen, R., and E. Zywicz, "A Three-Dimensional Constitutive Theory for Fiber Composite Laminates," *Journal of Applied Mechanics*, **57**, pp. 948–955, 1990.
3. Christensen, R., "The Numbers of Elastic Properties and Failure Parameters for Fiber Composites," *Transactions of the ASME: Journal of Engineering Materials and Technology*, **120**, pp. 110–113, 1998.
4. Holzapfel, G. A., Nonlinear Solid Mechanics: A Continuum Approach for Engineering, John Wiley & Sons, Chichester, England, 2001.
5. Tang, C. Y., W. Shen, L. H. Peng, and T. C. Lee, "Characterization of Isotropic Damage Using Double Scalar Variables," *International Journal of Damage Mechanics*, **11**, 2002.

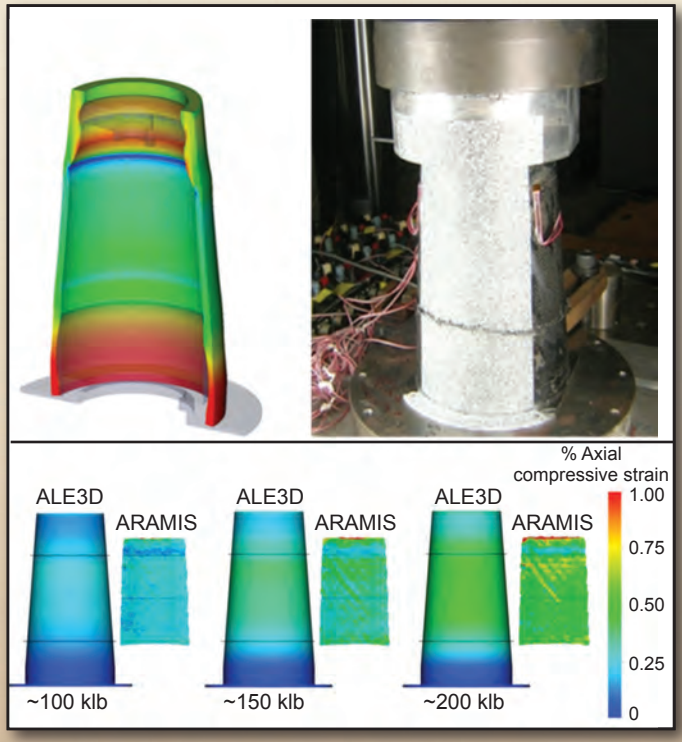

Figure 2. Structural analysis (ALE3D) of a conical composite case section and comparison to axial compression test data (ARAMIS).

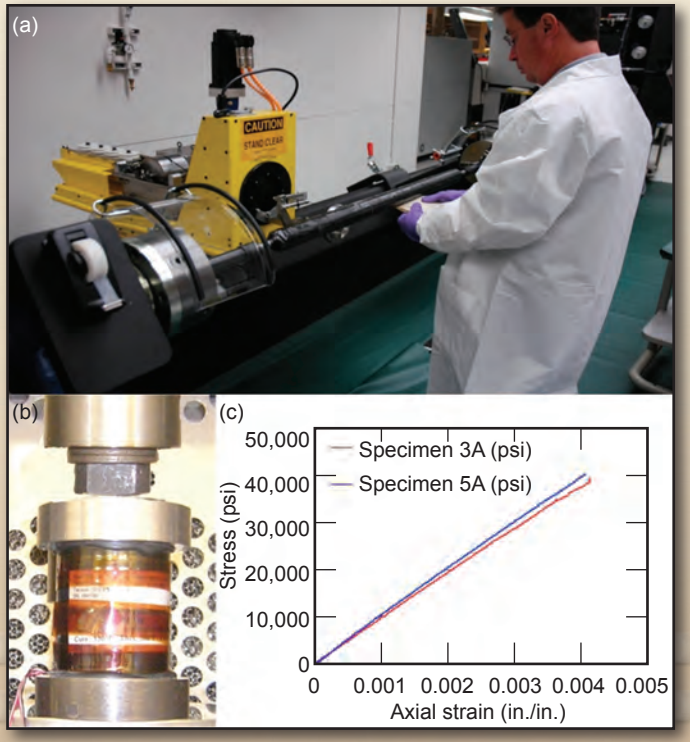

Figure 3. Composite thermal damage tests: (a) photograph of 2-in. composite tubes being manufactured; (b) instrumented composite tube being compressed in an oven; (c) stress-strain response of composite tube at temperature up to failure.

Lagrange Multiplier Embedded Mesh Method

Michael A. Puso
(925) 422-8198
puso1@llnl.gov

Our objective is to permit more effective simulation of complex phenomena by using multiple, but more easily generated, meshes. Figure 1 shows a simple example where a fluid is flowing past a moving solid mesh. The two meshes could in fact be processed by two distinct simulation codes, using meshes that enhance their respective robustness. This general class of method is known as embedded mesh. A number of different approaches exist, yet many have not become popular due to a variety of side effects. Most of these approaches have also focused on coupling finite volume grids. In our project, the focus is on the coupling of Arbitrary Lagrangian-Eulerian (ALE) type finite element meshes without the use of an overset grid. Close attention is paid to the accuracy and efficiency to make our method practical. The new methods are currently being implemented in our new FEusion software library and will be modular and documented for potential utilization in other LLNL codes.

Project Goals

We seek a general software tool to interface embedded meshes. The formulation as implemented should accommodate the computational efficiency expected of an explicit time integration method. It should also be extensible to different physics and finite element discretizations. Two model problems are the focus:

1. Fluid structure interaction of solid and fluid meshes. An example would be a Lagrange shell mesh subjected to an air blast on an ALE or Eulerian mesh (Fig. 2). Our approach would obviate the need for conformal meshing of the fluid domain to the structural geometry and potentially be more robust.
2. Coupled solid-electrodynamics of a moving conductor in an air background grid (Fig. 3). Applications of this phenomenon would be the rail gun or flux compression generator.

Relevance to LLNL Mission

The methodology developed in this project will enhance our computational tools, permitting more robust simulation of complex, real-world engineering models in support of many LLNL programs.

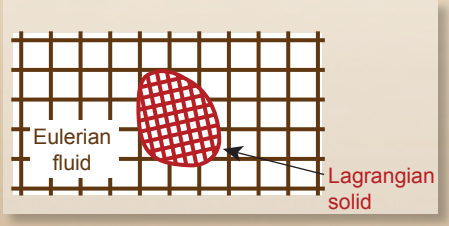

Figure 1. Schematic application of an embedded grid method to model the interaction of a solid body with a surrounding fluid. The software couples the fluid and solid along their common boundary.

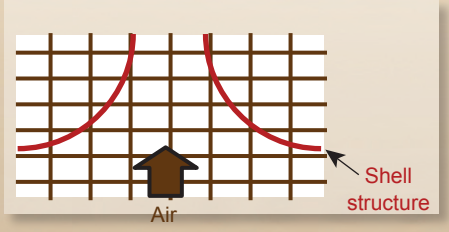

Figure 2. Blast loading on a shell structure.

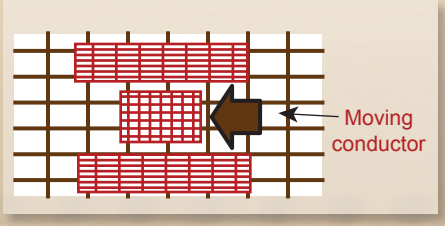

Figure 3. Moving conductor on an air background grid.

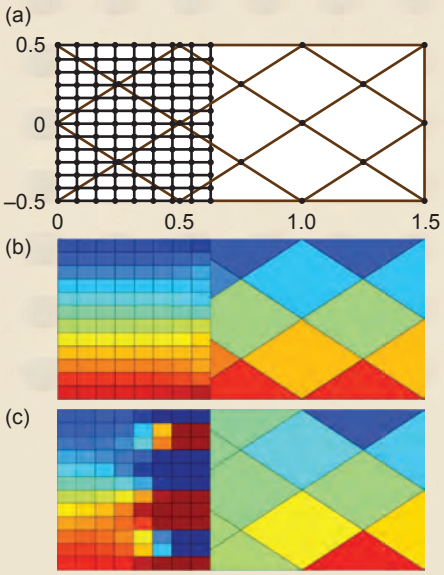

Figure 4. (a) Overlapping fine (black) and coarse (brown) meshes. (b) Stress at interface with a soft material on fine and coarse meshes. (c) Stress at interface with stiff material on fine mesh and soft material on coarse mesh.

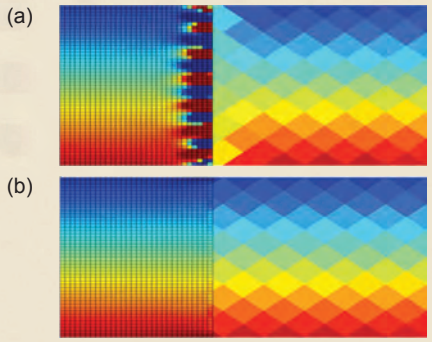

Figure 5. Stress at interface with stiff material on fine mesh and soft material on coarse mesh: (a) using standard approach, (b) using new modified approach.

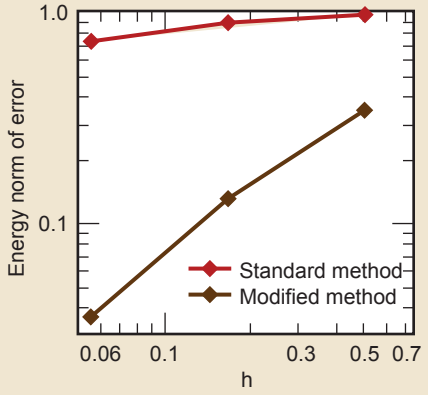

Figure 6. Energy norm of error vs. element size for stiff material on fine mesh and soft material on coarse mesh. Modified method converges at optimal rate.

FY2009 Accomplishments and Results

As year one of the project, initial development was begun for the FEusion embedded mesh coupling software. The data model accepts a superposed mesh (*e.g.*, Lagrange solid) and a background mesh (*e.g.*, ALE fluid). The software identifies overlaps, resulting voids on the background grid, and the strains on the "cut" background cells. It then generates constraint equations that enforce velocity continuity and associated transformation operators along the boundary between the two meshes. An interface to LLNL's ALE3D code was created and a developers guide written detailing the specific data structures exchanged with FEusion. A MATLAB implementation was also developed as a numerical test bed for the new coupling methods.

Most of the formulation developed so far has been for fluid structure interaction. A Lagrange multiplier is defined on the solid surface mesh and used to enforce velocity continuity between the fluid and solid. A special dual Lagrange multiplier yields efficient monolithic coupling. Typical model applications will have a background fluid grid that is finer than the superposed solid mesh because of the needed resolution.

Our MATLAB results in Fig. 4 (b) show that stress is smoothly captured across the fluid and solid boundaries for this simple example. Nonetheless, some models will have a coarse fluid mesh and this can result in so-called mesh locking [Fig. 4(c)]. This known pathology of many embedded grid methods can be avoided using an intermediate mesh. Figure 5 shows a finer mesh representation of the stiff and soft material problem with results from the original and modified approaches. The new modified approach eliminates the stress oscillations. Optimal convergence is documented in Fig. 6.

Related Reference

Puso, M. A., "A 3-D Mortar Method for Solid Mechanics," *International Journal for Numerical Methods in Engineering*, **59**, pp. 601–629, 2004.

FY2010 Proposed Work

Our proposed FY2010 work is as follows:

1. **Interface FEusion with ALE3D.**
2. **Extend application to handle shell solid models.**
3. **Modify advection routines in ALE3D to accommodate "cut" fluid cells.**
4. **Interface FEusion to Diablo for solid-electrodynamics problem.**

Physics of Local Reinitiation and Morphological Evolution of Mitigated Sites for Ultraviolet Optics

James S. Stölken
(925) 423-2234
stolken1@llnl.gov

Small defects in laser optics can grow due to exposure to high-power fluence, both degrading the beam quality and ultimately threatening the structural integrity of the optic. Mitigation strategies are under development, yet recent testing of high-fluence operations has revealed ever-more restrictive requirements for the mitigation process. The objective of this work is to develop and implement a predictive, physics-based model to accurately control the mass transport and thermal-induced stress associated with laser-based material processing of high-fluence ultraviolet optics. Mitigated site attributes associated with re-initiation, crack formation, and downstream intensification have been identified that require increasingly sophisticated physics models and experimental programs. The basic material science that governs these attributes is not well understood and lies outside existing current predictive capabilities.

We propose to integrate advanced diagnostics, materials characterization, and fundamental computational capability to clarify the origins and means to minimize or eliminate these effects.

Project Goals

The optics damage mitigation process uses laser-induced heating, melting, and evaporation to remove damaged material, heal subsurface cracks, smooth the surface, and anneal residual stress in the affected region. Development to date has been driven primarily by experimental work supported by empirical models that provide only rough guidance for control of temperature and material transport. Present technology has limited

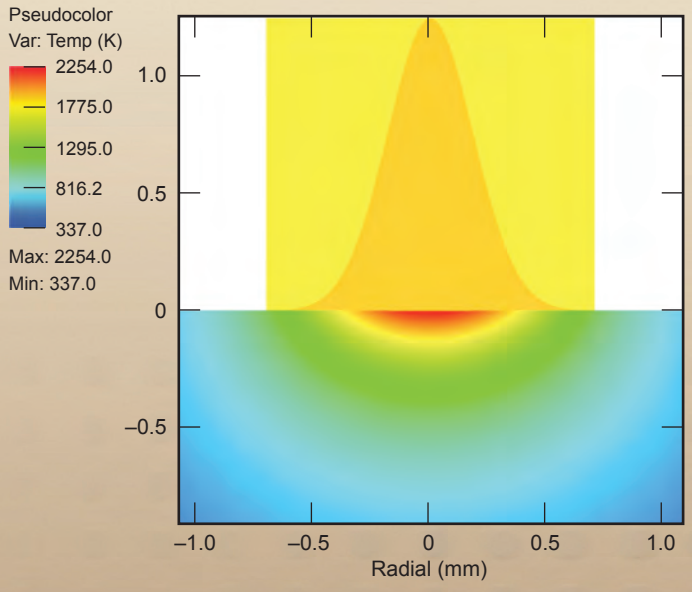

Figure 1. Simulated laser heating of silica with a CO_2 laser. The upper half of the image depicts the Gaussian spatial distribution of intensity within the laser. The lower half depicts a pseudo-color plot of the temperature distribution.

ability to control size, morphology, and damage threshold of a mitigated site, which fundamentally impacts yield and performance. We expect to develop a stronger scientific basis and advanced diagnostics to guide development of mitigation techniques and extend the understanding of laser interaction with optical materials.

Relevance to LLNL Mission

High-energy laser systems are essential tools for the Stockpile Stewardship Program and other national security applications, as well as for inertial confinement fusion as an advanced energy concept. High-energy lasers are also a key scientific element of high-energy-density research at LLNL. This work will provide an enabling technology for these systems to operate efficiently, reliably, and affordably with development of robust ultraviolet-optics mitigation technologies backed by reliable computational models.

FY2009 Accomplishments and Results

We developed an imaging technique to accurately measure temperature (±5%) and thermal conductivity (±10%) of 4.6- and 10.6-µm CO_2 laser-heated optical materials (SiO_2, Al_2O_3, LiF, $MgAl_2O_4$) at spatial and temporal resolutions of 200 µm and 30 ms, respectively. Measured transient temperature maps (Figs. 1 and 2) were in excellent agreement with ALE3D thermal transport models, which included a multi-group diffusion model for radiation transport. Microstructural evolution and residual stress in SiO_2 caused by laser heating above glass transition, were investigated using confocal Raman microscopy, comparing well with predictions from ALE3D. Finally, analytic models derived from a commercial fluid dynamics code were used to predict surface roughness relaxation caused by laser heating on optically damaged SiO_2 surfaces. This work produced three archival journal articles. These results were part of three presentations at an international symposium on laser damage.

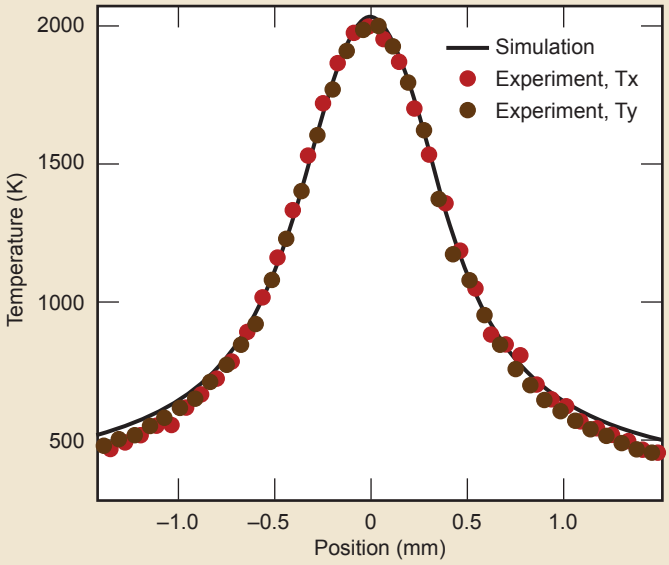

Figure 2. Comparison of simulated and measured surface temperature profiles for CO_2 laser heating of silica. Excellent agreement of the axisymmetric simulation with the data is found for the two orthogonal line-outs.

FY2010 Proposed Work

In FY2010 we will 1) complete our combined hydrodynamics and propagation model connecting visco-capillary surface physics and evaporation on fused silica surfaces to downstream modulation of incident light; 2) develop vapor-phase transport and multigroup diffusion radiation approximations; 3) explore new approaches to mitigation involving active environments and mid-infrared irradiation using our modeling predictions; 4) probe evolution of the glass state and microstructure as it relates to residual defects and stress using characterization techniques such as confocal Raman and time-resolved photoluminescence microscopy; and 5) develop *in situ* diagnostics based on our thermographic probe for potential use in laser mitigation facilities.

Simulation Visualization and Data Management

Bob Corey
(925) 423-3271
ircorey@llnl.gov

Support for and enhancement of several visualization and postprocessing tools are key components of our project. These tools include the Griz finite element visualization postprocessor, the Mili data management library, and a data file manipulation tool called Xmilics. These tools are used by analysts and engineers across LLNL to interpret data from a variety of simulation codes such as DYNA3D, ParaDyn, NIKE3D and Diablo. We also provide support in the area of data translation tools and processes for performing intra-code calculations.

Griz remains our users' primary tool for visualizing finite element analysis results on 2- and 3-D unstructured grids. Griz provides advanced 3-D visualization techniques such as isocontours and isosurfaces, cutting planes, vector field display, particle traces, and free-particles or free-nodes. Mili is a high-level mesh I/O library for computational analysis and postprocessing on unstructured meshes, providing the primary data path between other LLNL analysis codes and Griz. Mili databases are also viewable with the LLNL VisIt postprocessor. Xmilics is a utility used to combine results from multiple processors that are generated by our large parallel computing platforms.

Project Goals

The project provides ongoing support for LLNL's visualization and postprocessing tools and adds new capabilities to these tools to support evolving, multiprogrammatic requirements.

Relevance to LLNL Mission

These postprocessing tools provide important user interfaces to our simulation capabilities and are critical elements in our tool suite. Without such tools analysts would be severely limited in their ability to interpret the vast amounts of data generated by simulation and to synthesize key results.

FY2009 Accomplishments and Results

User support continues to be a high priority goal. We are currently supporting 30 to 40 active users on a variety of platforms across LLNL and some off-site users including LANL and the Naval Surface Warfare Center, Indian Head. This year we saw a high level of usage and special requests from users supporting W Program, NIF, and Global Security; *e.g.*, Griz and Mili were recently used in LIFE calculations (Fig. 1).

We added a variety of new visualization features to Griz, with the most significant being: 1) enhancements to support strain rotation calculations for shell elements; 2) enhanced support for

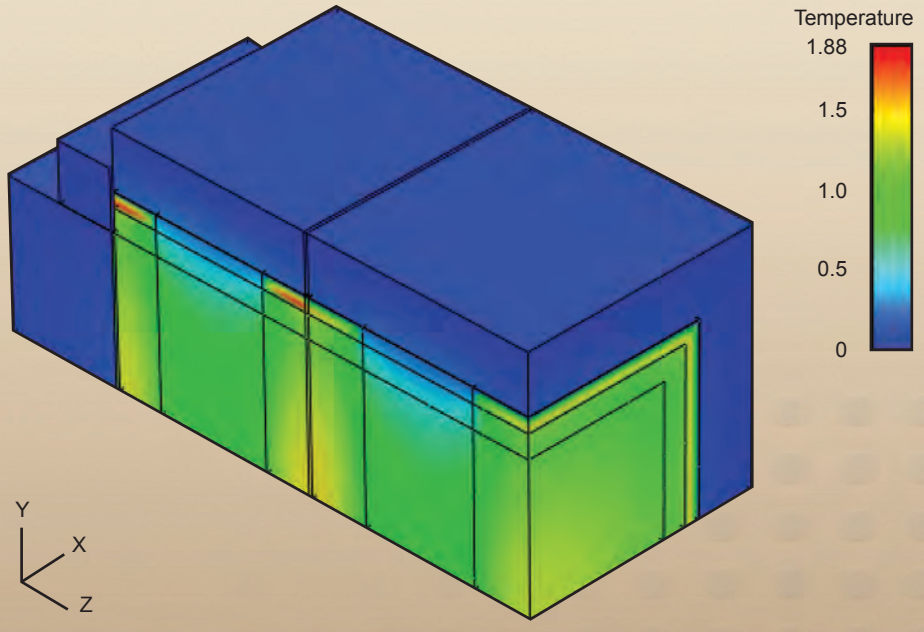

Figure 1. Griz rendering of a thermal model for a high-repetition rate laser that could be used in the LIFE project for lifetime testing of optics.

running Griz from Windows platforms; 3) improvements and features to support "meshless" techniques; and 4) a new form of cut-plane to permit analysts to assess results within parts (Fig. 2).

Last year we began an effort to create a Griz-like API that interfaces to LLNL's popular VisIt parallel visualization tool. We are now working on a GUI using PyQt to function as a familiar interface to the VisIt rendering engine (Fig. 3). This *GrizIt* will give our analysts the capability to visualize very large models with VisIt, while using a more productive command structure.

We continued to make progress in migrating Mili to a modern file structure, namely Silo/HDF. The architecture is hierarchical with a separation between the Silo and Mili layers.

We are applying modern software quality engineering tools to make assessments of Griz and Mili for potential defects. We also created a new Mili Database Reader Utility that will serve as the backbone of an end-to-end regression testing process that represents the workflow most common to our analysts.

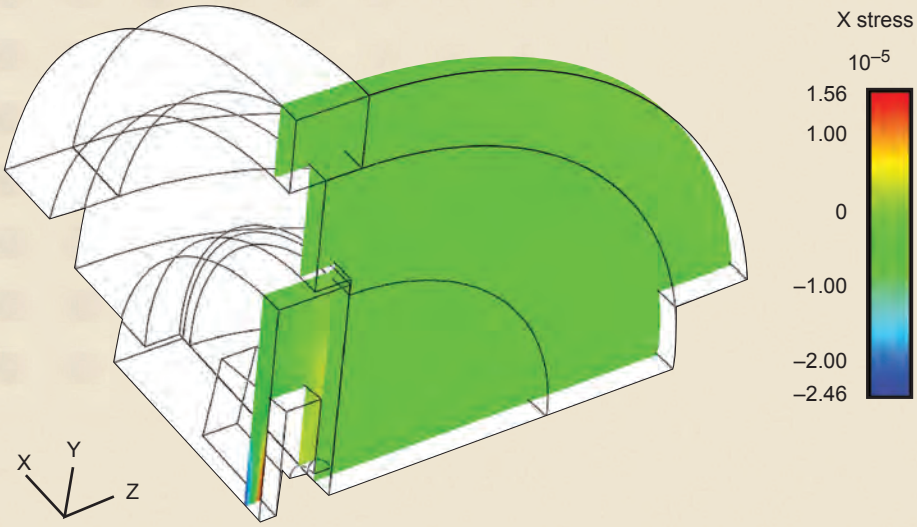

Figure 2. Example of the Griz cut-plane function applied to a ParaDyn Model.

FY2010 Proposed Work

We will continue to provide support for our user base. Efforts targeted for next year include: 1) completing a new version of the Xmilics combiner tool with support for particle methods; 2) providing Griz enhancements as part of the ParaDyn Suite 10.1 release; 3) delivering version 1.0 of GrizIt for testing by analysts; and 4) delivering end-to-end regression testing for code suites including Griz, Mili, and Xmilics.

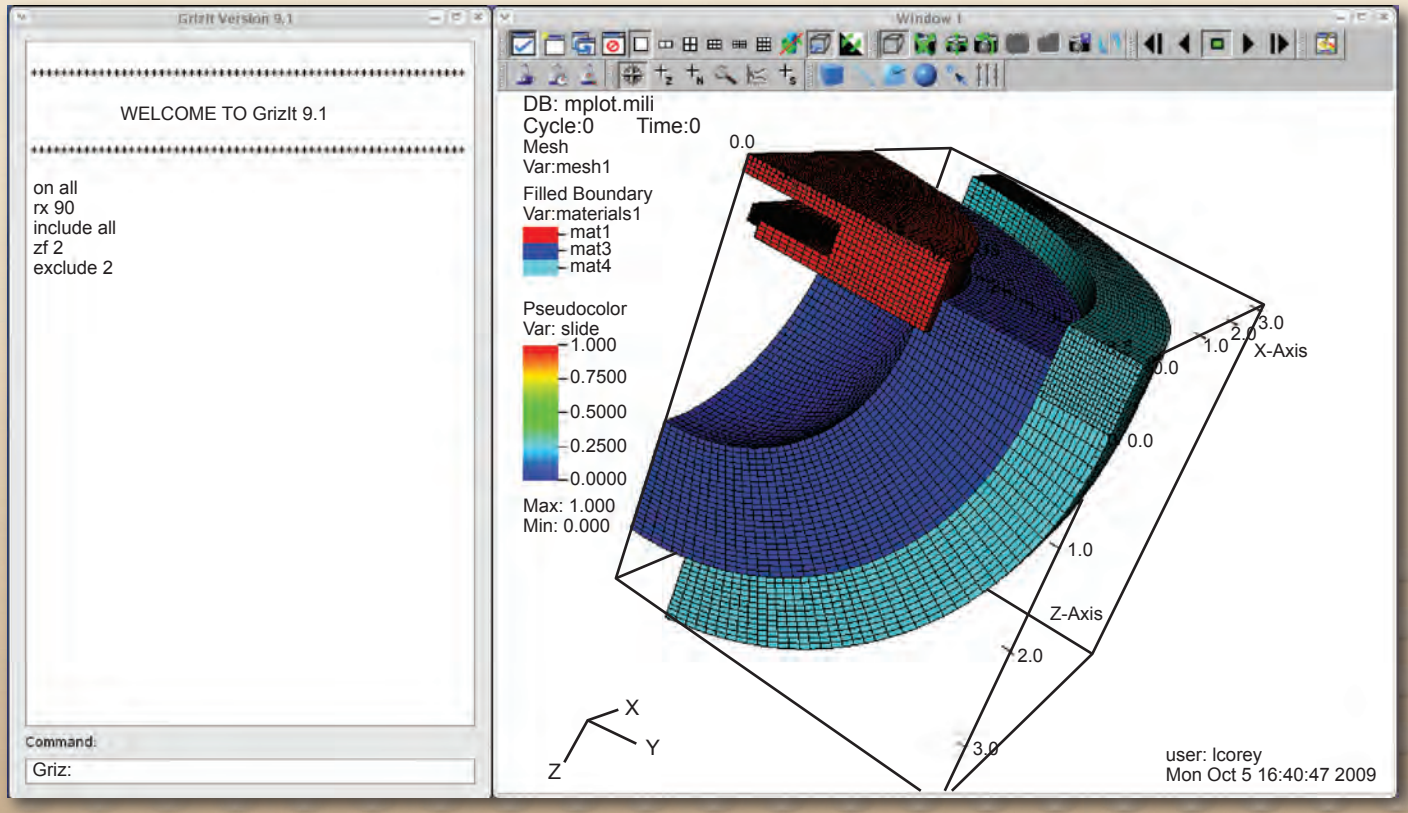

Figure 3. Example of prototype GrizIt command interface using VisIt parallel rendering engine.

New Features for Structural Elements in DYNA3D

Jerry I. Lin
(925) 423-0907
lin5@llnl.gov

Due to its ability and efficiency in modeling the nonlinear behaviors of solids, the explicit finite element code DYNA3D has long been a main computational tool at LLNL for the simulation of transient response of solid continuum and structures to fast, impulsive loadings. In addition to its original mission of supporting Laboratory activities, DYNA3D over the years has evolved to encompass other applications such as infrastructure protection, vehicle impact simulation and earth structure analysis. DYNA3D also provides the mechanics functionalities of the highly parallel ParaDyn code. This project funds the ongoing implementation of user-requested features, general technical support and documentation updates.

This project also supports the broader interagency DYNA3D activities through LLNL's Collaborator Program. The Collaborator Program grants selected users licensed access to LLNL's computational mechanics/thermal codes in exchange for their research/development results and acknowledgement. These collaborative members include our sister laboratories, U.S. government agencies, and other education/research institutions.

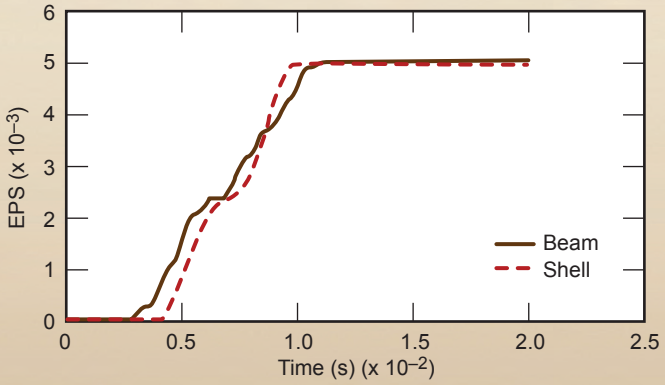

Figure 1. Comparison of equivalent plastic strains from resultant-based shell and beam element representation of a fixed-end beam subjected to a concentrated mid-span load.

Project Goals

The planned tasks include user support and code maintenance, implementation of new functionalities for program needs, enhancement of existing features, compliance to software quality assurance (SQA), and FORTRAN 95 standard.

Relevance to LLNL Mission

Many programs supported by LLNL need new/enhanced DYNA3D functionalities and technical support to complete their missions. Many of these programs and projects involve the Laboratory's collaboration with other institutions and federal agencies, such as the Los Alamos National Laboratory (LANL), Missile Defense Agency, the Naval Surface Warfare Center (NSWC), the U.S. Army Corps of Engineers, and the Department of Homeland Security.

FY2009 Accomplishments and Results

In recent years, with the expansion of DYNA3D's use in application breadth and model size, the use of structural

elements (beam, shell, and thick shell) has increased. For efficiency, some beam element formulations describe their response in terms of aggregate quantities: the total moment as a function of the beam bending. The trade-off of this "resultant-based" approach is that an analyst is left to interpret the aggregate response rather than the more familiar point-wise material behaviors, *e.g.*, the peak stress. A common point-wise response of interest is the equivalent plastic strain, a measure of permanent deformation that is often used to judge the margin from failure in ductile materials such as many metals.

Recent modeling of complex aircraft structures often uses resultant-based beam elements for efficiency. Acting upon a user request, we added an equivalent plastic strain output option to that element type. This option was derived from an analogous capability for resultant-based shell elements that already existed in DYNA3D. Due to the lack of a concise analytic expression for the equivalent plastic strain for this model, we created a computational procedure based on the plastic work. The algorithm yields good agreement with the results provided by the shell model (Fig. 1), and can also serve as a template for similar calculations for other material models. The permanent deformation of the rebar in reinforced concretes can be observed through the beam equivalent plastic strains (Fig. 2).

Important classes of LLNL simulations require the inclusion of effects arising from the natural variability of materials. For example, the local strain-to-failure of a material will vary across a part and thereby influence the evolution of its behavior under extreme loads. Often a Weibull statistical distribution is a reasonable, convenient representation of such variability. In response to analysts, our Johnson-Cook Elastic/Plastic material model was extended to accept Weibull distributions on parameters that determine fracture strain behavior.

We note that DYNA3D is also gaining features under our collaboration with NSWC and its German project partners. A new material model, Tabulated Rate-Dependent Elastic-Plastic with Fracture was integrated into DYNA3D. The inclusion of predefined inputs for common beam cross-sections from the same partner will significantly streamline model preparation for complex, stiffened structures such as ship hulls.

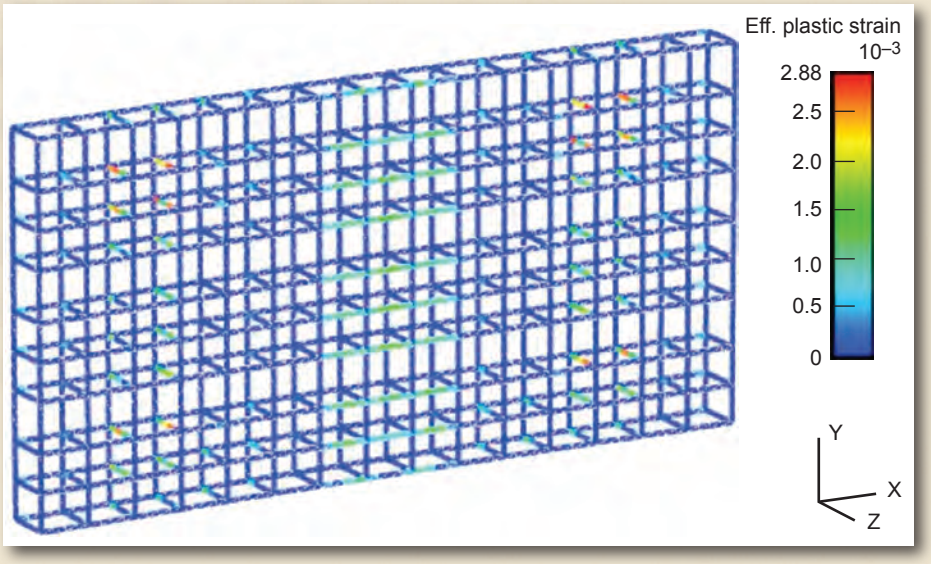

Figure 2. Equivalent plastic strain distribution in the rebar system of a reinforced concrete slab under pressure load at the mid-section. The concrete material is removed for clarity.

FY2010 Proposed Work

General technical support of our analysts for DYNA3D will continue. The extension of the existing *Closed Volume* feature to permit gas flows among multiple volumes is now scoped and awaiting further user specification of requirements. Work on hardening in material models for the resultant-based beam element will also be added.

Related References

1. Kennedy, J. M., T. Belytschko, and J. I. Lin, "Recent Developments in Explicit Finite Element Techniques and Application to Reactor Structures," *Nuclear Eng. and Design*, **97**, pp. 1–24, 1986.

2. Johnson, G. R., and W. H. Cook, "A Constitutive Model and Data for Metals Subjected to Large Strains, High Strain Rates and High Temperatures," *Seventh International Symposium on Ballistics*, The Hague, The Netherlands, April 1983.

NIKE3D Enhancement and Support

Michael A. Puso
(925) 422-8198
puso1@llnl.gov

The objective of this work is to develop, maintain, and support the implicit structural mechanics finite element code NIKE3D. New features are added to accommodate engineering analysis needs. Maintenance includes bug fixes and code porting to the various platforms available to engineering analysts. User support includes assisting analysts in model debugging and providing general analysis recommendations.

Project Goals

Ongoing code support requires new features to meet our engineering community's user demands. Our goals included the following highlights in NIKE3D development:

1. add bucket sort to mortar contact to speed up contact searching;
2. add new Hierarchical Data Format (HDF) stress initialization restart for coupling to ParaDyn;
3. integrate key NIKE3D contact and solver features to Diablo; and
4. perform an extensive benchmarking study using NIKE3D and Diablo.

Relevance to LLNL Mission

Structural analysis is a core competency of LLNL's Engineering. In-house maintenance, support, and code enhancement are crucial for meeting Engineering's many analysis needs. NIKE3D, in particular, is a premier code for handling difficult non-linear static structural analysis problems.

FY2009 Accomplishments and Results

The mortar contact algorithms previously added to NIKE3D have proven very successful in solving many difficult production analyses and are now

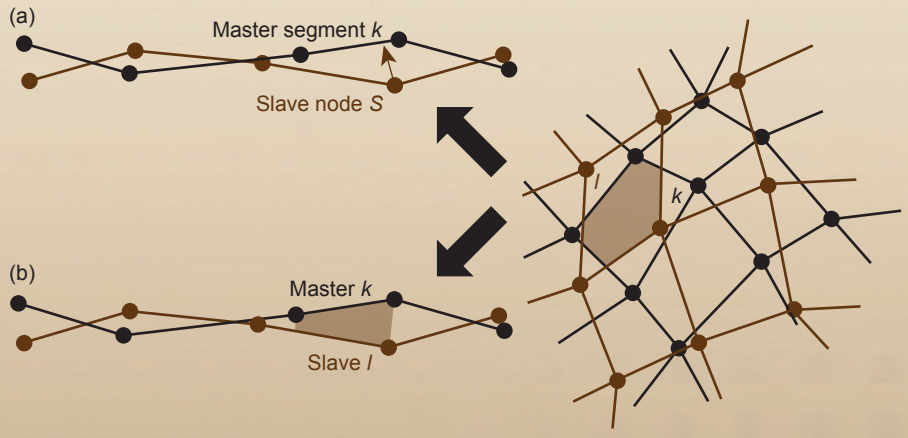

Figure 1. Illustrations of (a) node-on-segment contact algorithm, using a closest point approach to gather node-segment pairs and compute the associated gap between slave node *S* and master segment *k*; and (b) segment-to-segment contact algorithm, gathering segment-segment pairs and computing weighted volume between slave segment *l* and master segment *k*.

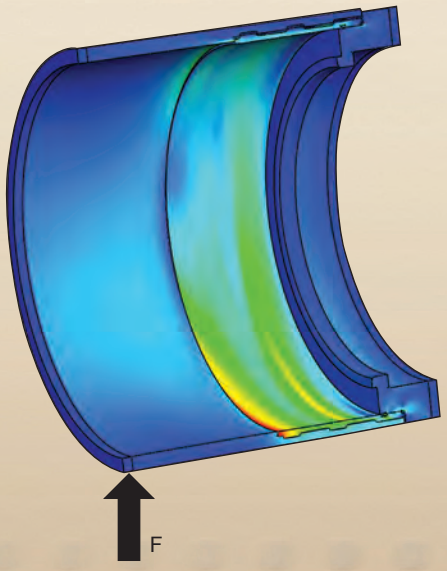

Figure 2. Aft coupler joint analysis. The mesh includes 167,000 elements, (550,000 dof) and over 13,000 contact segments. It required approximately half an hour of wall time to run, using 64 processors for the linear equation solving phases in NIKE3D.

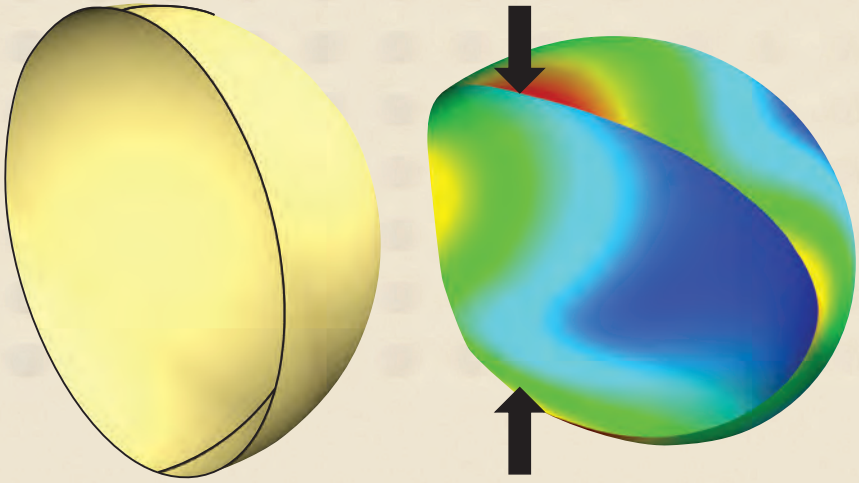

Figure 3. Bending of thin steel shell membrane. The radius is 10 in. and the thickness is 0.04 in.

the preferred contact method for our analysts. The classical contact algorithms are node-on-segment [Fig. 1(a)] whereas mortar contact is a segment-to-segment type contact algorithm [Fig. 1(b)]. The mortar contact method smoothes the contact results and thus provides more robust response. Unfortunately, the segment-to-segment approach is radically different and little of the existing node-on-segment code could be reused for its implementation.

The popularity of the node-on-segment approach was mainly due to its simplicity and it evolved to accommodate a number of different search algorithms and formulations such as local search, bucket sort, and automatic contact. The segment-to-segment approach is more complicated and some of NIKE3D's contact features still need to be implemented in that context.

The latest enhancement is the bucket sort for replacing the simple "brute force" search originally implemented. The old mortar sort algorithm used order N^2 operation (where N is the number of contact facets). The bucket sort, appropriately implemented, reduces to order N operations. The new bucket sort defines a 3-D grid based on a characteristic length. This grid is then populated with master and slave segments. Each cell in that grid is called a bucket, and candidate segment interactions need to be searched only between adjacent buckets.

Bucket sorts achieve optimal speed when all segments are equal size but can approach N^2 operation counts when segment sizes differ. To alleviate this problem, segments can be binned according to sizes and a multiple pass bucket sort approach used. The speed up can be dramatic.

Figure 2 shows an aft coupler joint from a composite material assembly. The contact search time using the old search algorithm required 2500 s whereas the new bucket sort required only 318 s.

The stress initialization feature was upgraded to accommodate the new HDF file format used by ParaDyn. This feature is useful for static initialization of models prior to assessing fast transient response. Whereas explicit dynamic relaxation is often used for such initialization, an implicit code such as NIKE3D can be faster. Figure 3 shows the bending of a thin shell; Fig. 4 displays wall clock times required to do static initialization as the mesh is refined. ParaDyn typically demonstrates near perfect scaling as the number of processors is increased for a fixed mesh size. However, here the problem geometry is fixed and the number of elements increases, requiring a smaller time step size. As the same total time interval must be simulated to dampen to a static response, the number of ParaDyn time steps to solution increases. NIKE3D's parallel direct solver cannot scale perfectly either, but maintains a performance edge across the range of problem size considered.

FY2010 Proposed Work

Our plans for FY2010 include 1) modularizing and upgrading data structures and improving shell routines; and 2) implementing an interior point method within a quasi-Newtonian framework for the solution of unilateral contact problems.

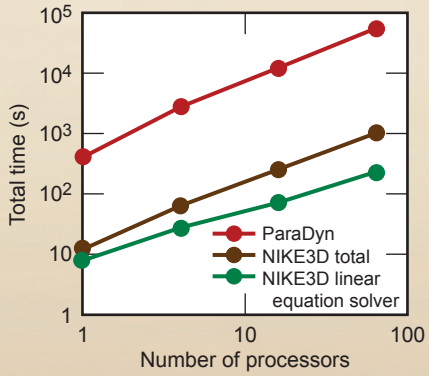

Figure 4. Scaling plot for stress initialization of a thin sphere. Here, the mesh is refined as the number of processors is increased. ParaDyn typically scales very well but does not in this type of benchmark since the time step shrinks with successive refinements. NIKE3D is not parallel but the direct linear solver is. This solver typically scales very well.

Electromagnetics Code Maintenance

Daniel A. White
(925) 422-9870
white37@llnl.gov

LLNL Engineering's EMSolve code is a 3-D, parallel, finite element code for solving Maxwell's equations. EMSolve has modules for electrostatics, magnetostatics, eigenvalues, eddy currents, and wave propagation. The code has been used to support NIF, the Weapons Program, and Global Security. In addition, EMSolve results have appeared in approximately 30 peer-reviewed publications. The purpose of this project is to enhance, verify, document, and maintain the EMSolve suite of computational electromagnetics codes.

Project Goals

The goal for FY2009 was to incorporate sensitivity analysis and uncertainty quantification into EMSolve in collaboration with Ohio State University. In finite element codes such as EMSolve, the geometry, material properties, and source terms are considered *input*, and field values (*e.g.*, electric field, magnetic field, and current density) are considered *output*. In virtually all engineering applications there is some uncertainty in input, and quantifying that effect upon output is referred to as uncertainty quantification. A key step in uncertainty quantification is sensitivity analysis, defined by computing the differential change in output due to a differential change in the input.

Relevance to LLNL Mission

EMSolve can perform electromagnetic analyses that cannot be undertaken with commercial codes. This allows better support for programs, and EMSolve's unique capability allows LLNL to be better positioned to assist other government agencies through work-for-others projects.

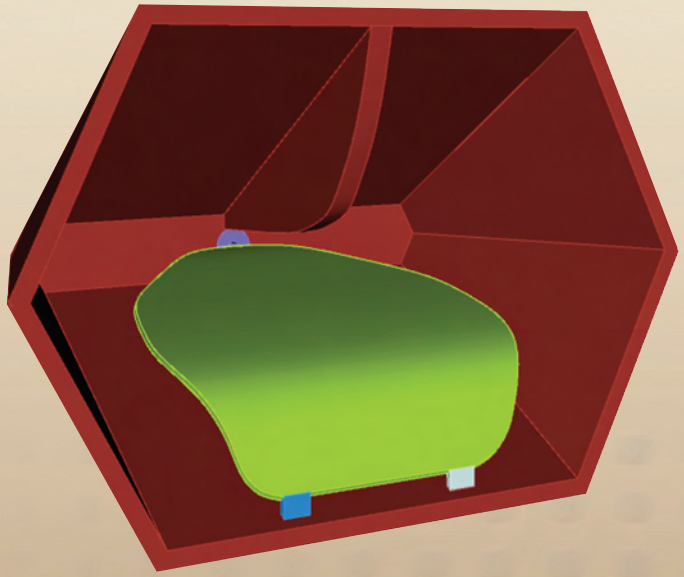

Figure 1. CAD model of an ultra-wideband antenna. This antenna is currently being used for several radar projects. The two small tabs are resistors, and the sensitivity of the radiated power with respect to these resistors can be determined using the Adjoint Method.

FY2009 Accomplishments and Results

We investigated several approaches for sensitivity analysis and determined that a good starting point is the Adjoint Method. For clarity of explanation we will write the frequency domain finite element representation of Maxwell's Equations as **Au = b**, where **b** is the source vector, **A** is the discretized Helmholtz Equation, and **u** is the solution vector. We have a set of parameters **p** = $\{p_1, p_2, \ldots, p_n\}$ that affect the solution vector **u**, and we have a response functional **R (p,u)** that is an engineering metric of interest, *e.g.*, total current or input impedance. Sensitivity analysis consists of computing

$$\nabla R = \left(\frac{dR}{dp_1}, \frac{dR}{dp_2}, \ldots, \frac{dR}{dp_N} \right)$$

$$\text{where } \frac{dR}{dp_i} = \frac{\partial R}{\partial p_i} + \frac{\partial R}{\partial u}\frac{\partial u}{\partial p_i}$$

We assume that the engineering metric of interest is linear; *i.e.*, **R = c u**. The sensitivity equation is then

$$\frac{dR}{dp_i} = c'u + cA^{-1}(b' - A'u)$$

where the prime denotes differentiation with respect to the parameter, **p**. The key step in the Adjoint Method is to introduce an adjoint variable, ψ, defined by the equation

$$A^H \Psi = c$$

The second term in the sensitivity equation becomes

$$cA^{-1}(b' - A'u) = \psi (b' - A'u),$$

the net effect being that to compute the sensitivity of **R** with respect to **N** parameters requires only two linear solves, one for **u** and one for ψ.

The Adjoint Method described above was implemented in the frequency domain module of EMSolve. For the time being the parameters **p** are restricted to be material properties, sensitivity with respect to geometry is significantly more complex and will be implemented next year.

As an example consider the ultra-wideband antenna illustrated in Fig. 1. The aperture is approximately 3.2 by 2.2 in. The two small tabs below the tongue are 100-Ω resistors. This antenna is designed to operate from 2 GHz to 5 GHz. We used the Adjoint Method to compute the sensitivity of the antenna-radiated power with respect to the conductivity and dielectric constant of the resistors.

The interesting sensitivity results are shown in Fig. 2. First, the sensitivity is low, meaning it is not necessary to fabricate precision resistors. While variability in radiated power between different antennas is experimentally observed, this sensitivity analysis shows that observed variability is not due to variation in resistors. Second, the sensitivity has the same sign for all frequencies, meaning the radiated power can be increased across the entire frequency band by reducing the value of the resistors. Third, the sensitivity with respect to the dielectric constant also has constant sign, thus adding a capacitor will increase the radiated power across the entire frequency band. This example shows how sensitivity analysis can be used both for assessing the effect of manufacturing variability and also for system design optimization.

Related References

Cacui, D., Sensitivity and Uncertainty Analysis, Volume 1, CRC Press, 2003.

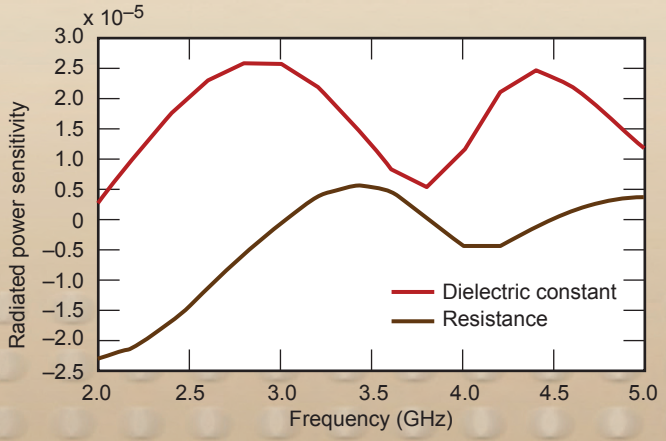

Figure 2. Sensitivity of radiated power with respect to resistance and capacitance of the two small tabs. This result can be used to optimize the antenna design and to determine acceptable manufacturing specifications.

High Efficiency, Zero Emission, Low Cost H_2-O_2-Ar Engine

Salvador M. Aceves
(925) 422-0864
aceves6@llnl.gov

While gasoline-hybrid vehicles reduce CO_2 emissions and petroleum use, the goal of complete elimination of automotive petroleum use and the resulting emissions will demand hydrogen-fueled vehicles. Fuel cells are thought necessary to power hydrogen vehicles due to their high efficiency (~50%). The current high cost of fuel cells is the greatest barrier to hydrogen vehicle commercialization.

We are investigating the feasibility of a hydrogen (H_2) spark-ignited internal combustion engine that promises the highest efficiency of any engine ever built. This engine can have the high efficiency and zero emissions of a fuel cell, enabling affordable and practical vehicles necessary for a successful transition to carbonless transportation. Our concept for hydrogen engines consists of mixing H_2 and oxygen (O_2) with argon (Ar) in the combustion chamber. Argon has a high specific heat ratio (γ = 1.67, compared to γ <1.4 for air). According to basic engine theory, this high value of γ can considerably improve engine efficiency. Theory predicts an ideal efficiency approaching 75% (Fig.1), and in practice we anticipate 50% once heat transfer and friction losses are included. Argon can be recycled in a closed loop (Fig. 2), so that there is no need for "refueling" Ar.

Fully realized, the H_2-O_2-Ar engine would represent a transformational

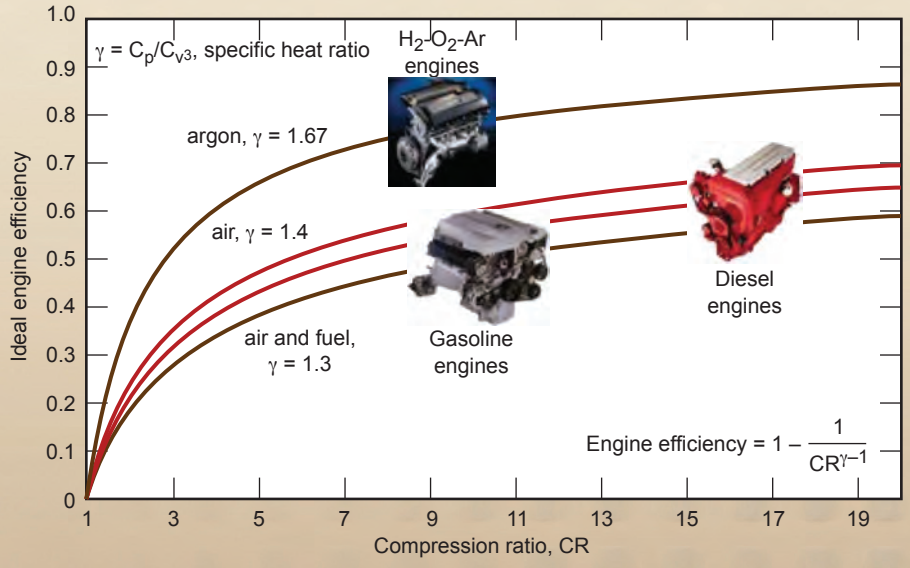

Figure 1. The efficiency of an Otto-cycle internal combustion engine. Ideal engine efficiency is dependent on the compression ratio and the specific heat ratio, γ, of the gases in the cylinder. Using Ar as a working fluid allows for significant gain in the thermodynamic efficiency of the cycle.

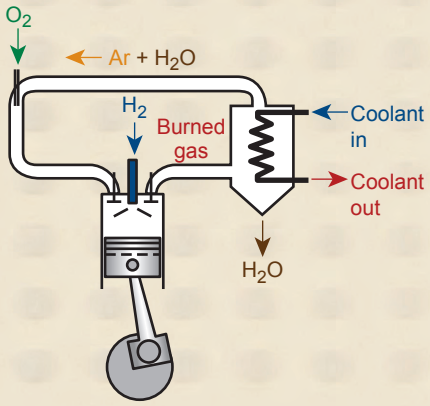

Figure 2. The H_2-O_2-Ar engine. The engine achieves high efficiency by operating with Ar in a closed loop, adding H_2 and O_2 for combustion, and condensing out combustion product water.

breakthrough in the use of H_2, delivering a vehicle power plant with similar performance to a fuel cell, but with significantly reduced cost. This innovation rethinks how an engine is operated by adapting current technology, does not need breakthroughs in materials technology to be successful, and is deployable in the near term. This engine concept has many advantages:

1. High efficiency: argon gas as the working fluid in an internal combustion engine has the most favorable thermodynamic characteristics.
2. Zero emissions: carbon and nitrogen are eliminated from the engine system, avoiding compounds that promote both global warming (CO_2) and local air pollution (CO, HC, NO_X).
3. Affordability: the engine has no significant cost premium since it can be made entirely from existing engine technology.
4. High power density: the closed loop allows the engine to be effectively supercharged with little parasitic losses.
5. Argon abundance: Ar is inexpensive and abundant and could readily meet the demand for a fleet of H_2-O_2-Ar powered vehicles using recirculating Ar.

Project Goals

Our work focuses on demonstrating the virtues of the H_2-O_2-Ar engine concept. Due to its unique combustion characteristics, hydrogen is the only practical fuel for this concept. Hydrogen fuel enables engine operation spanning the broadest possible range of compositions with O and Ar, and the easily condensed combustion product (water) makes operation at high pressures and attendant high power density possible. This fuel ratio flexibility also means an extensive space of compositions must be evaluated over the operational range needed for a practical engine.

Relevance to LLNL Mission

The goals of this project are aligned with LLNL's missions in energy and the environment.

FY2009 Accomplishments and Results

We have developed a science-based capability to identify appropriate regions of operation for a H_2-O_2-Ar engine. As compression with a high specific heat ratio leads to high pressure and temperature during the compression stroke, we developed and validated a detailed chemical kinetic mechanism for hydrogen combustion especially tuned for this previously unexplored thermodynamic space. This mechanism was then applied within a systems model of the engine that confirmed its potential for very high efficiency and low emissions for closed cycle operation. Ongoing work focuses on detailed fluid mechanics modeling of H_2-O_2-Ar engine combustion.

In a parallel task, we converted a variable compression ratio CFR engine to H_2-O_2-Ar operation (Fig. 3) and extensively tested the range of chemical compositions and compression ratios that may maximize efficiency. Preliminary efficiency results are limited by knock (fuel autoignition ahead of the spark-initiated flame). Knock avoidance calls for operation at higher speeds in overexpanded engines (asymmetric engine cycle with higher expansion ratio than compression ratio), and this is the direction of current investigation. In the longer term, high-pressure hydrogen direct injection during the compression stroke could prove a straightforward approach for eliminating engine knock.

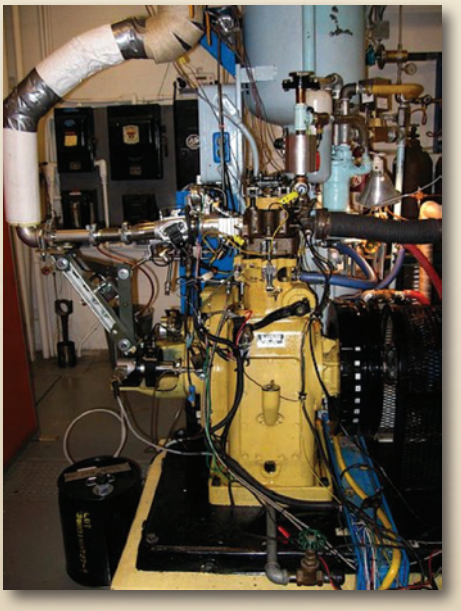

Figure 3. H_2-O_2-Ar operation. A flexible and robust single cylinder variable compression ratio engine is critical to optimizing the performance of the combustion system, particularly when operating an engine in a brand new regime like that of the H_2-O_2-Ar engine.

Micro/Nano-Devices & Structures

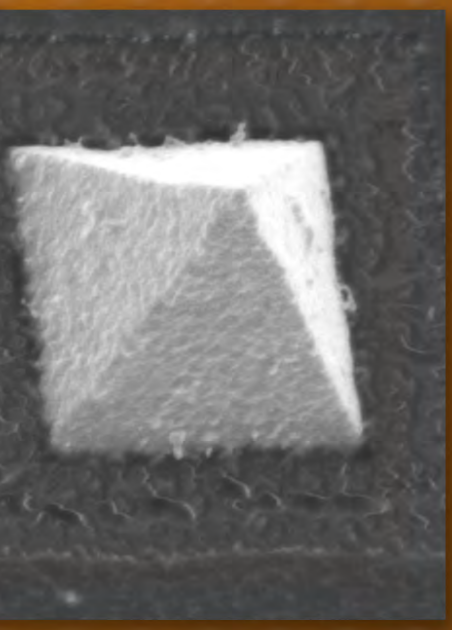

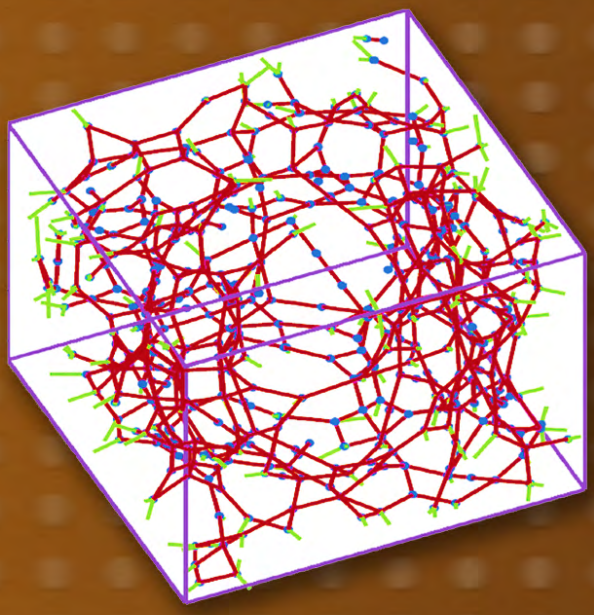

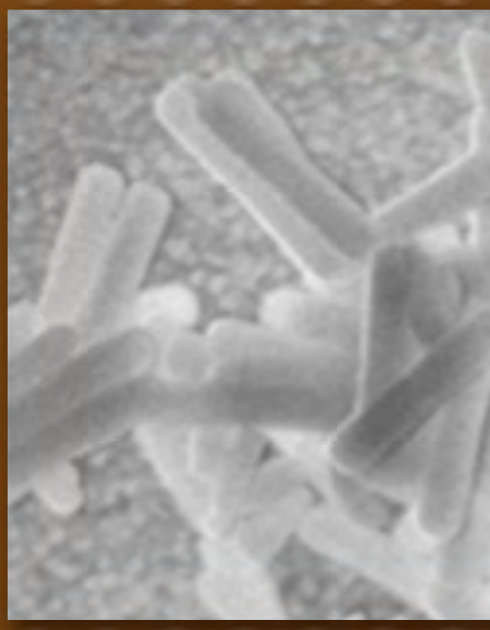

Hybridization, Regeneration, and Selective Release of DNA Microarrays

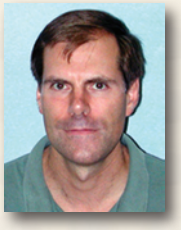

John M. Dzenitis
(925) 422-6695
dzenitis2@llnl.gov

DNA microarrays contain sequence-specific probes arrayed in distinct spots numbering from 10,000 to over 1,000,000, depending on the platform. This tremendous degree of multiplexing gives microarrays great potential for environmental background sampling, broad-spectrum clinical monitoring, and continuous biological threat detection. In practice, their use in these applications is not common due to limited information content, long processing times, and high cost. This work seeks to characterize the phenomena of microarray hybridization, regeneration, and selective release that will allow these limitations to be addressed. This will revolutionize the ways that microarrays can be used for LLNL's Global Security missions.

One study area is selective release. Microarrays easily generate hybridization patterns and signatures, but there still is an unmet need for methodologies enabling rapid and selective analysis of these patterns and signatures. Detailed analysis of individual spots by subsequent sequencing could potentially yield significant information for rapidly mutating and emerging (or deliberately engineered) pathogens. In the selective release work, optical energy deposition with coherent light is being explored to quickly provide the thermal energy to single spots to release hybridized DNA.

The second study area involves hybridization kinetics and mass-transfer effects. The standard hybridization protocol uses an overnight incubation to achieve the best possible signal for any sample type, as well as for convenience in manual processing. There is potential to significantly shorten this time based on better understanding and control of the rate-limiting processes and knowledge of the progress of the hybridization. In the hybridization work, a custom microarray flow cell will be used to manipulate the chemical and thermal environment of the array and image the changes over time during hybridization.

A related study area is regeneration. Microarrays cost hundreds of dollars and can typically be used only once, or at most a few times, due to degradation in signal with reuse. Balancing the thoroughness of the regeneration process against the stability of the microarray and quantitative signal requirements could enable new microarray applications.

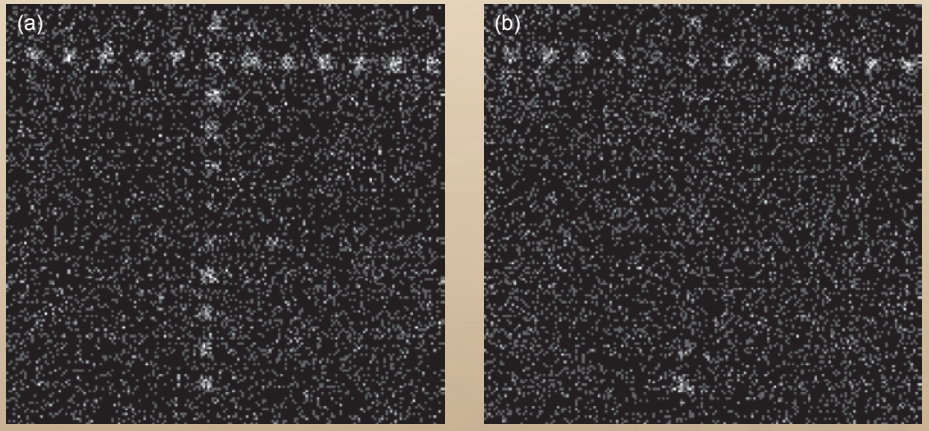

Figure 1. Demonstration of the effect of IR laser energy deposition on a DNA microarray at approximately 100-µm resolution from the spot field, (a) before and (b) after deposition.

Project Goals

The goals of the selective release work are to characterize the phenomena involved in high-resolution energy deposition with an IR laser and to demonstrate selective release of DNA from a microarray. This includes assessing the effects of wavelength, absorption, spot size, materials, pulse energy, and fluid flow.

The goal of the hybridization work is to quantify the rate-limiting processes in microarray hybridization and to

demonstrate improvement in hybridization time by controlling the process.

The goals of the regeneration work are to determine the cause of microarray degradation in regeneration and to reduce degradation.

Relevance to LLNL Mission

LLNL has ongoing efforts in detection methods against biological terrorism. The next stage of molecular diagnostics for biological threats is to look much more broadly for emerging threat bio-signatures, such as virulence elements or natural and engineered mutations. This capability is targeted against new natural pandemics and engineered biological warfare agents, while still detecting the full set of known bio-threat agents, to enable prompt countermeasures.

FY2009 Accomplishments and Results

Most of the effort this fiscal year was focused on selective release. We extended the capability of the DNA Release and Capture Laser (DRACULA) system with an alignment method and positioning controller to address microarray spots. With this system, we demonstrated energy deposition to microarrays by showing an effect on spot fluorescence near the diffraction limit, at approximately 100-µm resolution (Fig. 1). We developed a 3-D computational fluid dynamics (CFD) model to characterize the penetration heating profile of the current 10.6-µm CO_2 laser, and used the code to assess the energy deposition that would result from a new 1.47-µm diode laser (Fig. 2). This confirmed that the shorter-wavelength laser would provide better heating penetration,

Figure 2. Results from a numerical simulation of the temperature distribution resulting from (a) the 10.6-µm laser and (b) the 1.47-µm laser.

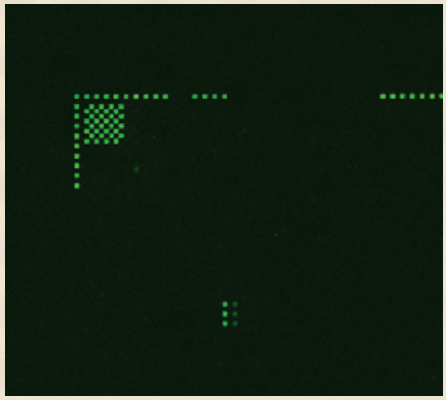

Figure 3. Detail image (approximately one two-hundredth of a microarray scan) showing 15-µm fiducial spots in an initial experiment of integrated hybridization and scanning using the microarray flow cell.

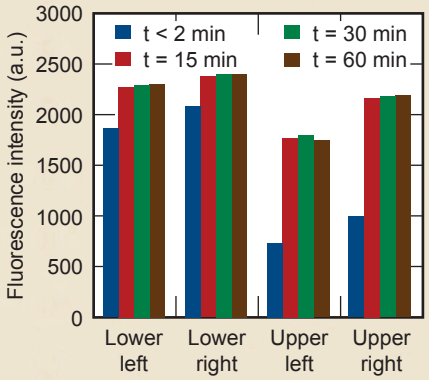

Figure 4. Average fluorescence values over time for the four fiducial corners during an initial experiment of integrated hybridization and scanning. Most of the signal was achieved early in the incubation.

which may be required for well-controlled selective release. We also designed and fabricated custom microarrays with SARS and Rhinovirus probes for use in selective release testing of biological samples.

In the first steps of the hybridization work, we used the microarray flow cell to perform hybridizations first off-scanner and then integrated with the scanner (Fig. 3). We developed an analysis method to quantify the hybridization level for this system, and proved that the experimental apparatus will be able to provide kinetic data by tracking hybridization level over time on control spots (Fig. 4).

Related References

1. Chan, V., D. J. Graves, and S. E. McKenzie, "The Biophysics of DNA Hybridization with Immobilized Oligonucleotide Probes," *Biophys. J.*, **69**, pp. 2243–2255, 1995.

2. Jaing, C., S. Gardner, K. McLoughlin, N. Mulakken, M. Alegria-Hartman, P. Banda, P. Williams, P. Gu, M. Wagner, C. Manohar, and T. Slezak, "A Functional Gene Array for Detection of Bacterial Virulence Elements," *PLoS ONE*, **3**, 5, e2163, 2008.

3. Singh-Gasson, S., R. D. Green, Y. J. Yue, C. Nelson, F. Blattner, M. R. Sussman, and F. Cerrina, "Maskless Fabrication of Light-Directed Oligonucleotide Microarrays Using a Digital Micromirror Array," *Nat. Biotech.*, **17**, pp. 974–978, 1999.

4. Wang, D., A. Urisman, Y. Liu, M. Springer, *et al.*, "Viral Discovery and Sequence Recovery Using DNA Microarrays," *PLoS Bio.*, **1**, pp. 257–260, 2003.

5. Wang, Z., L. T. Daum, G. J. Vora, D. Metzgar, E. A. Walter, L. C. Canas, A. P. Malanoski, B. Lin, and D. A. Stenger, "Identifying Influenza Viruses with Resequencing Microarrays," *Emerging Infectious Diseases*, **12**, 4, pp. 638–646, 2008.

FY2010 Proposed Work

For selective release, the key milestone will be release and capture of undamaged SARS target DNA selectively over Rhinovirus target DNA. For the hybridization effort, we will design an array for hybridization rate tests investigating effects such as probe length, target length, and sequence mismatch, and will quantify those effects along with concentration, flow rate, and temperature. In regeneration, we plan to fabricate sets of arrays with custom coupling and probe chemistry to assess their stability to different regeneration processes in bulk and in the microarray flow cell. Combined, these efforts will expand the applicability of microarrays to LLNL's Global Security missions.

A Mesoscale Approach to Characterize Material Properties of Polymeric Media

Todd H. Weisgraber
(925) 423-6349
weisgraber2@llnl.gov

Over time, changes in the network microstructure of filled or reinforced elastomers due to chemical bond scission and crosslinking can alter the physical properties of these materials. In particular, chemical aging can strongly affect the elastic properties of the network through modifications to the network as well as changes in the interactions between the polymer and filler particles. Furthermore, changes in the mechanical properties can depend on the strain history. For example, an elastomer that undergoes additional crosslinking in a state of strain can acquire a permanent set or deformation when the stress is removed. The ability to accurately predict the mechanical behavior of these materials through robust models to assess lifetime performance in different environments is essential. We have adopted a mesoscale network model that retains information about the microstructure and is not limited by some of the assumptions found in constitutive descriptions.

Project Goals

In our second year, our goals were to improve the understanding of the robustness of the network model by 1) evaluating the model's applicability to materials of programmatic interest (filled elastomers and foams); 2) adding the capability to manipulate the microstructure in a predetermined manner; and 3) examining the relationship between microstructure, material response, and aging parameters.

Relevance to LLNL Mission

This effort has enabled LLNL to play a key role in the multiscale modeling of mission-critical materials through the linkage of scales. Specifically, we examined the relationship between a coarse-grained representation of the microstructure and the mechanical properties and lifetime performance of these materials. A variety of ongoing programs will benefit from these capabilities. A specific early adopter of this technology will be the Enhanced Surveillance Campaign (ESC).

FY2009 Accomplishments and Results

The mesoscopic network model consists of a set of nodes with selected node pairs linked by a single "bond" that represents a crosslink in the network. Initially the connectivity is arranged on a simple cubic lattice with periodic boundary conditions (Fig. 1). The bond interactions are described by a FENE spring potential and the standard Lennard-Jones potential. Bonds within the initial cubic lattice are randomly selected and deleted from the lattice to obtain the desired crosslink density. The ensemble of bonded nodes is then relaxed via energy minimization to obtain the initial structure.

The material we focused on in the first year had a fairly linear stress response over moderate strains so it was relatively straightforward to parameterize the model to capture this behavior. Another filled silicone elastomer, TR-55, exhibited a similar linear response over small and large strains while having a non-linear transition for intermediate

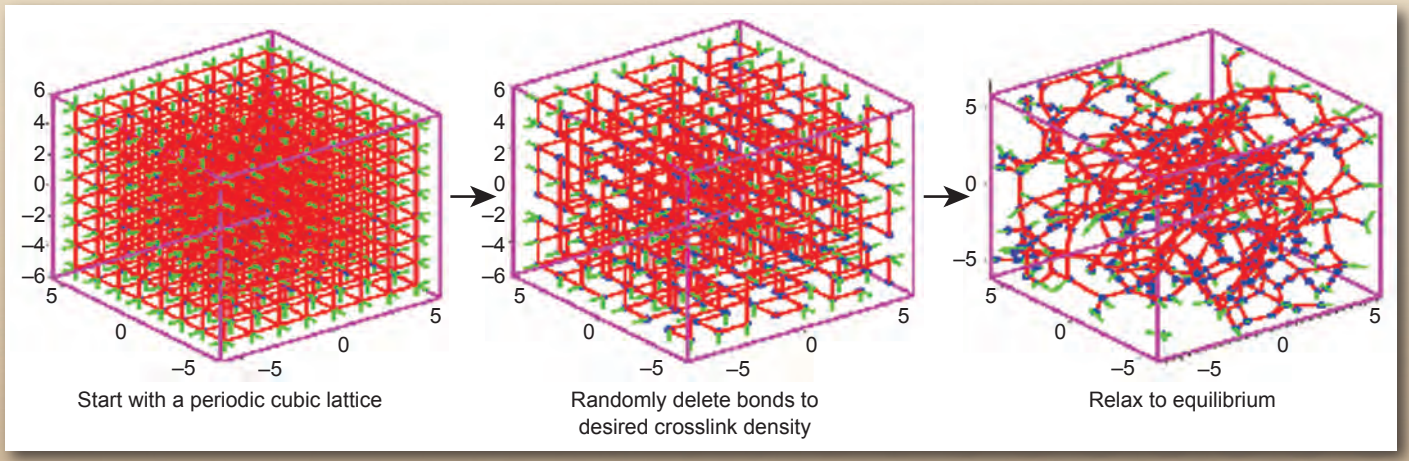

Figure 1. Initializing the microstructure in the mesoscopic model.

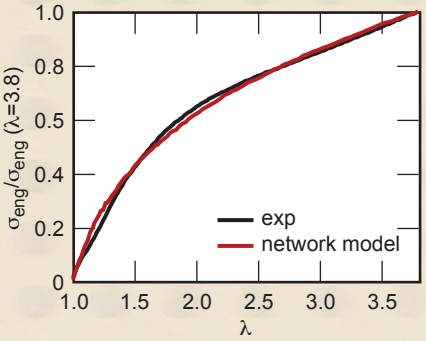

Figure 2. Normalized stress response of a sample of TR-55, a filled elastomer (black curve), compared with the mesoscopic model representation of this material (red curve).

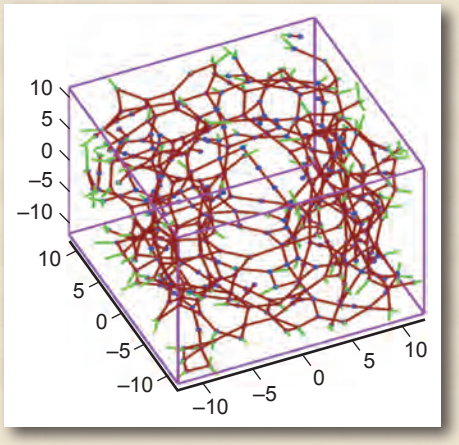

Figure 3. Mesoscopic model microstructure of a foam material. Blue circles represent nodes; red lines are bonds; and green lines denote periodic bonds that intersect the domain boundary. Note the center of the domain is devoid of bonds.

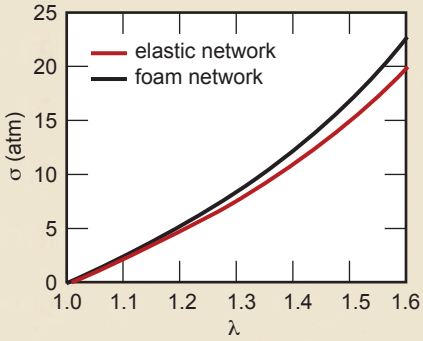

Figure 4. Comparison of the stress response of a representative elastomer network (no voids) and the model foam network depicted in Fig. 3.

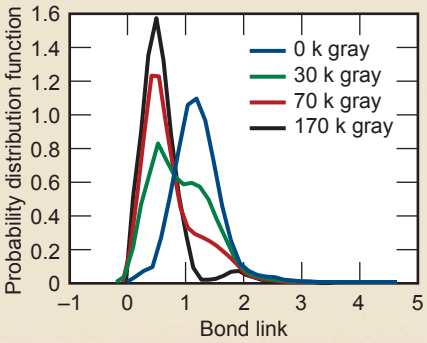

Figure 5. Distribution functions of the polymer length between crosslinks as a function of exposure to ionizing radiation or artificial aging.

strains. By varying the appropriate bond parameters, the network model produced a stress curve very similar to the experimental data from a sample of this material. Figure 2 shows the normalized stress results from this comparison. In terms of accuracy, the predicted stress curve from the model was comparable to some of the more sophisticated constitutive equations, which contain more free parameters.

Elastomeric foams are also of interest, so we enhanced the capability of the model to include void regions to approximate microstructures for these materials. Figure 3 shows the model foam structure after creating a void in the central region and equilibrating. Using this result we were able to address the relationship between the network topology and the elastic properties of these materials. We compared the stress response of an elastomeric structure without any voids and the new foam structure with a single void. The crosslink densities of both models were set equal to avoid inconsistencies in the shear modulus. The results in Fig. 4 indicate that the stress of the foam model is consistently larger than the elastomer stress.

Finally, we examined the changes in elastomer microstructure resulting from exposure to ionizing irradiation. In this aging process chain scission occurs but crosslinking dominates and increases with dosage. The network modifications can be simulated with the mesoscopic model by adding and removing bonds. One method of monitoring the microstructural changes is the distribution of bond or chain lengths between crosslinks. These distributions are plotted in Fig. 5 for several dosages. The shift toward lower chain lengths and the gradual narrowing and increase of the peak is consistent with an increase in net crosslinking. These predictions qualitatively agree with quantum NMR measurements of these aged materials.

Related References

1. Andrews, R. D., A. V. Tobolsky, and E. E. Hanson, "The Theory of Permanent Set at Elevated Temperatures in Natural and Synthetic Rubber," *J. Appl. Phys. Chem.*, **17**, pp. 352-361, 1946.

2. Rottach, D. R., J. G. Curro, G. S. Grest, and A. P. Thompson, "Effect of Strain History on Stress and Permanent Set in Cross-Linking Networks: A Molecular Dynamics Study," *Macromolecules*, **37**, 14, pp. 5468-5473, 2004.

3. Kremer, K., and G. S. Grest, "Dynamics of Entangled Linear Polymer Melts - A Molecular-Dynamics Simulation," *Journal of Chemical Physics*, **92**, 8, pp. 5057-5086, 1990.

4. Grimson, M. J., "Structure and Elasticity of Model Gel Networks," *Molecular Physics*, **74**, 5, pp. 1097-1114, 1991.

5. Weisgraber, T. H., R. H Gee, A. Maiti, S. Chinn, and R. S. Maxwell, "A Mesoscopic Network Model for Permanent Set in Cross-linked Elastomers," *J. Polymer*, **10**, p. 1016, 2009.

Cadmium-Zinc-Telluride Sandwich Detectors for Gamma Radiation

Adam M. Conway
(925) 422-2412
conway8@llnl.gov

Detectors to sense nuclear and radioactive weapons concealed in transit through borders, airports, and seaports are crucial for the international struggle against terrorism and proliferation of weapons of mass destruction. Currently, germanium detectors offer the best performance in detecting gamma rays; however, they must be operated at cryogenic temperatures. A room-temperature detector is greatly preferred because of cost and ease of use, but the only available alternative is based on cadmium-zinc-telluride (CZT) technology, which offers inferior performance. Here we propose a pathway for CZT gamma detectors to achieve the desired energy resolution of less than 1%. We will use a multilayered structure as shown schematically in Fig. 1, to allow signal collection while simultaneously rejecting noise, which arises primarily due to leakage current.

Figure 1. Schematic diagram of a-Si:H/CZT detector layer structure.

Project Goals

With this project, we expect to demonstrate a pathway toward a gamma detector with better than 1% energy resolution that will operate at room temperature. To achieve this goal, we will design a novel structure using bandgap engineering concepts that will result in a 90% reduction in leakage current relative to a resistive device. We also will provide leadership to the detector community by providing a technical roadmap for how to demonstrate a 0.5% energy resolution within five years.

Relevance to LLNL Mission

The solution to the radiation-detector materials problem is expected to have significant impact on efforts to develop detectors that are compact, efficient, inexpensive, and operate at ambient temperature for the detection of special nuclear materials as well as radiological dispersal devices. The multidisciplinary nature of this work and the relevance to national and homeland security align well with LLNL capabilities and missions.

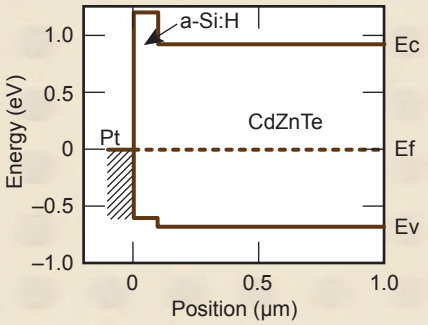

Figure 2. Simulated energy band diagram of a-Si:H/CZT layered structure.

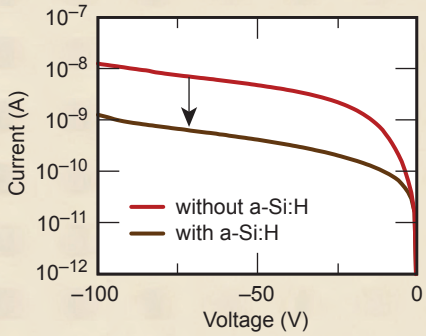

Figure 3. Comparison of current vs. voltage characteristics with (brown) and without (red) a-Si:H contacts.

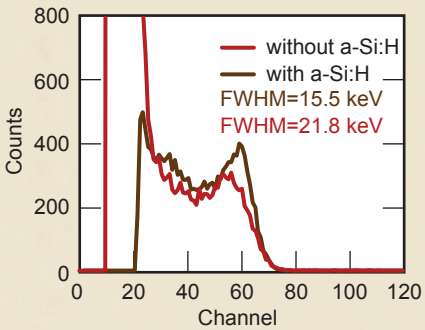

Figure 4. ^{241}Am gamma spectra for CZT detectors with and without a-Si:H blocking contact.

FY2009 Accomplishments and Results

In FY2009, we have:

1. benchmarked our models with experimentally gathered data from FY2008 and refined our models to account for discrepancy;
2. designed and fabricated structures with amorphous layers on CZT and carried out both electrical and radiation characterization, which show reduced dark current and improved breakdown voltage over structures without amorphous layers (Fig. 2);
3. demonstrated an effective resistivity of greater than 10^{11} ohm-cm (> 200 V) in material that is considered too conductive for typical CZT gamma detectors with resistivity of 10^{9} ohm-cm; and
4. used these structures to characterize the interface and energy barrier between the amorphous material and single-crystalline CZT.

Related References

1. Conway, A. M., B. W. Sturm, L. F. Voss, P. R. Beck, R. T. Graff, R. J. Nikolic, A. J. Nelson and S. A. Payne, "Amorphous Semiconductor Blocking Contacts on CdZnTe Gamma Detectors," *International Semiconductor Device Research Symposium*, December 2009.

2. Voss, L. F., A. M. Conway, B. W. Sturm, R. T. Graff, R. J. Nikolic, A. J. Nelson, and S. A. Payne, "Amorphous Semiconductor Blocking Contacts on CdTe Gamma Detectors" *IEEE Nuclear Science Symposium*, October 2009.

3. Nelson, A. J., A. M. Conway, C. E. Reinhardt, J. J. Ferreira, R. J. Nikolic, and S. A. Payne, "X-Ray Photoemission Analysis of CdZnTe Surfaces for Improved Radiation Detectors," *Materials Lett.* **63**, 180, 2009.

FY2010 Proposed Work

In FY2010, we propose to 1) use x-ray photoelectron spectroscopy to characterize surface Fermi level pinning and add interface physics to our heterojunction detector model; 2) compare current vs. voltage vs. temperature measurements with capacitance vs. voltage measurements for characterization of Schottky barrier height and energy band offsets in amorphous CZT heterojunctions; 3) fabricate amorphous layer CZT heterojunction detectors that have an effective resistivity of greater than 10^{12} ohm-cm in material that is too conductive for typical CZT gamma detectors with resistivity of 10^{9} ohm-cm (Fig. 3); and 4) demonstrate a proof-of-principle detector with improved energy resolution (Fig. 4).

Study of Transport Behavior and Conversion Efficiency in Pillar Structured Neutron Devices

Rebecca J. Nikolić
(925) 423-7389
nikolic1@llnl.gov

A radiation detection device that can be easily fielded and offers high detection efficiency is vital to national security efforts. In this project, we will demonstrate technology that could lead to a device with over 70% thermal neutron detection efficiency. By applying microtechnology methods to neutron detection, we expect to make revolutionary improvements in device efficiency and field usability. We will take advantage of recent advancements in material science, charged carrier transport, and neutron-to-alpha conversion dynamics to fabricate semiconductor pillars in a 3-D matrix in which the neutron-to-alpha conversion material has adequate density to capture the full neutron flux.

Project Goals

With this project, we intend to develop and demonstrate a proof-of-principle device, and we will devise a roadmap for scaling the device to optimal efficiency. This is significant because current technology suffers from poor efficiency and adaptability to field use, high voltage, sensitivity to microphonics, a large device footprint, and high pressure, resulting in significant complications in air transport and deployments. The advances we propose in micro- and nanofabrication methods are applicable to many other fields, including biochemical detection, communications, and computations.

Relevance to LLNL Mission

Our project supports the Laboratory's national security mission by advancing technology for detection of special nuclear materials and radiological dispersal devices. If our demonstration device meets the requirements for high efficiency and demonstrates suitability for field use, it will pave the way to manufacturing field-ready devices in partnership with an industrial collaborator.

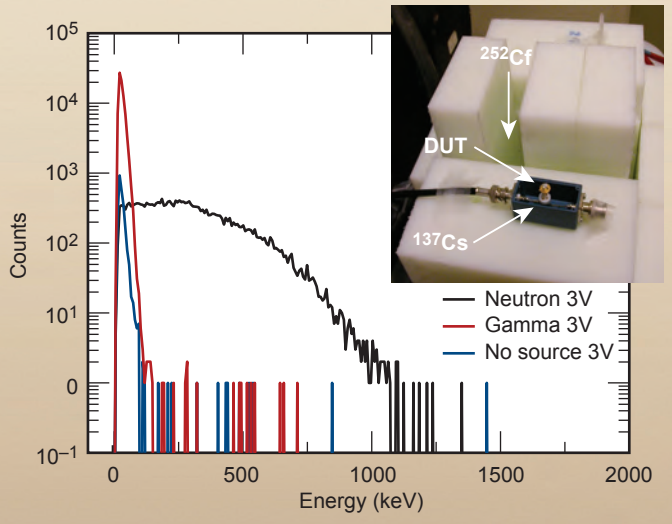

Figure 1. Neutron efficiency for LLNL's 3-D Pillar Structured Thermal Neutron Detector, currently at 20% thermal neutron detector efficiency, at 3 V, and 10^5 neutron to gamma discrimination. The inset shows the test configuration for the device under test (DUT). Both Cf and Cs are present for testing of both neutrons and gammas.

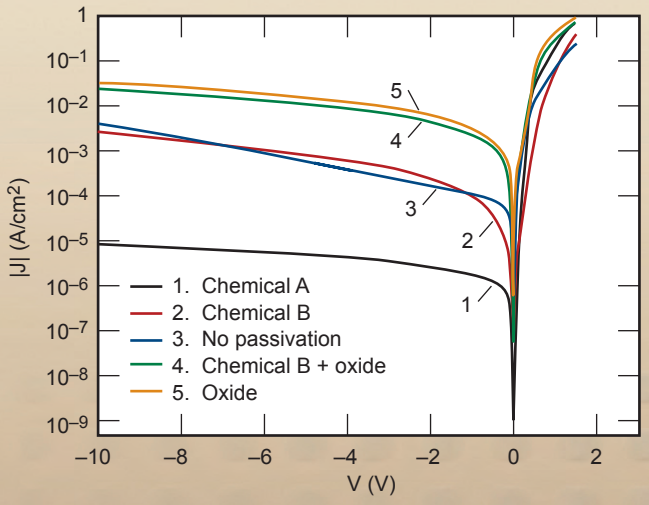

Figure 2. Current-voltage characteristics of Si pillar diodes with various passivation methods. An ideal diode would show very low current for negative voltages. Treatment with Chemical A produces diodes that come the closest to ideal in this case.

FY2009 Accomplishments and Results

Our primary milestones for FY2009 that came to full completion included:

1. Fabrication and characterization of 26-μm tall pillar detector with a 20% thermal neutron detection efficiency, 3-V reverse bias and a neutron to gamma discrimination of 10^5 (Fig. 1).
2. Reduction in pillar sidewall leakage current by understanding the relationship between chemical sidewall treatments and the electron-hole pair recombination lifetime. Decreased recombination rates (longer minority-carrier lifetimes) lead to less leakage current and to improved device performance (See table and Figs. 2 and 3).
3. We continued to publish material in both conference and journal papers.

In summary, we have designed a high efficiency thermal neutron detector by understanding the transport dynamics of neutrons, their interaction by-products and ultimately electron-hole pairs. By optimizing our 3-D detector structure we have defined a pathway to achieve a thermal neutron detection efficiency greater than 50% (Fig. 4).

Related References

1. Voss, L. F., C. E. Reinhardt, R. T. Graff, N. Deo, C. L. Cheung, A. M. Conway, R. J. Nikolic, "ECS Etching of ^{10}Boron for Thermal Neutron Detectors," *215th Meeting of the ECS*, May 2009.
2. Conway, A. M., L. F. Voss, C. E. Reinhardt, R. T. Graff, T. F. Wang, R. J. Nikolic, N. Deo, and C. L. Cheung, "Si Based Pillar Structured Thermal Neutron Detectors," *IEEE Nuclear Science Symposium*, October 2009.
3. Conway, A. M., T. F. Wang, N. Deo, and C. L. Cheung, "Numerical Simulations of Pillar Structured Solid State Thermal Neutron Detector Efficiency and Gamma Discrimination," *IEEE Transactions on Nuclear Science (TNS)*, October 2009.
4. Voss, L. F., C. E. Reinhardt, R. T. Graff, A. M. Conway, R. J. Nikolic, N. Deo, C. L. Cheung, "Comparison of CF_4 and SF_6 Plasmas for ECR Etching of Isotopically Enriched ^{10}boron Films," *Nuclear Instruments and Methods in Physics Research A*, **606**, pp. 821–823, 2009.
5. Nikolic, R. J., A. M. Conway, C. E. Reinhardt, R. T. Graff and T. F. Wang, N. Deo and C. L. Cheung, "Pillar Structured Thermal Neutron Detectors," *International Conference on Solid State and Integrated Circuit Technology (ICSICT)*, Beijing, China, October 20–23, 2008.

Passivation methods applied to Si pillars.

Passivation method	Preparation
Chemical A	1. RCA II, 80 °C, 10 min 2. HF (1%) 120 s 3. H_2SO_4:H_2O_2, 1:1, 120 °C, 10 min 4. HF (1%) 180 s
Chemical B	HNO_3:H_2:NH_4F, 126 ml: 60 ml: 5 ml, 1 min
Thermal oxidation	Dry O_2, 1150 °C, 40 min

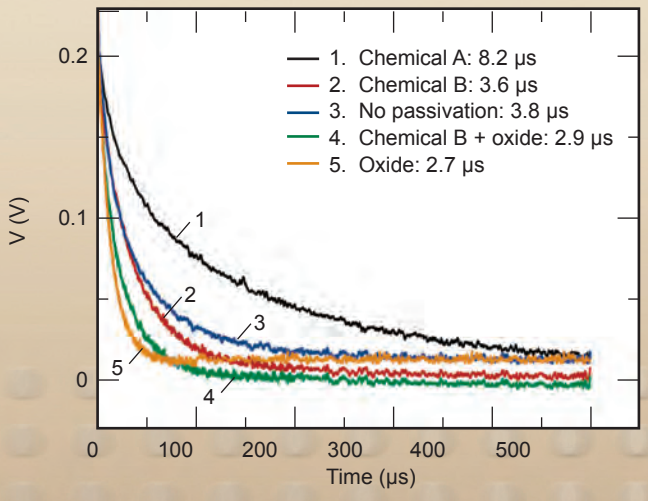

Figure 3. Open-circuit voltage decay waveforms of Si pillar diodes with various passivation methods. The extracted minority carrier lifetimes are listed. Longer lifetimes mean better performance of the diode.

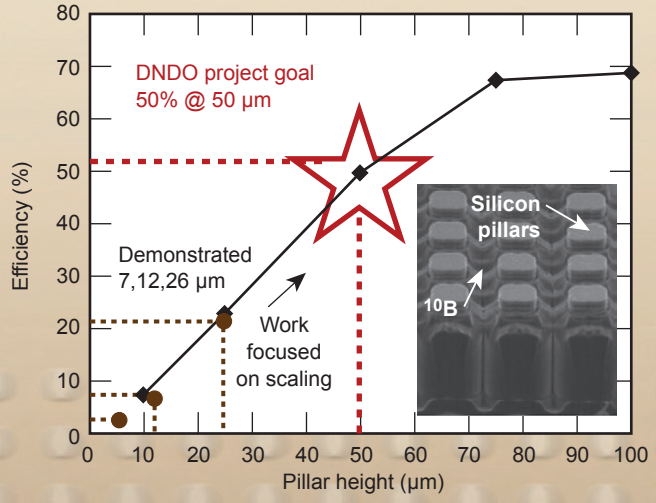

Figure 4. Roadmap of detector efficiency.

Enabling Transparent Ceramics Optics with Nanostructured 3-D Materials

Klint A. Rose
(925) 423-1926
rose38@llnl.gov

We are working on a novel nanomanufacturing technique, using the electrophoretic deposition (EPD) process to create transparent ceramic optics with unique properties based on tailored nanostructures. The EPD process uses electric fields to deposit charged nanoparticles from a solution onto a substrate.

We are expanding current EPD capabilities to enable controlled deposition in 3-D by automating the injection of nanoparticle suspensions into the deposition chamber and dynamically modifying the electrode pattern on the deposition substrate. We can also use the electric field to control the orientation of nonspherical particles during deposition to orient grain structures prior to sintering.

To enable this new functionality, we are 1) synthesizing ceramic nanoparticles as our precursor material; 2) implementing new instrumentation for the benchtop deposition experiments (Fig. 1); and 3) creating modeling capabilities to predict deposition kinetics and deposited structures based on the particle, solution, and system properties.

To guide our efforts, we have identified transparent ceramic optics as a major area in which nanostructured, functionally graded materials can have a significant impact. Laser physicists and optical system engineers are currently hindered by the small subset of materials available. The only crystalline materials open to them are those that can be grown as single crystals and isotropic

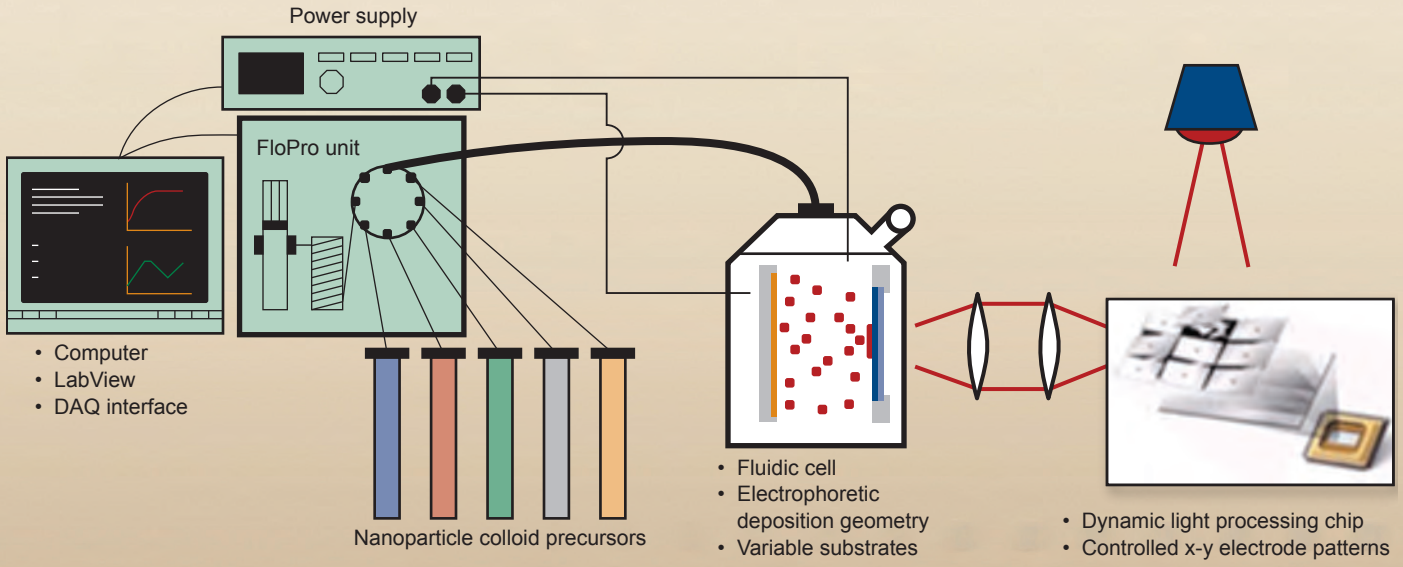

Figure 1. Schematic of electrophoretic deposition system. A FloPro unit pumps nanoparticle solutions into the deposition cell, where the computer controlled power supply provides either constant voltage or constant current between the two electrodes. A dynamic light processing (DLP) chip projects the desired deposition pattern from the computer onto one of the electrodes.

cubic materials that can be formed into transparent ceramics. By depositing nanorods of a noncubic material in the same orientation, the resulting green-body can theoretically be sintered to a transparent ceramic.

Additionally, current optics configurations are material- and process-limited to uniform composition profiles across optical components and laser gain media. To date, only coarse step function composition changes have been produced in the most advanced transparent ceramic optics. Our EPD platform will enable us to create new transparent ceramic optics with doping profiles tailored in three dimensions.

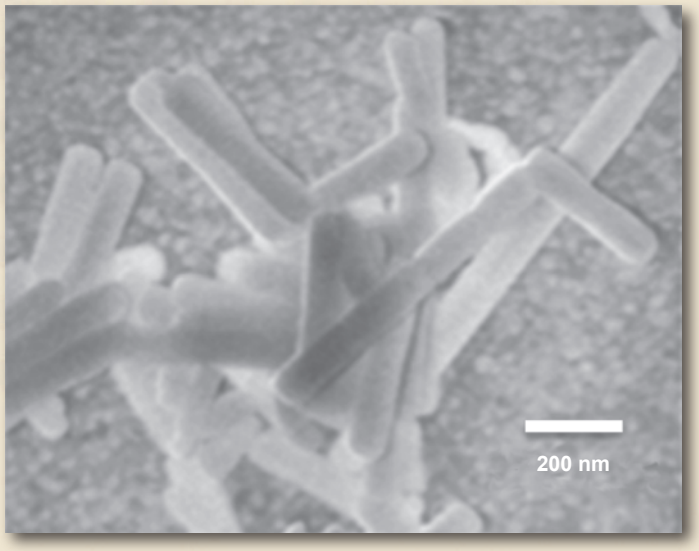

Figure 2. Fluorapatite nanowires synthesized at LLNL. The nanowires are approximately 100 nm in diameter and 500 nm in length.

Project Goals

The goals of this project are to demonstrate: 1) the fabrication of functionally graded materials with composition profiles tailored in 3-D while maintaining desired bulk properties; 2) the use of the EPD deposition field to simultaneously align nanorod particles of precursor material as they are deposited; and 3) the fabrication of composite structures with controlled material composition and create smooth or sharp material transitions along the z-axis of a composite structure.

Relevance to LLNL Mission

The project is intended to establish LLNL leadership in bottom-up nanofabrication of functionally graded materials. Our dynamic electrophoretic deposition system will position us to deliver the next generation of nanomanufacturing capabilities for projects throughout the Laboratory. Using these capabilities, we are working to produce a number of novel materials and structures. These structures will both illustrate the capabilities of the new process and demonstrate materials and structures of relevance to LLNL missions and programs. The main demonstrations for this project align with current and future needs in NIF as well as the LIFE and ALOSA thrust areas. These are: 1) to create transparent ceramic optics with doping profiles tailored in 3-D for new high-powered lasers (relevant to NIF and LIFE); and 2) to deposit aligned nanoparticles of noncubic ceramics to create a new family of transparent ceramics (relevant to NIF, LIFE, and ALOSA).

FY2009 Accomplishments and Results

Accomplishments and results in the first year include the following: 1) fabrication and testing of a new deposition chamber that enables automated injection and removal of particle suspensions and automated control of the electric field for deposition; 2) synthesis of fluorapatite and hydroxyapatite nanowires (Fig 2); 3) initiation of set-up of our dynamic electrode system with a high luminosity computer-controlled light source; and 4) integration of particle–particle interactions into the Stokesian dynamics model, which already included electrophoretic, dielectrophoretic, hydrodynamic, and Brownian motion effects.

FY2010 Proposed Work

In FY2010 we will 1) implement z-axis control and demonstrate a transparent sintered part with a depth-wise composition gradient; 2) demonstrate combined orientation and deposition control and fabricate transparent optic from noncubic material; 3) implement fixed-mask x-y control and demonstrate a transparent sintered part with a planar composition gradient; and 4) begin testing of dynamic x-y control.

High-Resolution Projection Micro-Stereolithography (PμSL) for Advanced Target Fabrication

Christopher M. Spadaccini
(925) 423-3185
spadaccini2@llnl.gov

This project advances the state of the art in 3-D target fabrication by using Projection Micro-Stereolithography (PμSL), first developed at the University of California, Los Angeles (UCLA) and the University of Illinois, Urbana-Champaign (UIUC). PμSL is a low-cost, high-throughput, microscale, stereolithography technique that uses a Digital Micromirror Device (DMD™ Texas Instruments) or a Liquid Crystal on Silicon (LCoS) chip as a dynamically reconfigurable digital photomask.

PμSL is capable of fabricating complex 3-D microstructures in a bottom-up, layer-by-layer fashion. A CAD model is first sliced into a series of closely spaced horizontal planes. These 2-D slices are digitized in the form of a bitmap image and transmitted to the LCoS. A UV LED illuminates the LCoS, which acts as a dynamically reconfigurable photomask and transmits the image through a reduction lens into a bath of photosensitive resin. The resin that is exposed to the UV light is then cured and anchored to a platform and z-axis motion stage. The stage is lowered a small increment and the next 2-D slice is projected into the resin and cured on top of the previously exposed structure.

Figure 1 shows a schematic of this process. This layered fabrication continues until the 3-D part is complete.

The process has been shown to have the capability to rapidly generate complex 3-D geometries. Applying this concept to target fabrication problems and advancing PμSL capability with respect to these issues constitutes the primary focus of the research. PμSL performance such as resolution, materials, geometries, and substrates, will be greatly improved by the following research directions:

1. Incorporation of a far-field superlens (FSL) to enhance resolution to the tens of nanometer-scale (well below the diffraction limit of UV light) enabling the first ever 3-D, nanoscale, fabrication system.
2. Incorporation of multiple DMD or LCoS assemblies to generate fully 3-D digital holograms enabling rapid throughput nanoscale features.
3. Use of laminar flow microfluidic systems to more optimally deliver and distribute photosensitive resins enabling fabrication with multiple materials.
4. Creation of a coupled optical-chemical-fluidic model resulting in an empirically validated design tool.

Project Goals

Our goals for FY2009 included:

1. Use of the new LLNL PμSL system to rapidly fabricate 3-D components.
2. Fabrication and integration of a superlens to demonstrate the capability for improved resolution; integration with PμSL.
3. Validation of the baseline coupled optical-chemical model.
4. Inclusion of fluid motion in the coupled model to study the impact of moving components in the liquid resin bath.
5. Initial demonstration of microfluidics with PμSL to demonstrate the capability to fabricate with multiple materials.

Relevance to LLNL Mission

Target fabrication for the National Ignition Facility (NIF) and other stockpile stewardship physics experiments

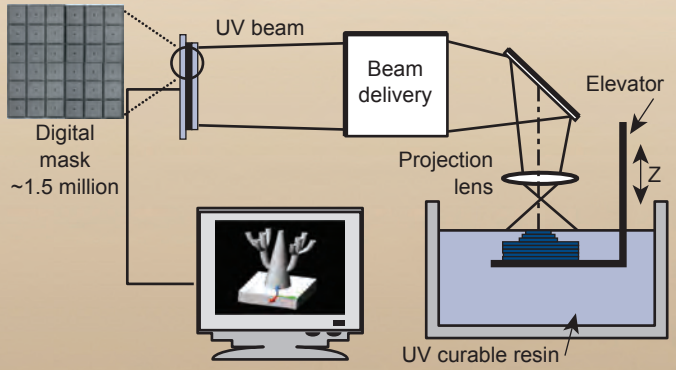

Figure 1. Schematic of a baseline PμSL system.

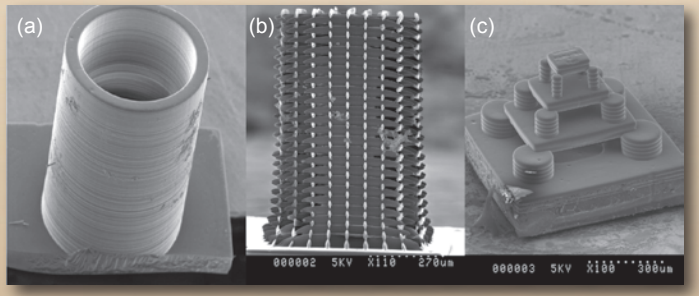

Figure 2. SEM images of (a) 300-μm cylinder, (b) lattice structure, and (c) 3-D components with overhanging features.

has been a critical factor in limiting the scope of tests that can be conducted. Research efforts across LLNL have focused on developing new fabrication techniques that can generate meso- to microscale targets with micro/nanoscale precision and features. Although much progress has been made, several key target features have been difficult to achieve. High resolution PμSL has the potential to directly impact the limitations and may also have great benefit to the newly emerging LIFE program at LLNL, which has its own set of target fabrication challenges. An ancillary impact of this work is to enable a host of new MicroElectroMechanical Systems (MEMS) devices never before conceived due to the rapid, high-resolution, fully 3-D nature of the technique.

FY2009 Accomplishments and Results

Significant progress has been made during FY2009, including:

Fabrication of many 3-D components of interest to the target community. Figure 2 highlights some of these pieces, including cylinders, lattice structures, and fully 3-D parts with overhanging features. Features as small as 5 μm have been demonstrated.

Fabrication and demonstration of a working plasmonic superlens. A scan of two slits in a substrate with spacing smaller than the wavelength of illuminating light (spacing = 200 nm) shows this phenomenon. Figure 3 shows a scan from a near field scanning optical microscope (NSOM) for the double slit geometry with the superlens material (thin film silver). Without the superlens the slits cannot be distinguished; however with the thin film of silver present, the two slits can clearly be seen as indicated by the peaks in the plot.

Validation of the optical-chemical model. Measurements from fabricated parts compared favorably to the predictions of the numerical model. In addition, fluid motion physics is now incorporated into the model.

Demonstration of microfluidics with PμSL. This is shown in Fig. 4, where a microfluidic channel was used to deliver a liquid monomer slurry with silica particles. The slurry was polymerized with a high loading of the silica and then the component flowed out of the microfluidic channel while another was fabricated in its place.

FY2010 Proposed Work

Expected achievements and goals for FY2010 include 1) integration of a plasmonic superlens with the LLNL system; 2) fabrication of nanoscale components; 3) continued improvements to structures for the target community; 4) fabrication of components with multiple materials; 5) extension of the model to light scattering from nanoparticles in suspension; and 6) use of the model as a design tool.

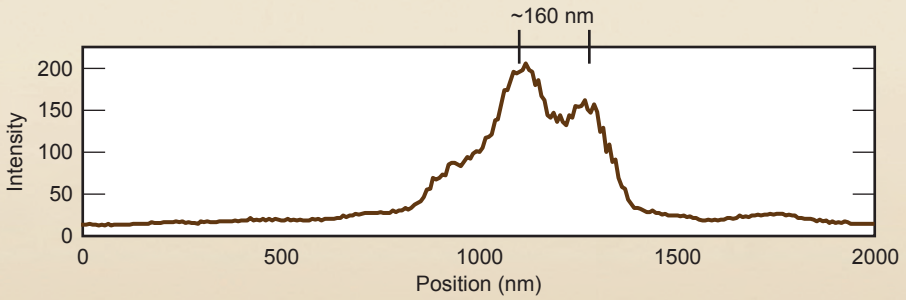

Figure 3. NSOM output for a superlens able to distinguish two slits spaced at 200 nm using 405-nm light.

Figure 4. Fabrication with a silica slurry in a microfluidic channel.

Compact High-Intensity Neutron Source Driven by Pyroelectric Crystals

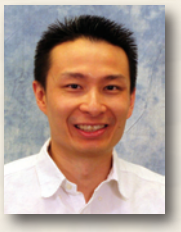

Vincent Tang
(925) 422-0126
tang23@llnl.gov

A promising technique for identification of unknown threats containing explosives or nuclear material is active interrogation via neutron bombardment and detection of induced gammas or scattered neutrons. A compact, lightweight (<10 lbs), palm-sized, pulseable neutron source or "neutron flare" requiring little electrical power could provide unique capabilities for active interrogation of these threats in the field. Pyroelectric crystals offer a means of achieving such a source by allowing a traditional neutron tube's ~100- to 200-kV power supply, ion source, and accelerator structure to be integrated on a scale an order of magnitude smaller than that of conventional technology. Figure 1 shows a schematic of the first proof-of-principle Crystal Driven Neutron Source (CDNS) experiment, illustrating the pyrofusion principle with a "coupled" ion source and acceleration approach.

Project Goals

Our objective is to establish the scientific basis for a compact palm-size pulseable neutron source driven by pyroelectric crystals using an independent nano-ion source. A primary goal is to achieve the "reversed" configuration illustrated in Fig. 2 after extending results in the coupled configuration. By decoupling the ion source from the pyroelectric crystal providing the acceleration voltage, the neutron source can be pulsed at frequencies and rates required for some interrogation applications, and the accelerating voltages tailored for either the D-D or D-T neutron producing reactions.

To achieve this, we seek a comprehensive understanding and development of pyroelectric HV sources, pyrofusion, and the development of novel nano-ion sources based on carbon nanotubes, gated nanotips, and microgap flashover ion sources. These new compact and high-yield ion sources would also have application for accelerators in general. A successful integrated demonstration with neutron production would complete the basis for the development of a palm-size "neutron flare."

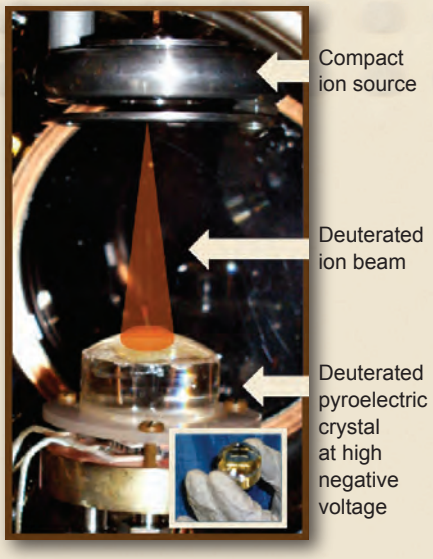

Figure 2. CDNS reversed configuration experiment. The LLNL flashover ion source is shown. The crystal in this case is biased negatively. The inset shows the palm-size scale of the crystal being tested.

Relevance to LLNL Mission

Active neutron interrogation is becoming a key approach for the detection of hidden threats including shielded nuclear materials and explosives. This results from the penetrating nature of fast neutrons and subsequent specificity of the gammas and neutrons produced through inelastic scattering and capture reactions from the target. As such, this technology will have significant impact on applications in homeland security, the military, and intelligence gathering needs. Furthermore, the technology provides new methods of interrogation that are not presently possible due to the nature of existing neutron sources. In this sense, the CDNS represents a new paradigm for active interrogation of threats. This work supports LLNL's national security mission by investigating a new technique that would enable a fundamentally new concept of operations, such as the possibility of a remote probe for covert interrogation.

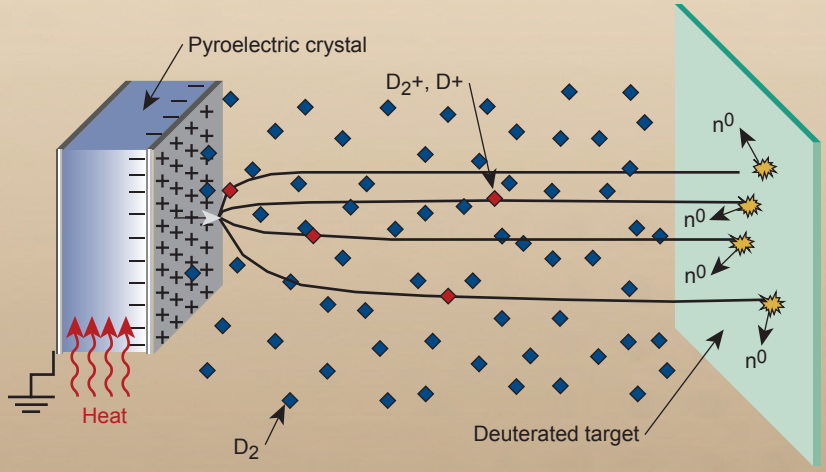

Figure 1. Illustration of pyrofusion effect using a coupled configuration.

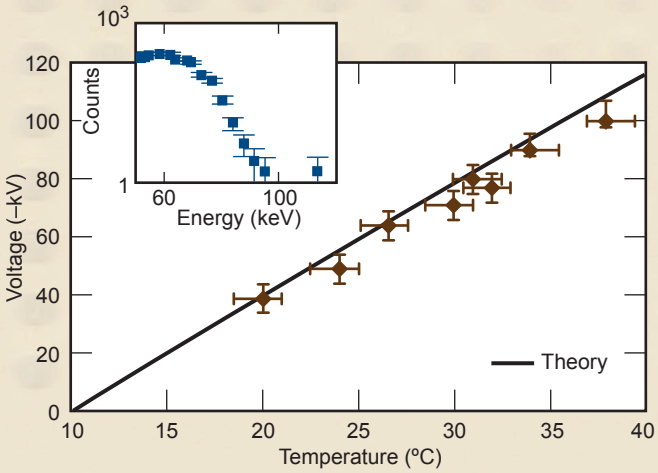

Figure 3. Bremsstrahlung-deduced crystal voltages and predicted voltages from our new pyroelectric model for different temperature cycles starting from 10 °C. The insert shows a sample bremsstrahlung spectrum indicating a crystal voltage of ~95 kV. The slight dip in measured voltages at higher temperatures is due to field emission charge losses not included in the model.

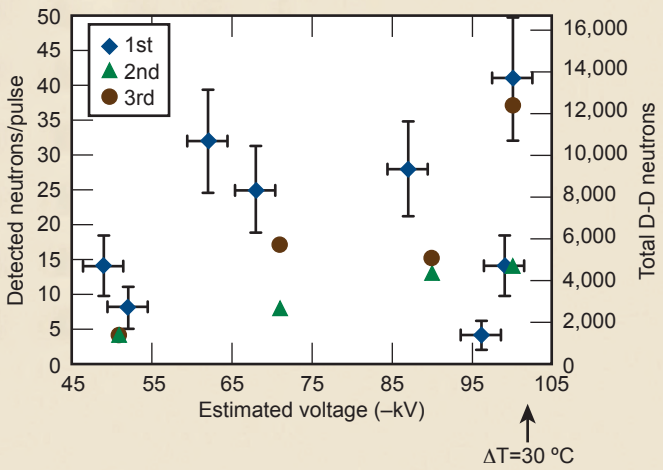

Figure 4. First pulsed pyrofusion neutron data from the CDNS reversed configuration experiment using a 1-cm-thick crystal. LLNL coupled configuration experiments have also demonstrated record D-T equivalent yields up to ~4 x 10^7 neutrons per thermal cycle at a DC rate of ~10^5 D-T equivalent n/s.

FY2009 Accomplishments and Results

We have made important progress on pyrofusion, pyroelectric HV supplies, and the required nano-ion sources for the reversed configuration. For the first time, pulsed pyrofusion via the reversed configuration using a flashover ion source and negative HV deuterated crystal targets was demonstrated. User-controlled yields greater than 10^6 D-T equivalent neutrons were achieved with pulse widths of ~100 ns.

A system model of the crystal and neutron production was constructed and benchmarked for the first time against experiments. Figure 3 illustrates the success of the model in predicting crystal voltages; Fig. 4 documents first pulsed pyrofusion data confirming the viability of the concept.

Concerning ion source development, in addition to the flashover ion source, we successfully fabricated and tested rugged gated nano-tips (Fig. 5) and are currently evaluating their performance for integrated testing in the CDNS.

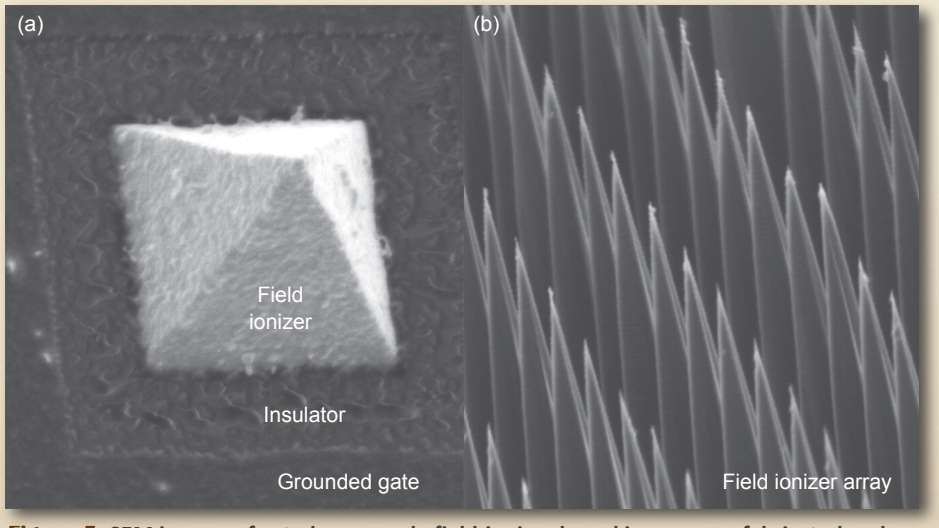

Figure 5. SEM images of gated nano-scale field-ionizer-based ion sources fabricated and studied for the reversed configuration. (a) Each ionizer tip in this ion source has an associated grounded gate. (b) The ionizers in the array for this source are grounded through a mesh suspended above the tips.

Related References

1. Tang, V., G. Meyer, S. Falabella, *et al.*, "Intense Pulsed Neutron Emission from a Pyroelectric Driven Accelerator," *Journal of Applied Physics*, **105**, 2, 026103-1-3, 2009.

2. Tang, V., *et al.*, "Fusion Neutron Science for Energy and National Security Applications," *UC Berkeley Nuclear Engineering Colloquium*, 2009.

3. Tang, V., J. Morse, G. Meyer, *et al.*, "Crystal Driven Neutron Source: A New Paradigm for Miniature Neutron Sources," *AIP Conf. Proc.*, **1099**, 870, 2009.

4. Tang, V., G. Meyer, J. Morse, *et al.*, "Neutron Production from Feedback Controlled Thermal Cycling of a Pyroelectric Crystal," *Review of Scientific Instruments*, **78**, 123504, 2007.

5. Tang, V., G. Meyer, S. Falabella, *et al.*, "Experimental Investigation and Simulations of Liquid Driven Pyroelectric Voltage Sources for Compact Accelerators," *20th Conference on the Application of Accelerators in Research and Industry*, 2008.

Microfabrication Technologies for Target Fabrication

Robin Miles
(925) 422-8872
miles7@llnl.gov

Atomic layer deposition (ALD) is the newest form of chemical vapor deposition technique capable of achieving atomic monolayer layer thickness while conformally coating in deep complex structures. This technique has been used to make novel structures such as nano-film capacitors, nano-FETS and tunable nano-magnetic structures. LLNL has purchased an ALD tool primarily for coating foams for physics targets.

Project Goals

This project was used to become familiar with the operation of the ALD tool, to make the appropriate fixtures to use the tool on a number of substrates of interest, and to characterize the tool for use with various deposited layers.

Relevance to LLNL Mission

Many materials in target fabrication, in particular the low-density foams used for current capsules, can be fabricated using an ALD system. ALD works by using a two-step deposition process. First, a vapor-phase precursor is introduced which reacts only with the substrate surface. Because only an exposed surface can be coated in this step, a monolayer is applied to the substrate and over a period of time the gas penetrates into the crevices of the structure applying this monolayer uniformly over complex structures. A second vapor-phase precursor is introduced that reacts only with the deposited layer of the first precursor to create a new layer of the desired substrate material, which is now able to react again with the first precursor gas. The precursor gases are alternately introduced into the reaction chamber and with each cycle an additional atomic layer is deposited. The high vapor pressure of the gases allows for the penetration into high-aspect-ratio features. The number of cycles determines the deposition thickness.

Many of the targets used in physics experiments require low densities of specific materials. One mechanism for producing these materials is to coat foam material with the material of interest. Foam structures such as silica aerogel are complex porous materials. The ALD precursor gases can penetrate into the lattice of the foams and apply an ultrathin layer to the foam ligaments. In this way, it is possible to create any number of low-density metal foams such as copper, tungsten, or platinum foams.

FY2009 Accomplishments and Results

The ALD system was installed in LLNL's Microfabrication Facility cleanroom. Results indicated good uniformity of the alumina depositions across a planar wafer (< 0.1% variation across a 100-mm wafer). The ALD system was also characterized for its ability to coat high-aspect-ratio features using the dynamic process mode. A covered (100) silicon wafer with anisotropic etched V-grooves was used for the experiment. The groove depths ranged from 5 to 178 µm. A standard coating process for aluminum oxide (Al_2O_3) was run at 200 °C using trimethyl aluminum (TMA) and water vapor at 1 Torr. The process is a sequential cycle involving the introduction of the precursor TMA followed by a purge evacuation. The second precursor

water vapor was introduced, followed by a purge evacuation. The precursor injection times and purge times were adjusted so that 1 Å of film was deposited in one complete cycle. The precursors must be entirely removed before the second precursor in injected, otherwise an uncontrolled chemical vapor deposition process results and the process is no longer an atomic layer deposition process.

One thousand cycles resulted in a film thickness of 1018 Å. The film thickness was measured with a Rudolph Research AutoEl-III ellipsometer at a wavelength of 632.8 nm using Program Code 211000 and refractive index of Al_2O_3 of 1.766. The Al_2O_3 coating penetration into the covered silicon V-grooves was measured using an optical microscope. A graph of the coating penetration depth verses the V-groove depth (Fig. 1) shows a coating penetration with increasing V-groove depth. The coating penetration reached a maximum of 6 mm due to the diffusion rate limitations of the precursors in the dynamic ALD mode. In order to increase the coating penetration into trench structures and foams, the static mode ALD process can be used.

A lift-off process to pattern ALD coatings was successfully created. Positive photoresist was patterned on a silicon wafer and hard baked at 120 °C. The wafer was then coated with 500 Å of Al_2O_3 using an ALD process operating at a temperature of 90 °C and chamber pressure of 1 Torr. This lower deposition temperature was selected to prevent the photoresist from outgassing or decomposing during the deposition. The photoresist was then removed by submerging the wafer in acetone in an ultrasonic bath. The ALD coating on the photoresist was successfully removed, resulting in the patterned Al_2O_3 structure shown in Fig. 2. The photoresist was not damaged during the ALD process. The 90 °C process was sufficiently low temperature to prevent flowing or decomposition of the photoresist. The rough edge artifacts on the Al_2O_3 structure are a result of the ALD coating the sidewalls of the photoresist. The rough edges can be minimized by reducing the coating thickness, thereby providing a cleaner separation of ALD film on the photoresist sidewall. The process will have applications in selective patterning of materials for sensors and catalyst.

Related References

1. Klootwijk, J. H., *et al., IEEE Electron Device Letters*, **28**, pp. 740–742, 2008.
2. Winkelmann, C. B., *et al., Nano-Letters*, **7**, pp. 1454–1458, 2007.
3. Bachmann, J., *et al., J. American Chemical Society*, **129**, pp. 9554–9555, 2007.
4. Biercuk, M. J., *et al., Appl. Phys. Lett.*, **83**, 2003.

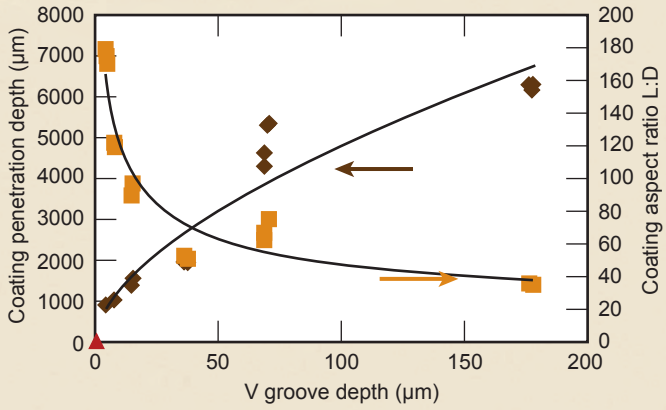

Figure 1. ALD coating penetration into silicon V groove channel.

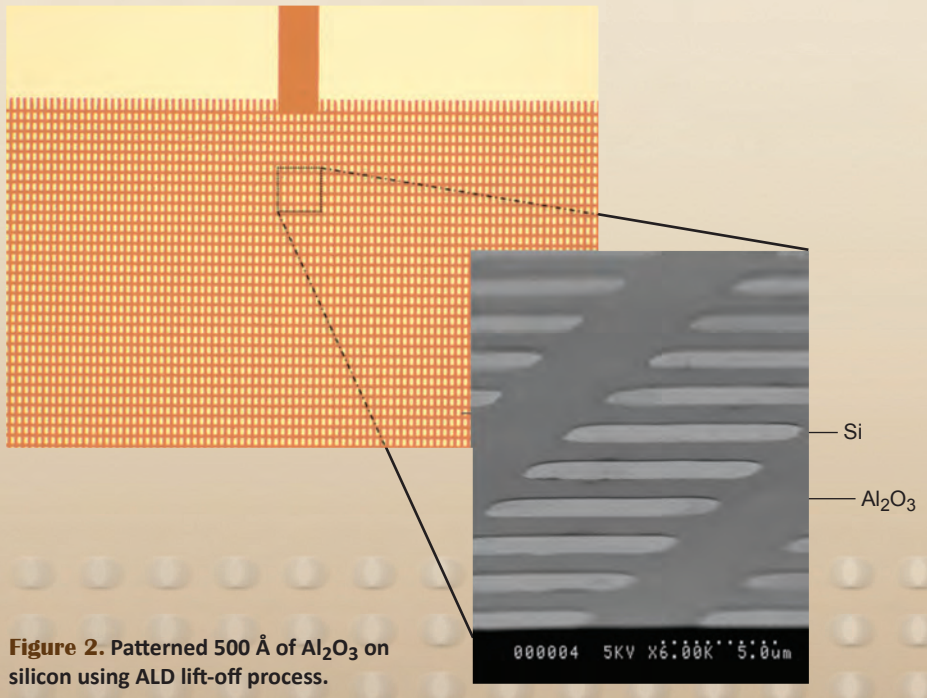

Figure 2. Patterned 500 Å of Al_2O_3 on silicon using ALD lift-off process.

Effect of Aging on Chondrocyte Function

Gabriela G. Loots
(925) 423-0923
loots1@llnl.gov

Articular cartilage is a load-bearing tissue that provides a frictionless and wear-resistant surface during joint movement. The cartilage can maintain this function for many decades in healthy joints; however, under the pathological conditions of osteoarthritis (OA), degeneration of cartilage leads to loss of mechanical integrity and motion (Fig. 1). In aging, articular cartilage stands out as a unique tissue since the cells (chondrocytes) and the majority of the extracellular matrix proteins (proteoglycans, collagen, and noncollagenous proteins) experience little turnover, resulting in a tissue that must withstand the accumulation of years of aging-associated changes without significant repair or renewal.

We have hypothesized that the age-dependent decreases in cell synthetic activity are due to a reduction in cell-matrix interactions that occur as a function of age. We have proposed to examine mechanisms by which aged cells become less responsive to mechanical loading, simulating the normal activity of aging human joints. If successful, the findings of this proposal will support the notion that healthy aging results in a loss of binding adhesion of aged cells to the matrix, which results in an understimulated cell synthesis and thus loss of homeostasis.

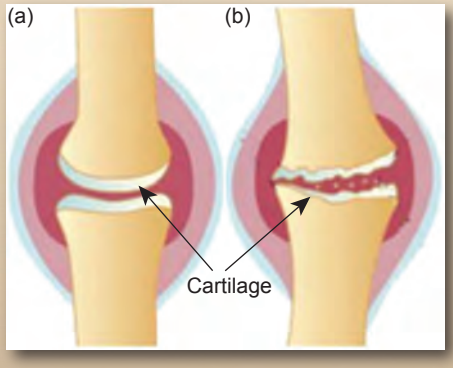

Figure 1. Cartilage in (a) healthy individuals, and (b) individuals with OA.

Project Goals

The project uses molecular biology (isolating live cells from bovine joints), biochemistry (purifying and modifying extra cellular matrix proteins from bovine joints to examine cell-protein adhesion), and bioengineering (single cell measurements using atomic force microscopy (AFM)) tools to examine age-dependent changes in molecular and mechanical properties of chondrocytes.

Three major outcomes are anticipated from these experiments. First, we aim to determine Young's modulus (compressive stiffness) and Poisson's ratio (resistance to lateral expansion) as a way to characterize physical properties of immature, young, and aged chondrocytes. We anticipate that age-dependent variations will be observed. Second, we aim to determine the molecular binding adhesion values of young and aged chondrocytes to extracellular matrix proteins that are also isolated from young or old joints. We anticipate that age-dependent changes in adhesion forces will be observed. Third, we aim to develop methods for purifying chondrocytes from mouse cells and compare them to bovine cells (the standard cells used in the field).

The long-term goal is to develop novel approaches of *in vitro* and *in vivo* analysis that can be carried out in an animal system amenable to genetic manipulations. If successful, the potential findings of this proposal could help establish a paradigm shift in the current dogma of age-dependent loss of chondrocyte function. The findings will also offer new insights into potential new target matrix proteins and receptors responsible for the decreased sensitivity of aged chondrocytes to loading. Such targets may represent novel venues for the development of alternative pharmaceutical treatments of OA.

Relevance to LLNL Mission

With the increase in our aging population, instances of OA will eventually reach epidemic proportions, creating a great economic burden on our healthcare system. In addition, excessive use and injuries to joints, commonly associated with intense physical training of our armed troops, can potentially increase the risk of developing early onset OA in young cadets, and chronically affecting the elderly veteran population. Understanding the age-related changes in biomechanical stimulation and chondrocyte function is vital for the development of OA treatments.

Our work fits into the measurement goals of LLNL's Science and Technology Pillars. Our research aim is to develop measurements for single cells using AFM, which can have applications in biomedical countermeasures.

FY2009 Accomplishments and Results

Although many approaches have been developed to model the deformation of chondrocytes *in situ*, existing theoretical models have not been able to sufficiently account for the empirical *in situ* magnitude of strain that cells are exposed to during cyclic loading. This limitation may be due to the assumption

that cells exhibit a constant compressive stiffness, despite their heterogeneous structure. We hypothesized that chondrocytes exhibit a nonlinear elastic modulus, requiring a non-Hertzian analysis of the contact of the resulting stress-strain response. To examine the indentation-dependent stiffness of chondrocytes using an AFM, the response of chondrocytes was investigated by probing the bulk stiffness of the cell using 10-µm spherical probes under different dynamical loading rates and relaxation times. The data was fit to an indentation-dependent model to empirically calculate the nonlinear elastic modulus as a function of deformation (Fig. 2).

We found that the mechanical stiffness of chondrocytes is dependent on the time the load is applied (hold time) and the time between subsequent loads (relax time) at a rapid loading rate (10 mm/s). We also found that the mechanical stiffness is not dependent on the hold time or relaxation time at a slow loading rate (1 mm/s). The dependency of elastic modulus on the hold and relaxation time at rapid loading rates suggests that the cell is deformed into a nonequilibrium conformation and the cells require anywhere from 1 to 10 s to equilibrate to a normal conformation. We believe this nonequilibrium configuration at rapid loading rates originates from the dynamic fluid rearrangement that occurs within the cell.

Related References

1. Guilak, F., and V. C. Mow, "The Mechanical Environment of the Chondrocyte: A Biphasic Finite Element of Cell-Matrix Interactions in Articular Cartilage," *J. Biomech.*, **33**, 12, pp. 1663–73, 2000.
2. Martin, J. A., and J. A. Buckwalter, "Aging, Articular Cartilage Chondrocyte Senescence and Osteoarthritis," *Biogerontology*, **3**, 5, pp. 257–64, 2002.
3. Wojcikiewicz, E. P., X. Zhang, and V. T. Moy, "Force and Compliance Measurements on Living Cells Using Atomic Force Microscopy (AFM)," *Biol. Proceed. Online*, **6**, pp. 1–9, 2004.
4. Chahine, N. O., and T. A. Sulcheck, "Inhomogeneous Mechanical Properties of Articular Chondrocytes Measured by Atomic Force Microscopy," *Materials Research Society*, #GG2.2, San Francisco, California, 2008.

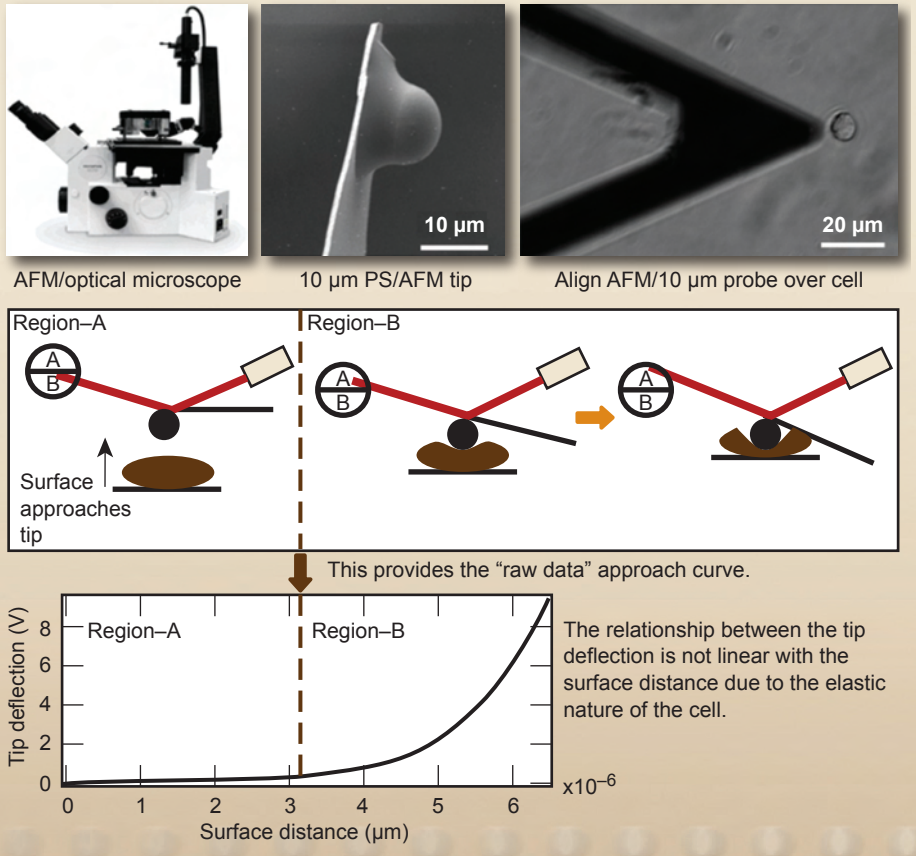

Figure 2. Process to measure the mechanical response of a cell to loading. Indentation curves were acquired where the AFM cantilever was initially not in contact with the surface (Region A). As the surface contacted the cell, the cantilever was deflected upwards, which was measured on the position sensitive detector (Region B). The nonlinear response of the cell surface to the applied force was then used to calculate the indentation-dependent stiffness of the cells.

FY2010 Proposed Work

In FY2010 we will focus on examining age-dependent changes in binding adhesion of cells and matrix proteins. We will conjugate two bovine proteins (hyaluronan and collagen type II) to beads and glass substrates and measure the adhesion forces between immature or adult chondrocytes and proteins attached to beads. We will also obtain mechanical measurements to determine if young and old chondrocytes have different affinities for extracellular proteins derived from young and old joints. In parallel experiments, we will isolate RNA from chondrocytes labeled with green fluorescent protein and carry out microarray experiments.

Measurement Technologies

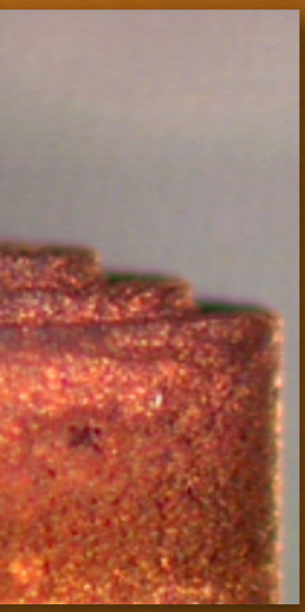

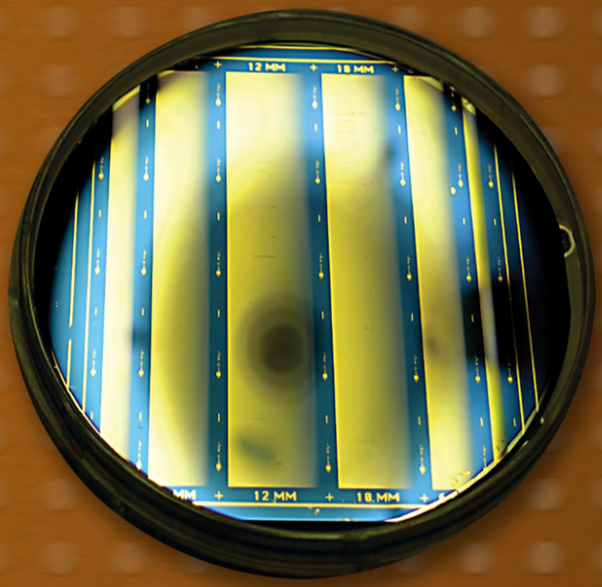

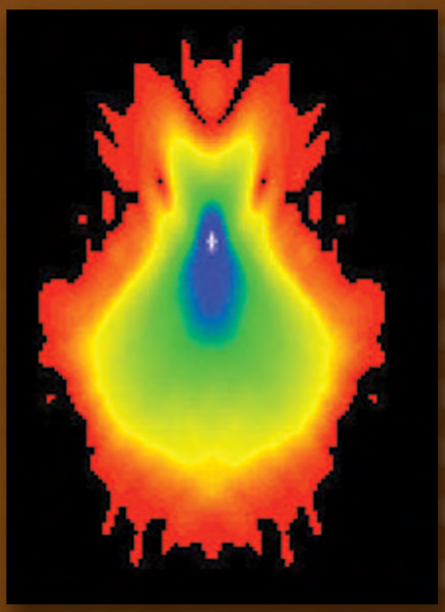

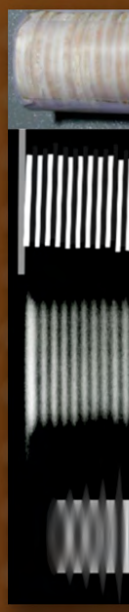

Detection, Classification, and Estimation of Radioactive Contraband from Uncertain, Low-Count Measurements

James V. Candy
(925) 422-8675
candy1@llnl.gov

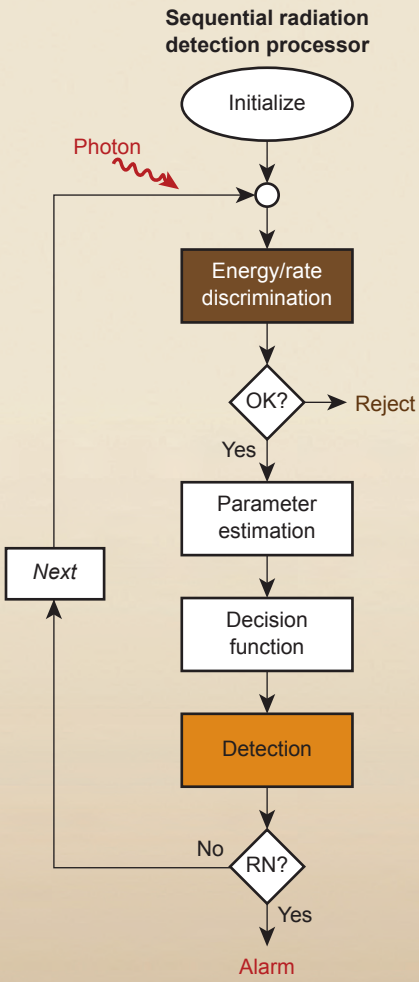

Figure 1. The Bayesian design is shown (simply) as a photon-by-photon processor using a model-based (physics-based) processor to enhance the raw detector measurement while rejecting instrumentation noise and estimating the photoelectrons through energy/rate discrimination and parameter estimation. This information is input to a function used to detect which of the target RN are present.

The detection of special nuclear material (SNM) smuggled into our nation is a critical issue for homeland security as well as for areas of nonproliferation, manufacturing, and processing and tracking of material. Today's high-speed, high-throughput computers enable physics-based statistical models that capture the essential signatures of radionuclides (RN) to be incorporated into a sequential scheme (a Bayesian sequential processor) capable of online, real-time operation. This approach is applicable to a large variety of model-based problems in many other critical areas of LLNL efforts.

This project is focused on the detection, classification, and estimation of SNM from highly uncertain, low-count RN measurements using a statistical approach based on Bayesian inference and physics-based signal processing. The effort encompasses theory, simulation, experiments, and application. It will enable the development of advanced signal/image processing techniques for the next generation of processors.

Project Goals

We expect to develop the techniques to provide fast, reliable radiation detection methods capable of making a more rapid decision about the presence of SNM with higher confidence along with the ability to quantify performance. Our goal is to reliably detect kilograms of shielded Pu with a 95% detection probability at a 5% false alarm rate in less than a minute.

Relevance to LLNL Mission

The detection of illicit SNM is a top priority of LLNL in furthering its national security mission. Radionuclide detection, classification, and identification are critical for tracking the transportation of radiological materials by terrorists, an important goal in national and international security.

FY2009 Accomplishments and Results

Our FY2009 accomplishments were:

1. performance evaluation of a Bayesian detection scheme using both simulated and controlled experimental data;
2. development of a solution to the classification problem using the physics-based Bayesian processors;
3. development of the signal-processing transport model based on point-to-point modeling by incorporating transport physics for gamma rays or photons and validating the results with full-physics simulations;
4. application of the signal-processing transport model to investigate solutions to the Compton inversion problem for source determination; and
5. development of a theoretical solution to the detection problem incorporating Compton scattering physics into the processor.

The basic structure of the processor implementation is shown in Fig. 1. After the photon information (energy/rate) is extracted from the photon by the measurement electronics, it is *discriminated* to determine if it is associated with the target RN. If so, the parametric information is enhanced by performing *parameter estimation* and is input to update the sequential decision function to *decide* (detection) whether or not the target RN is present.

Results of this photon-by-photon processor are shown in Fig. 2. A computer demonstration of the processor is available. These results are very promising and demonstrate the

potential capability of the Bayesian model-based approach to solving a variety of radiation detection problems.

Related References

1. Candy, J. V., E. Breitfeller, B. L. Guidry, D. Manatt, K. Sale, D. Chambers, M. A. Axelrod, and A. Meyer, "Radioactive Contraband Detection: A Bayesian Approach," *Proc. OCEANS09, IEEE OES Soc.*, 2009.

2. Candy, J. V., E. Breitfeller, B. L. Guidry, D. Manatt, K. Sale, D. H. Chambers, M. A. Axelrod, and A. M. Meyer, "Physics-Based Detection of Radioactive Contraband: A Sequential Bayesian Approach," *IEEE Trans. on Nuclear Science*, **56**, 6, 2, pp. 3694–3711, 2009.

FY2010 Proposed Work

In the remaining part of this project we plan to 1) demonstrate/evaluate the performance of the processor including Compton processing on controlled experimental data; 2) develop a solution based on the sodium-iodide detector measurements gathered previously; 3) cast the estimation of the threat mass problem into our model-based scheme for threat detection; and 4) develop a demonstration of the Bayesian scheme incorporating the processing of down-scattered photons (Compton) on simulated and experimental data. We expect to develop a radiation detection system capable of processing photon arrivals incorporating photon information extracted in a timely and reliable manner even in low-count environments.

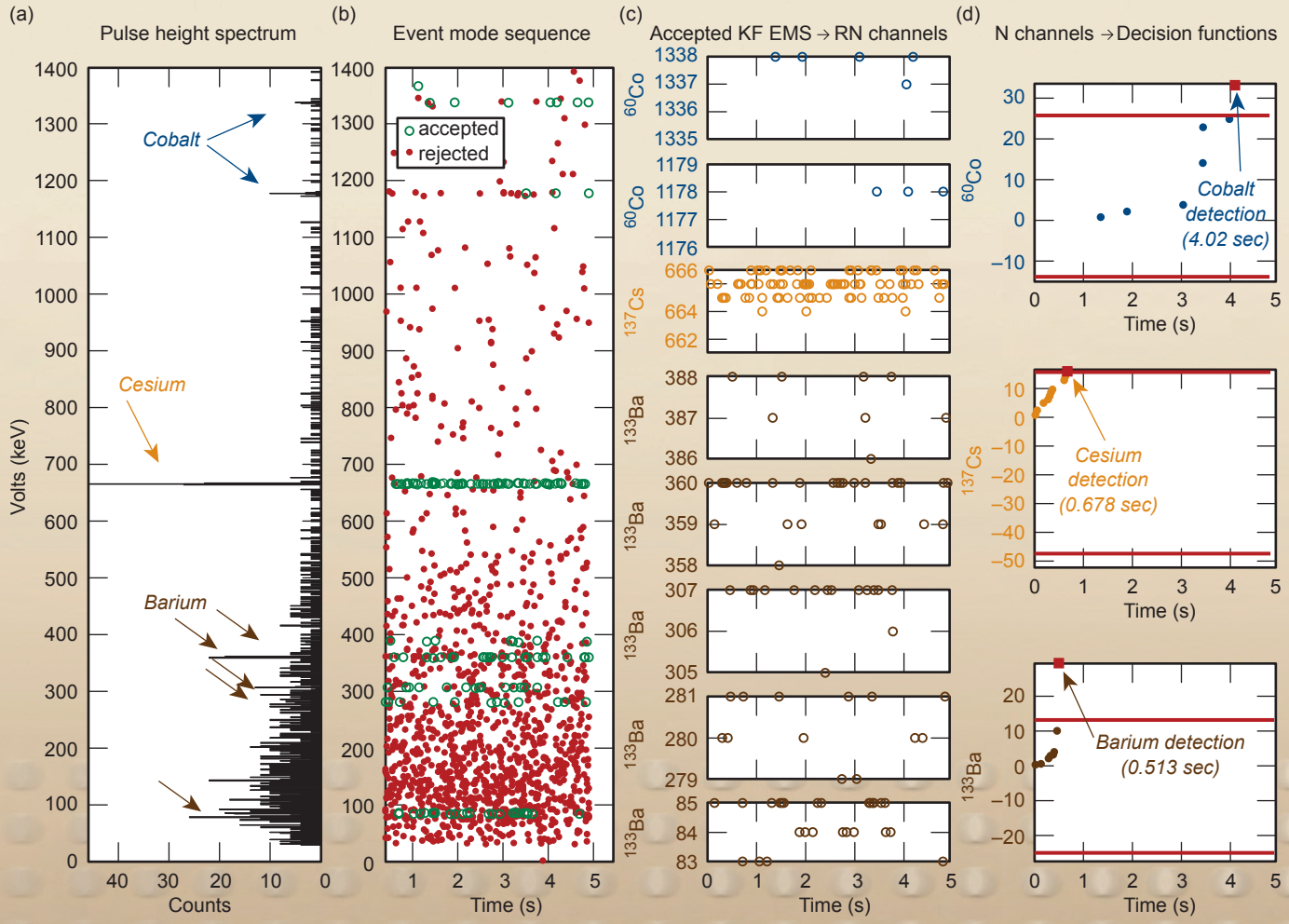

Figure 2. Sequential Bayesian detection and identification. (a) Pulse-height spectrum (after calibration); (b) photon arrivals (red) with discrimination (green circles); (c) enhanced energy estimates of targeted RN; (d) decision functions for ^{60}Co (detection time: 4.05 s), ^{137}Cs (detection time: 0.678 s) and ^{133}Ba (detection time: 0.513 s) with thresholds for RN detection/identification.

Optimized Volumetric Scanning for X-Ray Array Sources

Sean K. Lehman
(925) 423-3580
lehman2@llnl.gov

Nondestructive evaluation (NDE) is the science and technology of determining noninvasively the internal structure of manufactured parts, objects, and materials. NDE application areas include medicine, industrial manufacturing, military, and homeland security. X-ray measurement systems are most widely used because of their ability to image through a wide range of material densities, from human tissue in medical applications to the dense materials of weapon components. Traditional x-ray systems involve a single source and array detector system that rotates and/or translates about the object under evaluation. At each angular location, the source projects x rays through the object. The rays undergo attenuation proportional to the density and elemental composition of the object's constitutive material. The detector records a measure of the transmitted x rays. Mathematical algorithms are used to invert the transmission data to form images of the object. This is known as computed tomography (CT).

In recent years, single-source x-ray NDE systems have been generalized to arrays of x-ray sources. Array sources permit multiple views of the object with fewer rotations and translations of the source/detector system. The spatially diverse nature of x-ray array sources has the potential of reducing data collection time, reducing imaging artifacts, and increasing the resolution of the resultant images. Most of the existing CT algorithms were not derived from array source models with a spatially diverse set of viewing perspectives. This project addresses how best to use multiple sources and multiple detectors.

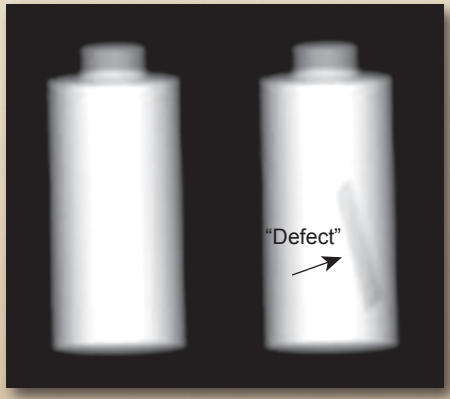

Figure 1. Simulated data used in model-based reconstruction of the proof-of-concept stacked cylinder model. The object on the left is pristine while the object on the right contains a parallelepiped "defect" which was identified and located.

Project Goals

Single-source x-ray CT data collection, processing, and imaging methods and algorithms are not applicable when the source location is expanded from 1-D to 2-D. The goal of this project is to determine the applicability of x-ray array sources to problems of interest to LLNL and its customers. It is believed that array source data collection will be faster while yielding higher resolution reconstructions with fewer artifacts. There are three tasks in the research:

1. develop forward array source analytic and computational models;
2. research and develop array source reconstruction algorithms; and
3. perform experiments.

Relevance to LLNL Mission

X-ray CT is an essential tool in LLNL's NDE area. X-ray array sources constitute leading edge technology in NDE.

FY2009 Accomplishments and Results

Two phantoms have been selected as canonical objects for the project: an alternating cylindrical stack of flat Teflon and balsa wood plates known as a "Defrise" phantom, and a cylindrically symmetric nested phantom of epoxy, aluminum, and air known as the cylindrical "As-Built" phantom. The Defrise phantom, for which array source CT data exist, serves as a contrast and resolution object. There is no array source CT data for the cylindrical "As-Built" phantom.

CTSIM (an LLNL x-ray ray-tracing transmission code) has been integrated into MATLAB. It has been used to model a stacked cylinder proof-of-concept and Defrise data.

A successful model-based inversion has been achieved with the stacked cylinder proof-of-concept model, which compared reconstructions of pristine and damaged objects. A simulated "defect" inserted in the damaged object was identified and located (Fig. 1).

A collaboration with Stanford University has been established. Real Defrise phantom data have been obtained and successful reconstructions achieved using model-based and voxel-based (ordered subset expectation maximization) algorithms (Fig. 2).

A collaboration with array source research, development, and manufacturing companies (Triple Ring and NovaRay) is forming to acquire future area array source CT data (Fig. 3).

Related References

1. De Man, B., B. Samit, D. Bequé, B. Claus, P. Edic, M. Iatrou, J. LeBlanc, B. Senzig, R. Thompson, M. Vermilye, C. Wilson, Z. Yin, and N. Pelc, "Multisource Inverse Geometry CT : A New System Concept for X-Ray Computed Tomography," *Medical Imaging: Physics of Medical Imaging Proc. of SPIE*, 6510, 2007.

2. Defrise, M., and R. Clack, "Filtered Backprojection Reconstruction of Combined Parallel Beam and Cone Beam SPECT Data," *Phys. Med. Biol.*, **40**, pp. 1517-1537, 1995.

3. Hudson, H. M., and R. S. Larkin, "Accelerated Image Reconstruction Using Ordered Subsets of Projection Data," *IEEE Transactions on Medical Imaging*, 1994.

FY2010 Proposed Work

A new Defrise phantom will be designed and manufactured at LLNL. The metrology (ground truth) does not exist for the Stanford University Defrise data, resulting in the lack of objective metrics for the current reconstructions.

Data will be collected on the new Defrise and cylindrical "As-Built" phantoms at Triple Ring. Source and detector characterization measurements will be performed.

Source and detector characterization algorithms, and remediation methods will be developed.

Research into inversion and imaging algorithms will continue.

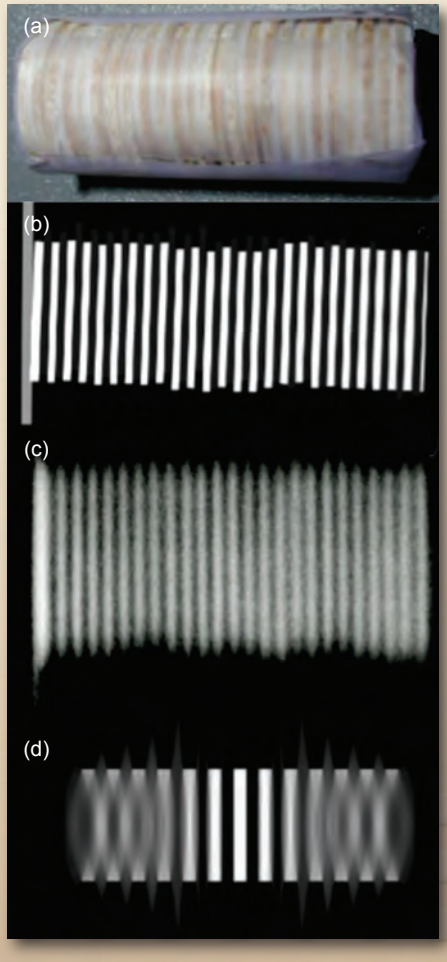

Figure 2. **(a) Photograph of Defrise stacked plate phantom. (b) Model-based reconstruction of real data. (c) Ordered-subset expectation maximization (OSEM) reconstruction of real data. (d) Traditional reconstruction of simulated Defrise phantom data. Simulated data were used to demonstrate the blurring and loss of resolution when compared with the model-based and OSEM algorithms. Simulated data were used in the traditional algorithm as the computer code failed on the real data.**

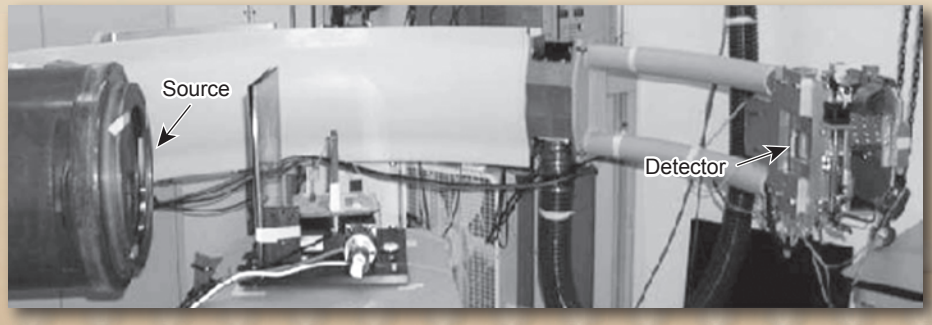

Figure 3. **Photograph of the x-ray array source and array detector system designed and developed by industrial collaborator Triple Ring. (Photo courtesy of Triple Ring)**

Standing Wave Probes for Micrometer-Scale Metrology

Richard M. Seugling
(925) 423-8525
seugling2@llnl.gov

In this project we are developing a low-force, high-aspect-ratio, mechanical probe for the nondestructive characterization of manufactured components and assemblies. The key concept for the probe is the correlation between the dynamic response of an oscillating cantilever rod (probe) and the interaction of its tip with a surface (Fig. 1). The applications for this probe begin with surface location, but may encompass the characterization of the material properties of the surface, and perhaps branch into the modification of the surface. This project is a collaborative effort between LLNL, the University of North Carolina at Charlotte (UNC-Charlotte) and an industrial partner, InsituTec Inc.

Project Goals

The project has provided the scientific understanding of a low-force, contact probe capable of being applied on a number of machine tools and metrology platforms with a characterized uncertainty based on the fundamental understanding of the probing process. The exit strategy includes continued collaboration with UNC-Charlotte, rigorous calibration efforts with NIST, engaging a commercial source of probing instruments, and the probe's practical application at LLNL and its vendors for target fabrication. Measurements have been made on geometries and materials relevant to LLNL target manufacture.

Relevance to LLNL Mission

Currently, Inertial Confinement Fusion (ICF) and high-energy-density physics (HEDP) targets comprise components with dimensions in the millimeter range, while having micrometer-scale, high-aspect-ratio functional features, including fill-tube holes and counterbores, hohlraum starburst patterns, and step-joint geometry on hemispherical targets. Future target designs will likely have additional challenging features. Variations in geometry from part to part can lead to functional limitations, such as limited flow rates during target filling, unpredictable instabilities during an ICF experiment, and the inability to assemble a target from poorly matched subcomponents. Adding to the complexity are the large number and variety of materials, components, and shapes that render any single metrology technique difficult to use with low uncertainty.

The near-term impact of this project is the expansion of LLNL's ability to accurately perform dimensional measurements of micrometer-scale features using a low-force, high-aspect-ratio probe system. The final goal of this work is to enhance LLNL's precision engineering capabilities, which encompass key core technologies supporting NIF, DNT and nanofabrication.

FY2009 Accomplishments and Results

A prototype standing wave probe system including upgraded electronics

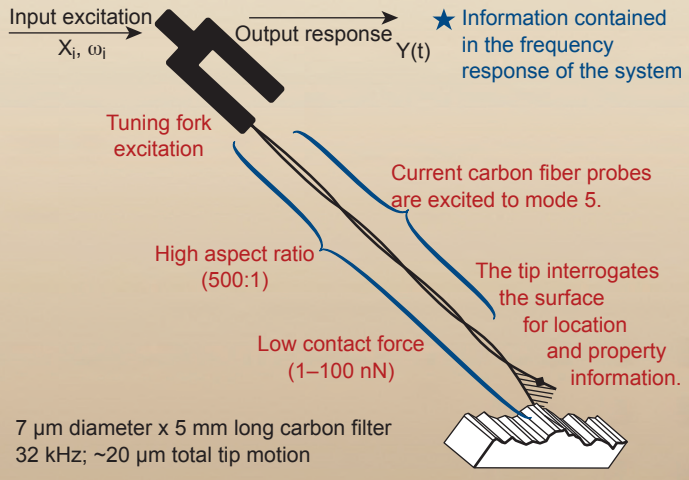

Figure 1. Schematic of probe system including tuning fork excitation and high-aspect-ratio rod. An input amplitude (X_i) at a frequency (ω_i) is applied to the tuning fork while the output amplitude (Y) is monitored as the probe comes into contact with the surface.

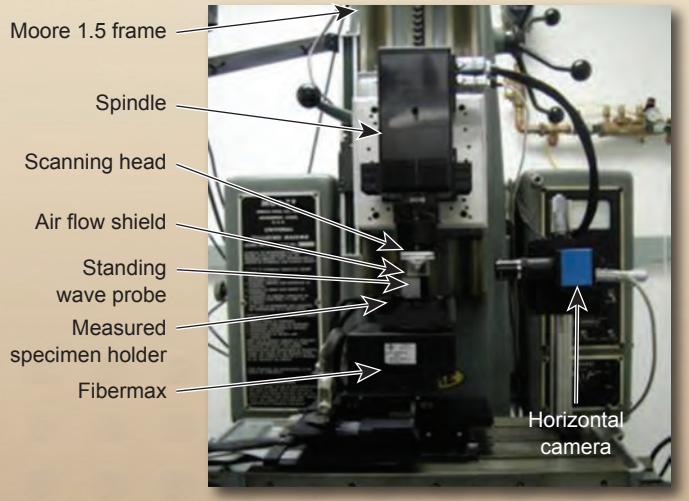

Figure 2. Standing wave probe incorporated into measurement system. Closed-loop controlled scanning stage is integrated with rotation axis onto a Moore machine.

for increased sensitivity has been built and is operational at LLNL. The system has been integrated with a precision motion stage station with subnanometer-level positioning capability and data acquisition. Probe sensitivity/repeatability to contact has been measured on a hardened steel gage block and has been shown to be at the ±10-nm level for experimental systems at both UNC-Charlotte and LLNL.

A model of the probe dynamics including contact has been derived as a stand-alone model in FORTRAN. The current scale system has a restoring force of ~100 mN due to the strain energy in the distorted beam during oscillation, while the theoretical and experimentally measured combined contact force is less than 10 mN. Scaling the system by an order of magnitude and using the same analysis, the restoring force in the oscillating beam is approximately 2 mN, while the combined surface forces are nearly 0.5 mN. Clearly, the influences of the surface forces are much more dominant at the smaller scale, as expected.

Using our modeling techniques, we have designed a system that can overcome the surface effects by either increasing the drive frequency at constant amplitude and/or shortening the fiber length to produce a larger restoring force.

A measurement system has been built at UNC-Charlotte by InsituTec Inc as a development platform for qualifying performance of the probe system measuring features and materials of interest to LLNL. The probe has been incorporated into a closed-loop controlled motion system to allow for scanning of sample features (Fig. 2).

One of the primary goals of this work was to investigate this probe technology on low-density materials used in HEDS targets. Two low-density foam artifacts were manufactured with 100-µm steps turned into the face of the structure (Fig. 3). These materials represent some of the most difficult to measure due to their combined optical and mechanical properties. Multiple measurements of each sample were made to evaluate repeatability and to investigate influence of material properties on probe performance. Based on increased probe sensitivity developed over the initial part of this effort, measurements of the foam features were done in a "non-contact" mode where the probe traces the surface without directly contacting the material.

Figure 4 shows results of the measurements for a 6% full-density (893 mg/cc) copper foam.

Related References

1. Bauza, M. B., R. J. Hocken, S. T. Smith, and S. C. Woody, "Development of a Virtual Probe Tip with an Application to High Aspect Ratio Microscale Features," *Rev. Sci. Instrum.*, **76**, p. 095112, 2005.
2. Arnau, A., Piezoelectric Transducers and Applications, Springer, New York, 2004.
3. Yang, F., "Adhesive Contact of Axisymmetric Suspended Miniature Structure," *Sensors and Actuators A*, **104**, pp. 44–52, 2003.
4. Weckenmann, A., G. Peggs, and J. Hoffmann, "Probing Systems for Dimensional Micro- and Nano-Metrology," *Measurement Science and Technology*, **17**, 2, pp. 504–509, 2006.
5. Muralikrishnan, B., J. Stone, and J. Stoup,"Area Measurement of Knife-Edge and Cylindrical Apertures Using Ultra Low Force Contact Fiber Probe," *Metrologia*, **45**, pp. 1–9, 2008.

FY2010 Proposed Work

We are building a 2-D probe system to be tested in FY2010. In addition, designs for a scaled 1-D probe and expanded 2-D probe have been modeled. Prototyping and testing are ongoing.

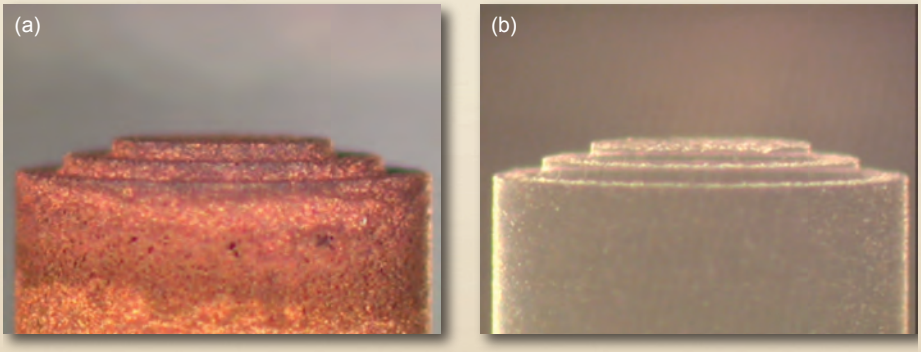

Figure 3. Two low-density foam artifacts with 100-mm steps: (a) 6% full-density (893 mg/cc) copper foam stepped sample; (b) 50-mg/cc SiO_2 foam stepped sample.

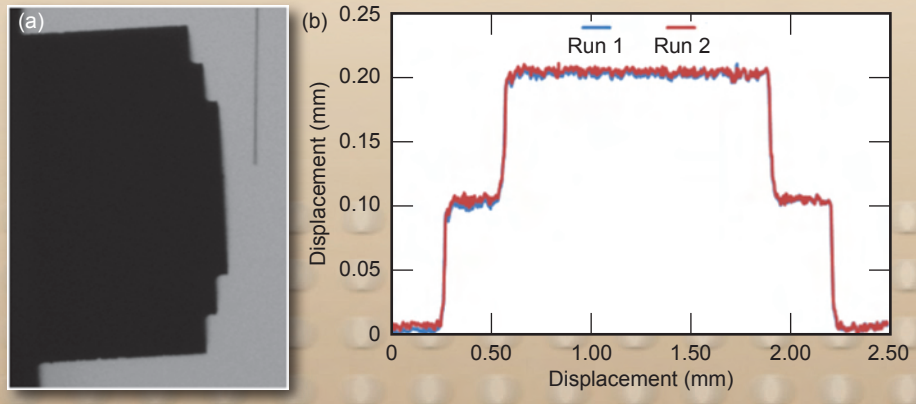

Figure 4. (a) Standing wave probe coming into contact with copper foam artifact; (b) step height measurement of 10% dense copper foam after removing tilt.

Prompt Experimental Diagnostics

John E. Heebner
(925) 422-5474
heebner1@llnl.gov

This project leverages the efforts of subsystems already in place for 1) prompt transcoding of x rays to the optical domain using x-ray induced changes in the refractive index of III-V semiconductor resonant optical cavities; and 2) high-fidelity, single-shot recording of ultrafast optical waveforms implementing temporal imaging and optical deflection-based techniques. An integrated diagnostic combining these subsystems has the potential for recording x-ray transients with near picosecond resolution and high dynamic range.

Project Goals

There are numerous challenges associated with the integration of these subsystems. They include the spectral compatibility of the transcoder and recorders, high peak power probe sources that do not disturb the transcoder resonance; synchronization of probe and signal to recorder temporal windows; and maintaining signal throughput. The goal of this project is to address these issues and arrive at an architecture that can preserve near picosecond temporal resolution and dynamic range in excess of 8 bits.

Relevance to LLNL Mission

The experimental validation of codes used to model fusion burn is critical to stockpile stewardship at LLNL. Expected radiation signatures on NIF will exhibit picosecond-scale features that span many orders of magnitude. Conventional recording instruments such as streak cameras do not have sufficient dynamic range at these timescales. The system created by this project will deliver a unique, high-performance recording capability for upcoming NIF experiments.

FY2009 Accomplishments and Results

Over the past year we made continuing improvements to the speed of the transcoder response. Building on FY2008 work, we used ion implantation to create crystal defects that aid electron-hole pair recombination and achieved the fastest transcoder devices built to date.

In a GaAs device, a sub-ps 800-nm impulse was transcoded to 930 nm with a resolution of 1.1 ps (Fig. 1). In an InGaAsP device, the same impulse was transcoded to 1560 nm, with a resolution of 2.3 ps (Fig. 2). A secondary consequence of ion implanting is increased absorption that can spoil the resonance and reduce x-ray sensitivity. To mitigate this effect, we conducted a study of post-implant thermal annealing and found it to be effective at minimizing some of the induced absorption without compromising device speed. Historically,

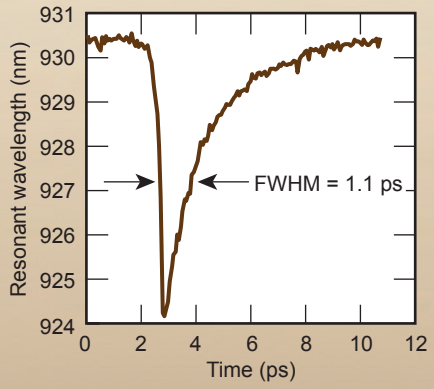

Figure 1. Optical pump-probe data from a 930-nm GaAs transcoder showing a 1.1-ps response.

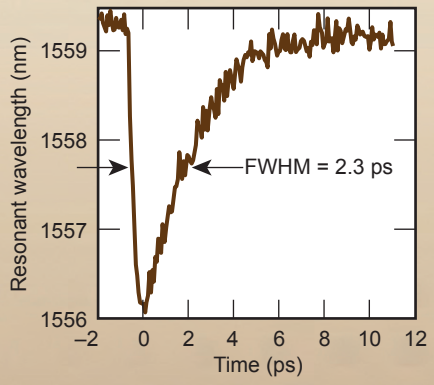

Figure 2. Optical pump-probe data from a 1560-nm InGaAsP transcoder showing a 2.3-ps response.

the epitaxial growth of the cavity layer has not been controlled with sufficient precision to guarantee resonances directly compatible with probe sources. Several effective means of resonance tuning were demonstrated this year including the addition of silicon trim layers, as well as angle and temperature adjustment.

The temporal imaging-based transient recording system has been reconfigured and rebuilt to increase the record length to 200 ps, increase the time magnification to 42 X, and improve the systems resolution and dynamic range. Figure 3 shows the response of the recorder to a single 776-fs input pulse (as measured using a frequency resolved optical grating (FROG)). Multiple single-shot output measurements recorded with a 30-GHz photoreceiver on a 20-GHz oscilloscope, after time magnification, are shown in blue, with the average width being 1.02 ps FWHM. This indicates a recording system resolution of 660 fs (Gaussian deconvolution approximation). In order to acquire recordable signals from the transcoder, we built a pulsed probe source with rectangular pulse width of 5 ns and peak power of 100 W, but only 1 mW of average power to avoid thermal activation of transcoder device.

The SLIDER all-optical streak camera recording system was upgraded with a single-box 800-nm Ti:Sapphire pump source capable of lock-to-clock operation. This will later enable relocation of the system from a tabletop to an experimental HEDP facility, and synchronization of the optically-induced deflection to the incoming signal. In order to probe the GaAs transcoders, we constructed a grating-based stretcher that generates pulse widths up to 500 ps with only 1 nm of bandwidth so as to maintain compatibility with the transcoder cavity resonance line width. Because the 930-nm probe pulses are generated with a compact optical parametric amplifier that uses a portion of the 800-nm pump source, they are inherently synchronized. As an early test of an integrated transcoder-recorder system, a transcoded optical impulse was recorded using SLIDER (Fig. 4).

Related References

1. Lowry, M. E., *et al.*, "X-Ray Detection By Direct Modulation of an Optical Probe Beam-Radsensor: Progress On Development For Imaging Applications," *Rev. Sci. Instrum.*, **75**, p. 3995, 2004.
2. Bennett, C. V., B. D. Moran, C. Langrock, M. M. Fejer, and M. Ibsen, "640 GHz Real-Time Recording Using Temporal Imaging," *OSA Conference on Lasers and Electro-Optics*, San Jose, California, May 2008.
3. Bennett, C. V., B. D. Moran, C. Langrock, M. M. Fejer, and M. Ibsen, "Guided-Wave Temporal Imaging Based Ultrafast Recorders," *OSA Conference on Lasers and Electro-Optics*, Baltimore, Maryland, May 2007.
4. Sarantos, C. H., and J. E. Heebner, "Ultrafast Optical Beam Deflection in a GaAs Planar Waveguide by a Transient, Optically-Induced Prism Array," *Integrated Photonics and Nanophotonics Research and Applications*, 2008.
5. Heebner, J. E., and C. H. Sarantos, "Progress towards the All-Optical Streak Camera," *Conference on Lasers and Electro-Optics*, 2009.

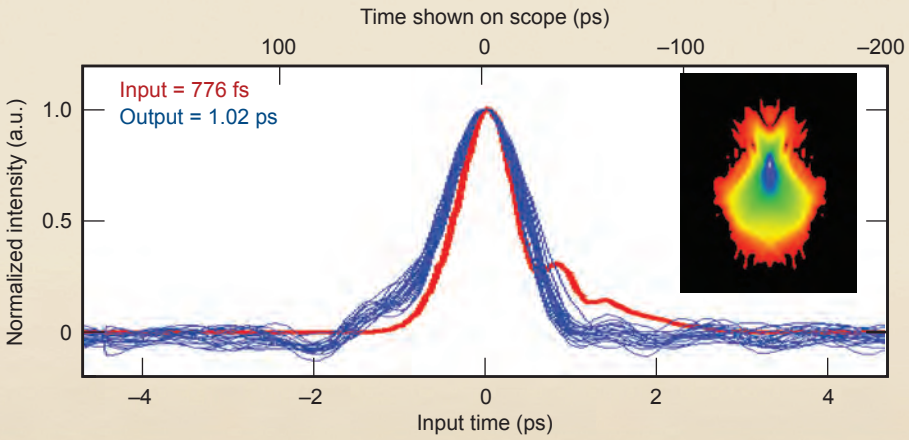

Figure 3. Temporal imaging of a 776-fs impulse with inset FROG measurement.

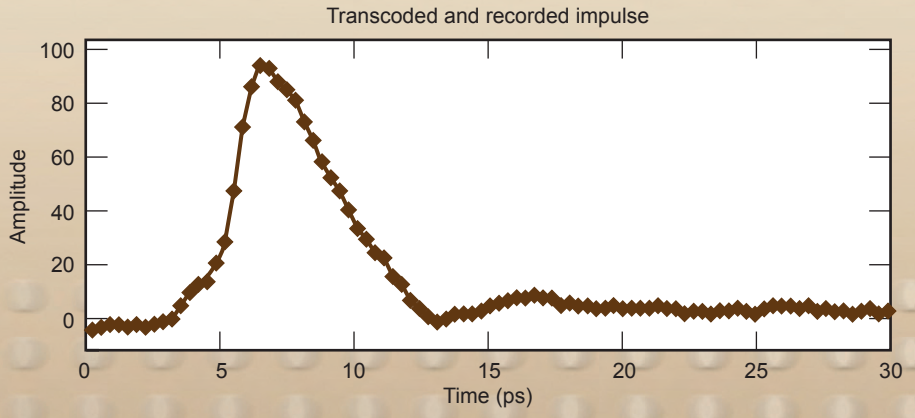

Figure 4. Pulse converted from an 800-nm above-bandgap x-ray surrogate beam using a GaAs transcoder and recorded using SLIDER. The system resolution is 3.9 ps.

Serrated Light Illumination for Deflection Encoded Recording (SLIDER)

John E. Heebner
(925) 422-5474
heebner1@llnl.gov

Conventional streak cameras are capable of sweeping electron beams at picosecond timescales. Unfortunately, space-charge effects lead to blurring at high signal levels, forcing an unforgiving tradeoff between resolution and dynamic range. Due to their absence of electrical charge, deflecting optical beams do not suffer from this limitation. A streak camera based on a deflecting optical beam thus has the promise of preserving high dynamic range at a timescale limited by the sweep rate of the deflection mechanism.

Project Goals

Deflecting a beam of light at a sweep rate required to achieve picosecond resolution has never been accomplished. We set out to demonstrate a novel deflection mechanism that can sweep an optical beam through multiple resolvable spots at near picosecond intervals. Implementing this deflection mechanism as a recorder, we set a goal of achieving near picosecond resolution with a dynamic range in excess of 8 bits.

Relevance to LLNL Mission

The experimental validation of codes used to model fusion burn is critical to stockpile stewardship at LLNL. Expected radiation signatures on NIF will exhibit picosecond-scale features that span many orders of magnitude. Conventional recording instruments such as streak cameras do not have sufficient dynamic range at these timescales. X-ray to optical transcoders are capable of imprinting x-ray signals on an optical carrier for transmission on a high bandwidth optical link. At a suitable standoff distance, the all-optical streak camera demonstrated in this project can record the imprinted signals with high fidelity and picosecond resolution on a single-shot basis.

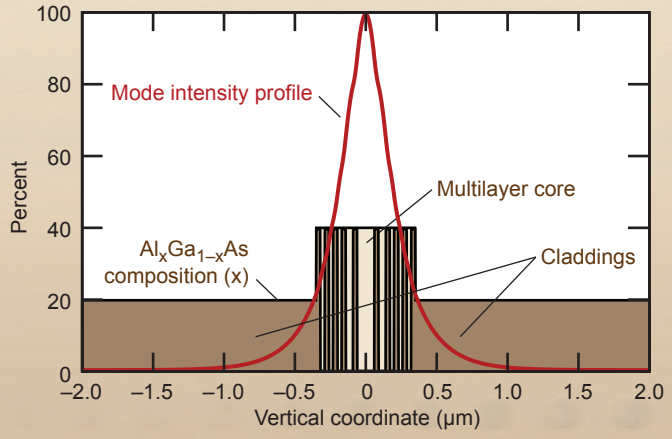

Figure 1. Multilayered waveguiding structure designed to limit the effective saturation fluence to 250 μJoules/cm². Also shown is the mode profile for the guided mode.

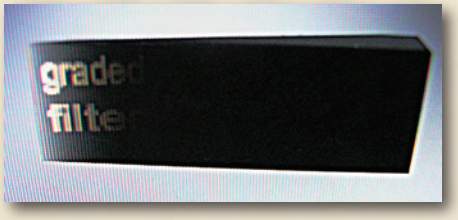

Figure 2. Graded filter used to compensate for the free-carrier absorption-induced falloff in transmission that increases with deflection.

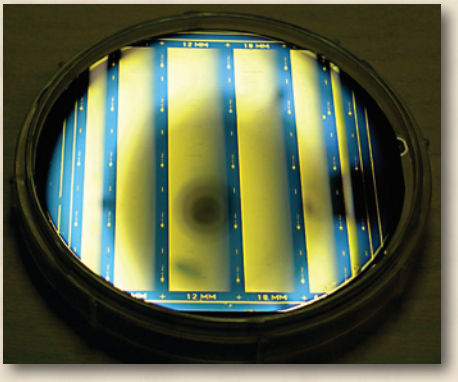

Figure 3. Array of SLIDER samples with varying gold prism patterns. The prisms are too fine to resolve and show up as a gradient. Wider patterns require more pump energy, are more likely to have end-facet defects, but can support multiple angularly multiplexed channels. Narrower patterns require less energy and result in higher device yield after cleaving, but limit the record over which the deflecting beam remains contained within the prism pattern.

FY2009 Accomplishments and Results

In the first two years of this project, we demonstrated a novel, ultrafast, optical beam deflection technique based on an array of transient, optically-induced prisms within a GaAs/AlGaAs planar waveguide. This year, we investigated the use of multilayered vs. step-index waveguides to provide extra degrees of freedom in controlling the saturation of the generated refractive index profile (Fig. 1). While it is not possible to mitigate free-carrier absorption while retaining free-carrier induced refractive index changes, we were able to demonstrate that the saturated effective index change can be limited to only the amount required for our desired resolution. This has the practical advantage of 1) stabilizing the shot-to-shot fluctuations in pump energy, and 2) flattening the effect of the nonuniformities in the pump beam creating the prisms, thereby reducing the wavefront error induced breakup of the deflecting focused spot. Free-carrier absorption limits the useful dynamic range to approximately 50 resolvable spots that can be allocated for high resolution or long record. To mitigate this, we investigated the use of transmission flattening by use of attenuation gradients inserted just before the recording plane of the camera.

To test this concept, we fabricated a custom graded filter from absorbing glass with a wedge angle designed to compensate for the reduction in transmission as a function of deflection (Fig. 2). We also varied the width of the serrated prism patterns to optimize the deflection per unit pump fluence (Fig 3). Using an optimized 8-mm-wide sample, we recorded several ring-down patterns (Fig. 4) and achieved a temporal resolution of 1.1 ps.

Related References

1. Heebner, J. E., and C. H. Sarantos, "All Optical Streak Camera, " *Conference on Lasers and Electro-Optics*, 2008.
2. Heebner, J. E., and C. H. Sarantos, "Ultrafast Optical Beam Deflection in a GaAs Planar Waveguide by a Transient, Optically-Induced Prism Array," *Integrated Photonics and Nanophotonics Research and Applications*, 2008.
3. Heebner, J. E. and C. H. Sarantos, "Progress towards the All-Optical Streak Camera," *Conference on Lasers and Electro-Optics*, 2009.
4. Bennett, B. R., R. A. Soref, and J. A. del Alamo, "Carrier-Induced Change in Refractive Index of InP, GaAs, and InGaAsP," *IEEE Journal of Quantum Electronics*, **26**, p. 113, 1990.

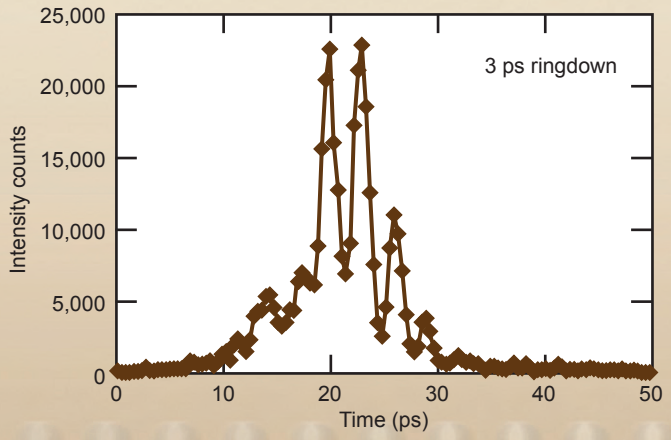

Figure 4. Recorded ring-down pattern from a Gires-Tournois cavity with 3-ps round trip spacing. Four pulses are clearly resolved within 10 ps. The resolution is 1.1 ps. Most of the background pedestal results from scattering at defects present at the waveguide facets.

Engineering Systems for Knowledge & Inference

Toward Understanding Higher-Adaptive Systems

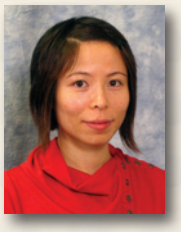

Brenda M. Ng
(925) 422-4553
ng30@llnl.gov

States available to the Red Team and the Blue Team in our I-POMDP model of the money laundering process. The Red Team's state denotes the location of money being laundered, while the Blue Team's state denotes the location of sensors deployed by law enforcement to surveil money laundering activities.

		Red	Blue
DP	Red's starting state: dirty pot	✓	
N	Blue's starting state: no sensors deployed		✓
BA	Domestic bank accounts	✓	✓
IN	Insurance products	✓	✓
SE	Securities	✓	✓
OF	Offshore account	✓	
SH	Shell company	✓	✓
TR	Trust	✓	✓
LO	Corporate loans	✓	✓
CA	Casino account	✓	✓
RE	Real estate	✓	✓
CP	Red's winning state: clean pot	✓	

This project is a two-year effort that seeks to understand higher-adaptive systems, which are systems that can modify their structures and behaviors in response to attempts at detection or regulation. These systems are ubiquitous: in the real world, there are many entities, such as money launderers and cyber intruders, whose fundamental behavior changes upon probing or intervention by an observer. Such a system outputs observations (*e.g.*, an unintentional trail of evidence connected to its activities) and adversarial actions (*e.g.*, direct assaults/countermoves against its opponent). In particular, these actions can span a spectrum of aggression, from limiting information available to its opponent to misleading the opponent into making the wrong moves or assumptions.

Project Goals

The objective of this work is to explore and extend as necessary current decision-theoretical frameworks and algorithms for solving real-world adversarial problems, especially those involving adversaries that are higher-adaptive, capable of disinformation and deceptive actions. The results of this work can provide foundational knowledge for building a computationally efficient framework that can characterize and respond to dynamically changing, deceptive adversarial systems. This knowledge will be invaluable for future advanced studies of even more adaptive and aggressive adversarial systems, such as those that limit resources as well as information from their opponents. This type of study has scientific merit in both the AI and game theory communities; it also provides the basis for addressing significant national security threats.

Relevance to LLNL Mission

This project is relevant to furthering LLNL's missions in Inference and Adversarial Modeling. This work can provide important insights about real-world adversarial modeling and higher-adaptive systems, with applications in biological systems (*e.g.*, regulatory networks), law enforcement (*e.g.*, money laundering and drug trafficking), and homeland security (*e.g.*, terrorist networks, cyber attacks, and proliferation of weapons of mass destruction).

FY2009 Accomplishments and Results

In FY2009, we used money laundering as the motivating application. Money laundering is a crime in which the funds from illegal activity are disguised to appear legitimate. It is an extremely pervasive crime and can be difficult to detect, as criminals often try to diffuse the "money trail" via a complex series of financial transactions. In this work, we created a decision-theoretic model of the money laundering process, from the perspectives of both criminals and law enforcement. To model the money laundering process, we used an interactive partially observable Markov decision process (I-POMDP), which extends POMDPs for modeling multiagent adversarial systems.

In an I-POMDP, each agent maintains beliefs about the physical states of the environment, and the models of other agents (*e.g.*, how each of the other agents might perceive or act in the same environment). This makes I-POMDP

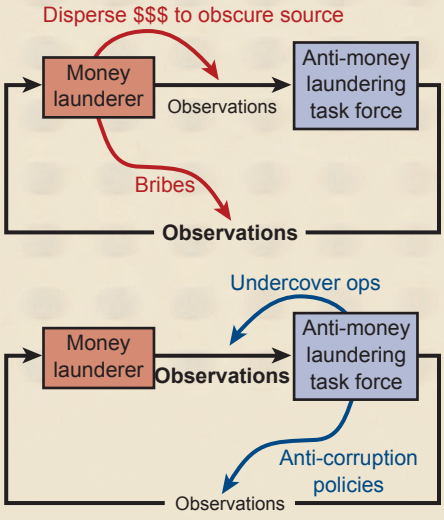

Figure 1. Schematic for understanding higher-adaptive systems. Agents can take actions to increase their own observations about the opponent, as well as actions that limit the opponent's observations.

novel with respect to other multiagent modeling frameworks in that it incorporates the notion of *nested intent* into the belief of each agent, allowing for the modeling of agents that "game" against each other, as in our money laundering scenario.

The agents in our model are the Red Team (money launderers) and the Blue Team (law enforcement). Red's goal is to evade capture while moving assets through a financial network, while Blue's goal is to find and confiscate Red's assets. The joint state consists of the locations of Red's assets and Blue's sensors. Some observations are automatically generated according to reporting requirements mandated by the Bank Secrecy Act (BSA), while other observations are obtained through actions related to active surveillance. Our I-POMDP model consisted of 99 joint states; four actions, and four observations for the Red Team; and nine actions and 11 observations for the Blue Team. Thus, the overall size of our problem (measured in terms of states × actions × observations × players) is nearly 20 times that of the largest previously solved instance in the I-POMDP literature.

To solve an I-POMDP is to determine the *optimal policy*, which for every possible observation produces an optimal action that maximizes the agent's expected reward. Previous work has shown that value iteration can be used to solve I-POMDPs. As part of our implementation of the value iteration algorithm, we applied approximations such as the *interactive particle filter* (I-PF) to address the belief complexity that increases with the number of states, and *reachability tree sampling* (RTS) to address the policy complexity that increases with number of time steps or *horizons* in the decision process. To make our problem tractable, we applied RTS to prune not only the agent's policy tree, but also the policy tree of its opposing agent. We also experimented with limited look-ahead strategies for the opposing agent.

The table and Figs. 1 and 2 illustrate our process.

Related References

1. Doshi, P., and P. Gmytrasiewicz, "Monte Carlo Sampling Methods for Approximating Interactive POMDPs," *Journal of Artificial Intelligence Research*, **34**, pp. 297–337, 2009.
2. Gmytrasiewicz, P., and P. Doshi. "A Framework for Sequential Planning in Multiagent Settings," *Journal of Artificial Intelligence Research*, **24**, pp. 49–79, 2005.
3. United States Treasury, "2007 National Money Laundering Strategy," Technical Report, Office of Terrorism and Financial Intelligence, United States Treasury, 2007.

FY2010 Proposed Work

In FY2010, we will shift our focus from passive adversaries with fixed dynamics to deceptively aggressive adversaries with adaptive dynamics. We will augment our framework to 1) include model learning capabilities for inferring the adversary's unknown dynamics; and 2) address deception and unreliability in the adversary's observable outputs.

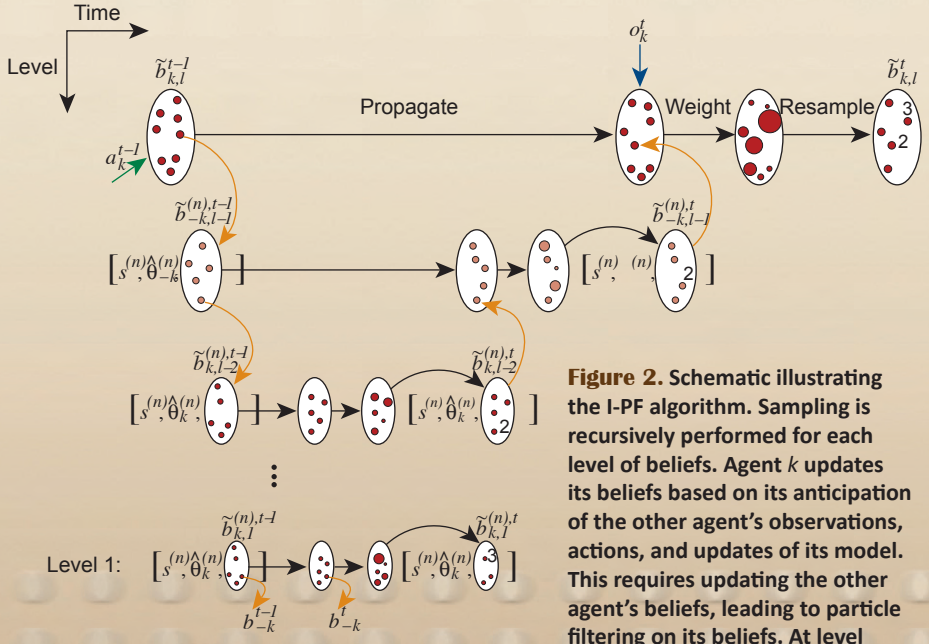

Figure 2. Schematic illustrating the I-PF algorithm. Sampling is recursively performed for each level of beliefs. Agent *k* updates its beliefs based on its anticipation of the other agent's observations, actions, and updates of its model. This requires updating the other agent's beliefs, leading to particle filtering on its beliefs. At level 1, agent *k* uses a POMDP belief update to infer the other agent's level 0 belief.

Enhanced Event Extraction from Text via Error-Driven Aggregation Methodologies

Tracy D. Lemmond
(925) 422-0219
lemmond1@llnl.gov

Knowledge discovery systems are designed to construct massive data repositories via text and information extraction methodologies, and then infer knowledge from the ingested data, allowing analysts to "connect the dots." The extraction of relational information (such as triples and events) and related entities (such as people and organizations) generally forms the basis for data ingestion. Unfortunately, these systems are particularly vulnerable to errors introduced during the ingestion process, often resulting in misleading or unreliable analysis. Though state-of-the-art extraction tools achieve insufficient accuracy rates for practical use, not all extractors are prone to the same types of error. This suggests that substantial improvements may be achieved via appropriate combinations of existing extraction tools, provided their behavior can be accurately characterized and quantified.

Our research is addressing this problem via the aggregation of extraction tools based on a general inferential framework that exploits their strengths and mitigates their weaknesses.

Project Goals

The objective of this effort is to develop a significantly improved entity/event extraction system that will enable 1) greater insight into the downstream effects of extraction errors; 2) more accurate automatic text extraction; 3) better estimates of uncertainty in extracted data; 4) effective use of investments by the Natural Language Processing community; and 5) rapid incorporation of future advancements in extraction technologies.

An extensive analysis of the error processes of individual extractors will yield insights into their synergistic and conflicting behaviors. These insights will be leveraged to configure a collection of base extractors, via a general inferential framework, into an aggregate meta-extractor with substantially improved extraction performance (Figs. 1 and 2).

Relevance to LLNL Mission

Nonproliferation, counterterrorism, and other national security missions rely on the acquisition of knowledge that is buried in unstructured text documents too numerous to be manually

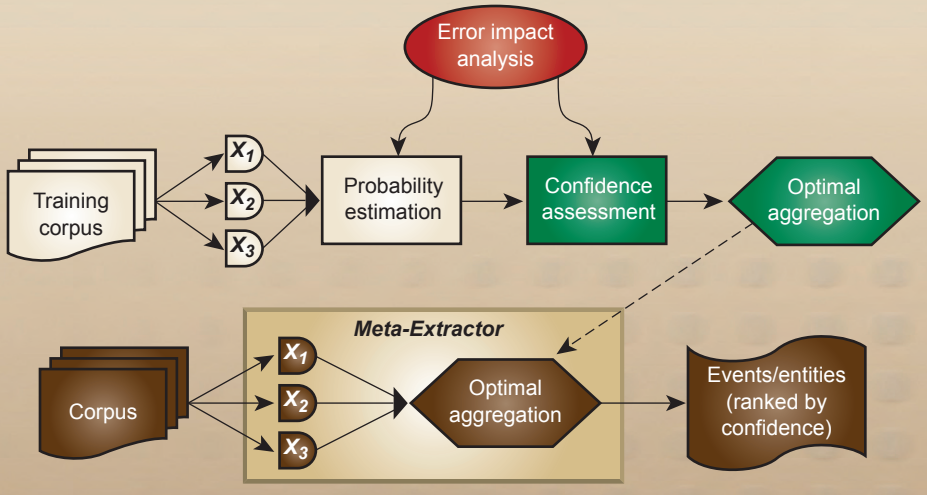

Figure 1. Schematic of the meta-extraction system.

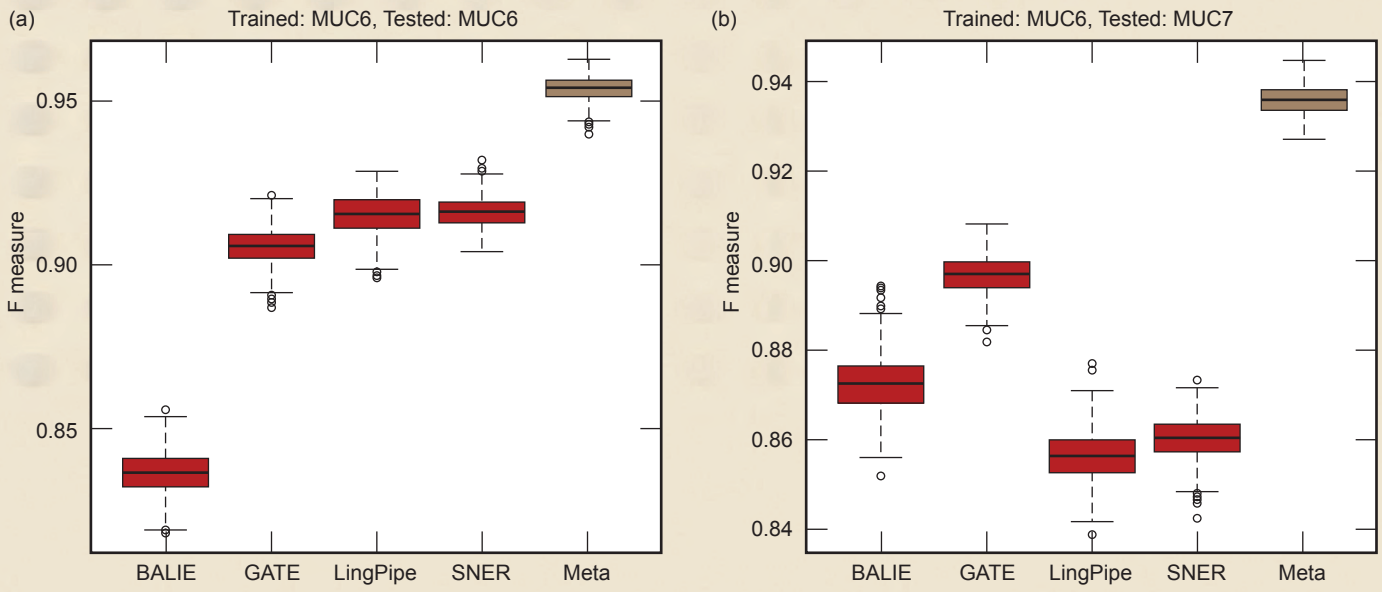

Figure 2. **Box plots showing bootstrapped samples of the weighted mean of F measure. The data come from MUC (Message Understanding Conferences) 6 and 7; [(a) and (b), respectively]. The meta-extractor shows statistically significant improvement over the base extractors.**

processed. Systems are under development by LLNL and its customers that must automatically extract critical information from these sources. To enable effective knowledge discovery, however, extraction error rates must be driven down. Probabilistic aggregation of extractors is a promising and innovative approach to accomplishing this goal. This effort directly supports the Engineering Systems for Knowledge and Inference (ESKI) focus area, the Text to Inference R&D area, and the Cyber, Space, and Intelligence strategic mission thrust in the LLNL five-year strategic roadmap. Successful completion of this research will provide highly valued and unprecedented inference and decision-making capabilities to internal programs, such as IOAP and CAPS, and to external customers such as DHS, DoD, and the IC.

FY2009 Accomplishments and Results

Insights gained in event extraction error analyses performed in FY2008 motivated a graduated approach to triple/event aggregation that is founded upon the aggregation of extracted entities. To this end, we have developed a novel aggregation methodology (the "meta-extractor") focused on entity extraction that can be generalized to multiscale triples (for example, simple events) and more complex event aggregation solutions. This methodology couples an innovative pattern-based approach with probabilistic methods to characterize the marginal and joint behaviors of entity extraction tools and aggregate their output. Empirical studies have shown that the developed aggregation methodologies achieve up to 120% improvement in performance over the best extraction tool included in the study. Moreover, these methodologies have been shown capable of determining the true entities when *all* of the extraction tools fail, a significant achievement in natural language processing.

Related References

1. Chen, M., Q. Shao, and J. Ibrahim, Monte Carlo Methods in Bayesian Computation, Springer, 2000.
2. Efron, B., and R. Tibshirani, An Introduction to the Bootstrap, Chapman and Hall, 1993.
3. Kohavi, R., "A Study of Cross-Validation and Bootstrap for Accuracy Estimation and Model Selection," *Proc. of the Fourteenth International Joint Conference on Artificial Intelligence*, **2**, 12, pp. 1137–1143, 1995.

FY2010 Proposed Work

In FY2010, we will extend and enhance the entity aggregation methodologies developed in FY2009 to more effectively leverage other information, such as entity type. In addition, we will continue to develop and generalize these methods to address the more general triple aggregation task. This unprecedented work will synergistically leverage the insights gained from the event error analyses performed in FY2008 and the entity aggregation research performed in FY2009 to produce a state-of-the-art extensible methodology for triple aggregation. If successful, our research will represent a significant breakthrough in natural language processing and knowledge discovery.

Entity Extractor Aggregation System

Tracy D. Lemmond
(925) 422-0219
lemmond1@llnl.gov

The extraction of relational information (such as triples and events) and entities (such as people and organizations) from unstructured text often forms the basis for data ingestion by Knowledge Discovery (KD) systems. These systems enable analysis and inference on massive sets of data and are particularly vulnerable to errors introduced during the ingestion process.

Though state-of-the-art extraction tools achieve insufficient accuracy rates for practical use, not all extractors are prone to the same types of error. This suggests that improvements may be achieved via appropriate combinations of existing extraction tools, provided their behavior can be accurately characterized and quantified. Several methodologies that combine pattern-based and probabilistic approaches exist to address the entity extraction problem via the aggregation of extraction tools (*i.e.*, base extractors). The focus of this effort has been to construct an operational prototype of these algorithms within an extensible framework that will allow future advancements to be easily incorporated and enable the generation of detailed results and performance assessment data.

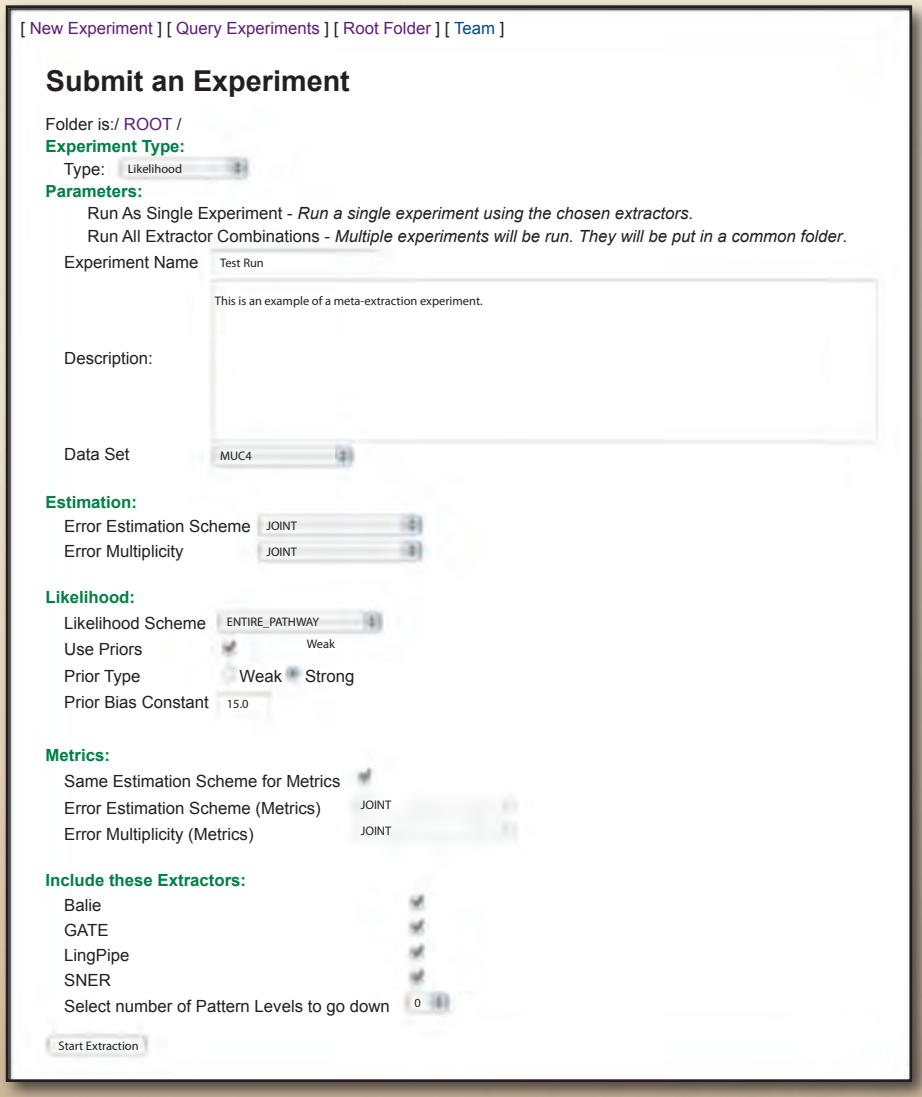

Figure 1. Parameter selection for a meta-extractor experiment.

Project Goals

Key objectives for this system include 1) building a "plug-and-play" extensible framework to enable the incorporation of future algorithmic advancements; 2) automating the execution of experiments and the navigation of experimental results; 3) providing tools for evaluating the performance of base extractors and of the final aggregated output; and 4) incorporating methodology characterization tools that facilitate algorithm optimization.

Relevance to LLNL Mission

Nonproliferation, counterterrorism, and other national security missions rely on the acquisition of knowledge that is buried in unstructured text documents too numerous to be manually processed. Systems are being worked on by LLNL and its customers that must automatically extract entities from these sources. Methodologies have been created that significantly advance entity extraction capabilities. Bringing these capabilities to an operational status is critical to the timely deployment of KD technologies that will impact LLNL mission goals. This effort directly supports LLNL's Engineering Systems for Knowledge and Inference (ESKI) Text to Inference area and the Cyber, Space, and Intelligence strategic mission thrust in the LLNL five-year strategic roadmap. The completed system will provide highly valued and unprecedented entity extraction capabilities to internal programs, such as IOAP and CAPS, and to external customers such as DHS, DoD, and the IC.

FY2009 Accomplishments and Results

The entity extractor aggregation tool has been constructed to serve as both a prototype of existing aggregation methodologies (meta-extractors) and an environment to enable future advancements. Four types of meta-extraction methodologies have been prototyped within the tool, each consisting of various interlinked modular components that include 1) extractor error detection; 2) error probability estimation; 3) hypothesis and likelihood computation; and 4) input/output of entity data. Each component relies on user-specified parameters that determine its behavior within a given algorithm (Fig. 1). For example, the user may specify the desired error space (the specific errors of interest) for the extractor error detection and probability estimation components. Execution of meta-extraction algorithms has been fully automated within the tool, and queuing of experiments has been enabled.

Performance estimation for the base and meta-extractors takes place via cross-validation, in which the data must be partitioned into multiple folds with associated performance estimates that are typically averaged to obtain an overall estimate. The aggregation tool runs these folds in parallel for increased efficiency. When an algorithm has been completed, the user is provided with an array of statistics associated with the execution. These include 1) error counts and probability estimates for the base and meta-extractors; 2) detailed output of the entities extracted by the base extractors, the space of hypothesized ground truths proposed by the meta-extractor, and the corresponding meta-extractor result; 3) the rate that events of interest occur (*e.g.*, the frequency with which the meta-extractor recreates the truth when all base extractors fail); and 4) the original text with extracted and ground truth entities highlighted (Fig. 2). This information collectively provides substantial insight into the behaviors and performance of meta-extraction methodologies, enabling the potential for algorithm optimization and enhancement.

Related References

1. Chen, M., Q. Shao, and J. Ibrahim, Monte Carlo Methods in Bayesian Computation, Springer, 2000.

2. Kohavi, R., "A Study of Cross-Validation and Bootstrap for Accuracy Estimation and Model Selection," *Proc. of the Fourteenth International Joint Conference on Artificial Intelligence*, **2**, 12, pp. 1137–1143, 1995.

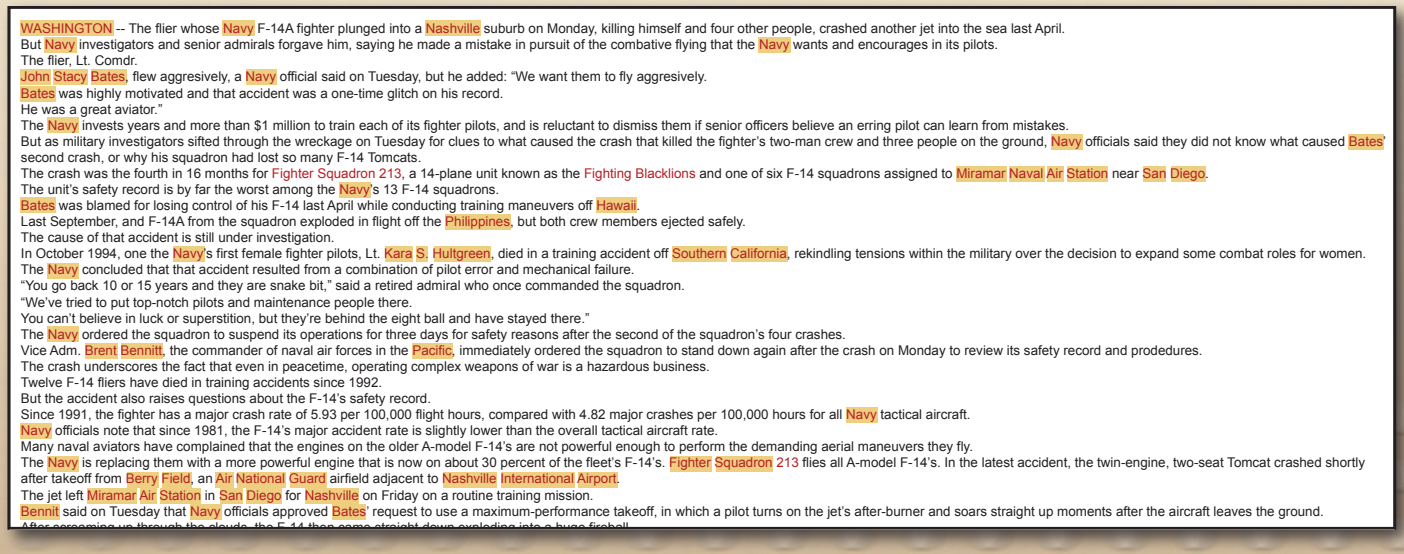

WASHINGTON -- The flier whose Navy F-14A fighter plunged into a Nashville suburb on Monday, killing himself and four other people, crashed another jet into the sea last April.
But Navy investigators and senior admirals forgave him, saying he made a mistake in pursuit of the combative flying that the Navy wants and encourages in its pilots.
The flier, Lt. Comdr.
John Stacy Bates, flew aggresively, a Navy official said on Tuesday, but he added: "We want them to fly aggresively.
Bates was highly motivated and that accident was a one-time glitch on his record.
He was a great aviator."
The Navy invests years and more than $1 million to train each of its fighter pilots, and is reluctant to dismiss them if senior officers believe an erring pilot can learn from mistakes.
But as military investigators sifted through the wreckage on Tuesday for clues to what caused the crash that killed the fighter's two-man crew and three people on the ground, Navy officials said they did not know what caused Bates' second crash, or why his squadron had lost so many F-14 Tomcats.
The crash was the fourth in 16 months for Fighter Squadron 213, a 14-plane unit known as the Fighting Blacklions and one of six F-14 squadrons assigned to Miramar Naval Air Station near San Diego.
The unit's safety record is by far the worst among the Navy's 13 F-14 squadrons.
Bates was blamed for losing control of his F-14 last April while conducting training maneuvers off Hawaii.
Last September, and F-14A from the squadron exploded in flight off the Philippines, but both crew members ejected safely.
The cause of that accident is still under investigation.
In October 1994, one the Navy's first female fighter pilots, Lt. Kara S. Hultgreen, died in a training accident off Southern California, rekindling tensions within the military over the decision to expand some combat roles for women.
The Navy concluded that that accident resulted from a combination of pilot error and mechanical failure.
"You go back 10 or 15 years and they are snake bit," said a retired admiral who once commanded the squadron.
"We've tried to put top-notch pilots and maintenance people there.
You can't believe in luck or superstition, but they're behind the eight ball and have stayed there."
The Navy ordered the squadron to suspend its operations for three days for safety reasons after the second of the squadron's four crashes.
Vice Adm. Brent Bennitt, the commander of naval air forces in the Pacific, immediately ordered the squadron to stand down again after the crash on Monday to review its safety record and prodedures.
The crash underscores the fact that even in peacetime, operating complex weapons of war is a hazardous business.
Twelve F-14 fliers have died in training accidents since 1992.
But the accident also raises questions about the F-14's safety record.
Since 1991, the fighter has a major crash rate of 5.93 per 100,000 flight hours, compared with 4.82 major crashes per 100,000 hours for all Navy tactical aircraft.
Navy officials note that since 1981, the F-14's major accident rate is slightly lower than the overall tactical aircraft rate.
Many naval aviators have complained that the engines on the older A-model F-14's are not powerful enough to perform the demanding aerial maneuvers they fly.
The Navy is replacing them with a more powerful engine that is now on about 30 percent of the fleet's F-14's. Fighter Squadron 213 flies all A-model F-14's. In the latest accident, the twin-engine, two-seat Tomcat crashed shortly after takeoff from Berry Field, an Air National Guard airfield adjacent to Nashville International Airport.
The jet left Miramar Air Station in San Diego for Nashville on Friday on a routine training mission.
Bennit said on Tuesday that Navy officials approved Bates' request to use a maximum-performance takeoff, in which a pilot turns on the jet's after-burner and soars straight up moments after the aircraft leaves the ground.
After screaming up through the clouds, the F-14 then came straight down exploding into a huge fireball.

Figure 2. Highlighted extracted and ground truth entities.

Probabilistic Characterization of Adversary Behavior in Cyber Security

Carol A. Meyers
(925) 422-1252
meyers14@llnl.gov

Cyber defense is a vast and growing problem in national security. According to the FBI, the annual loss due to cyber crime was estimated at $67.2 billion for U.S. organizations in 2005. Numerous efforts have sought to quantify the impacts of cyber crime, but much less work has focused on characterizing the cyber adversaries themselves. Given that cyber security is such a huge problem, in the construction of a defensive architecture it is essential to know who the cyber adversaries are and what threats they are likely to attempt.

This effort aims to provide a probabilistic characterization of adversary behavior in cyber security, in terms of *who* is perpetuating the attacks and *what methods* they use. The primary data source obtained for this project was a set of unfiltered email data, from a selection of addresses at ciac.org, the former Computer Incident Advisory Capability (CIAC) at LLNL. In addition, we performed an extensive review of the literature in cyber security to address attack vectors for which we were not able to obtain real data.

Project Goals

The objective of this project was to characterize the types of adversaries and attack methods associated with real cyber data, focusing in particular on email as an attack vector. There were three main quantitative thrust areas, centered on analysis of the CIAC dataset: 1) characterization of textual email data; 2) characterization of viruses present in attachments; and 3) characterization of malicious URL content.

The first of these addresses the descriptive content of the emails themselves, such as the volume over time, countries of origin, and methods of spoofing the header data. The second area examines the content of the email attachments, using a suite of antivirus programs to scan the emails and catalogue the kind and frequency of attacks. The third thrust area characterizes the content of web addresses embedded as URLs within the emails (Fig. 1), using custom scripts to query four different online malicious URL detection sites. In the process, we are also able to gauge the relative efficacy of different antivirus and malicious URL detection tools.

Relevance to LLNL Mission

This work directly aligns with the adversary modeling roadmap within the Engineering Systems for Knowledge and Inference (ESKI) portfolio. In addition, it supports the Cyber, Space, and Intelligence mission area of the institutional Science and Technology Five-Year Roadmap to the Future. The capabilities established with this work can be used in future LLNL cyber security studies, particularly in terms of mapping the adversarial threat space. All of the software and tools used are thoroughly documented and available for use by interested parties.

Figure 1. Graphic showing malicious URLs directing users from emails to websites hosting malware content.

FY2009 Accomplishments and Results

The email data used in our characterization was sent between February 2004 and July 2009, with an average of approximately 4000 emails received per month. A reverse lookup of the originating IP addresses was performed to identify the most common associated countries (Fig. 2). China and the United States represented the largest percentage of the sample, followed by South Korea and Brazil.

In terms of the attack methods chosen, we observed that the use of email attachments as an attack vector has decreased sharply over time (Fig. 3). This decrease is probably because email servers have implemented stronger screening procedures and the threat space itself has shifted, due to the lower level of sophistication required to launch an attack using malicious URLs. The number of attacks using malicious URLs increased across the data sample, supporting this hypothesis. With regard to the attacks themselves, the majority of email attachments contained Windows viruses, while most malicious URLs were associated with viruses and drive-by downloads.

Our analyses identified several traits about the adversaries and trends in their behavior. We observed that of the top four countries in the sample, two countries (China and South Korea) also scored very high on maliciousness and low on the trustworthiness of associated emails, while the other two (the United States and Brazil) did not. We can therefore conclude that the largest number of malicious emails is connected with adversaries in Southeast Asia. We also observed that emails sent on weekends are statistically more likely to be malicious than emails sent on weekdays, and the time of day with the highest percentage of malicious activity is late afternoons and evenings.

Finally, we note that the different tools that we used produced dramatically different results. In terms of email attachments, only two of the six tested tools (Norton Antivirus and AVG free) found any threats at all. With respect to malicious URL detection, the Web of Trust tool tested many more domains than any of the other tools (McAfee Site Advisor, Norton SafeWeb, and Google SafeBrowse), and also detected threats in a significantly higher percentage of websites (Fig. 4).

Figure 2. Graphic showing most common countries of origin for emails in the dataset, by reverse IP address lookup. The darker the color intensity, the greater the number of emails received from that country.

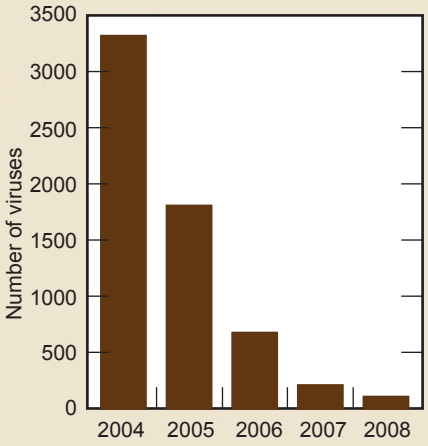

Figure 3. Graphic showing number of viruses identified in emails in the dataset, over time.

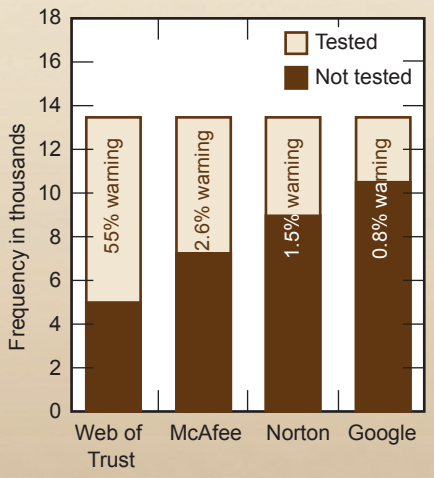

Figure 4. Graphic showing number of domains tested by each of the services, inset with the likelihood that the service generated a warning given a test.

Related References

1. Government Accountability Office (GAO), "Cybercrime: Public and Private Entities Face Challenges in Addressing Cyber Threats," *Technical Report GAO-07-705, U.S. Government Accountability Office*, 2007. Accessed at http://www.gao.gov/products/GAO-07-705.
2. Hansman, S., and R. Hunt, "A Taxonomy of Network and Computer Attacks," *Computers and Security*, **21**, pp. 31–43, 2005. Accessed at http://linkinghub.elsevier.com/retrieve/pii/S0167404804001804.
3. Lipson, H., "Tracking and Tracing Cyber Attacks: Technical Challenges and Global Policy Issues," *Technical Report CMU/SEI-2002-SR-009*, Carnegie Mellon University, 2002. Accessed at http://www.sei.cmu.edu/pub/documents/02.reports/pdf/02sr009.pdf.
4. Rantala, R., "Bureau of Justice Statistics Special Report: Cybercrime Against Businesses, 2005," *Technical Report NCJ 221943, U.S. Department of Justice*, 2008. Accessed at http://www.ojp.usdoj.gov/bjs/abstract/cb05.htm.
5. Rogers, M., "A Two-Dimensional Circumplex Approach to the Development of a Hacker Taxonomy," *Digital Investigation*, **3**, pp. 97–102, 2006.

Energy Manipulation

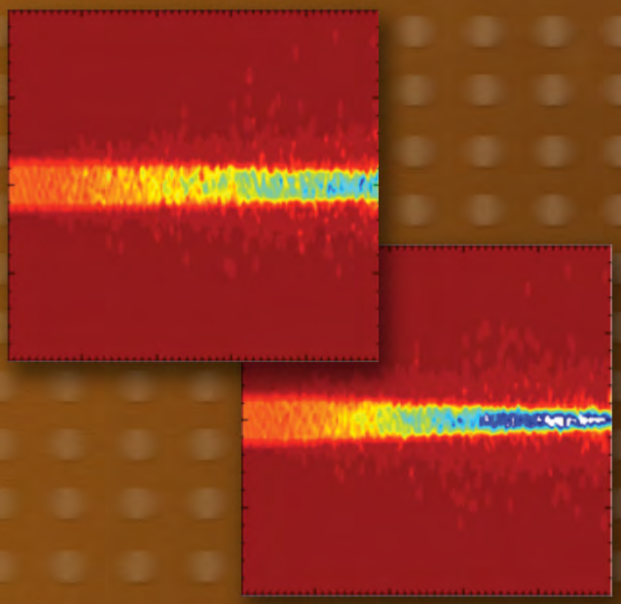

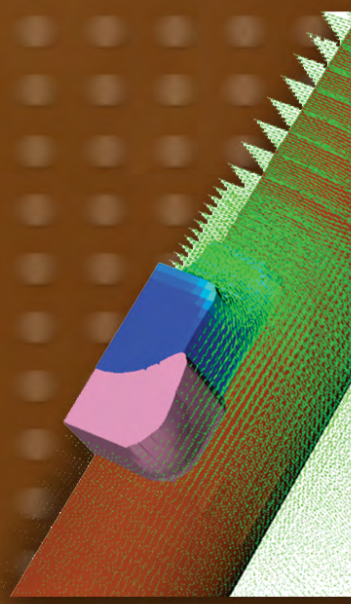

Ultrahigh-Velocity Railgun

Jerome M. Solberg
(925) 422-5971
solberg2@llnl.gov

Railguns have the theoretical potential to provide compact, repeatable acceleration of gram-sized projectiles to velocities significantly in excess of 10 km/s. However, the results from numerous experiments over the past 40 years show a perceived "velocity barrier" of 6 to 8 km/s.

This project aims to understand the physics behind this limitation using a combination of simulation and experiment, with the ultimate goal of proposing a concept that might overcome this barrier.

Project Goals

The project aimed to modify the 3-D coupled-physics code ALE3D such that it could model plasma and hybrid (solid/plasma) armature railguns, and use this tool to understand the physics. As a step in this direction, we constructed the Fixed Hybrid Armature experimental apparatus, comparing simulations to experiments in a sub-scale device. Finally, the project aimed to design and test a railgun with the potential to overcome the 8 km/s velocity limitation.

Relevance to LLNL Mission

A means to reliably launch gram-sized projectiles to velocities significantly in excess of 10 km/s is of great interest to the Laboratory for equation-of-state research. There remains a "gap" between high-energy states accessible primarily by lasers such as NIF, and lower energy states accessible via gas guns (currently limited to ~8 km/s). In addition, there is continued interest from NASA and the DoD for such a device as a kinetic energy weapon, for simulating asteroid impacts on space vehicles, and space launch.

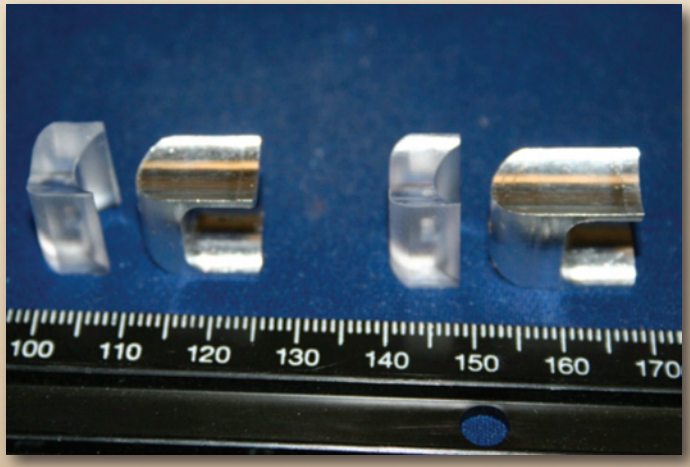

Figure 1. Launch package designs for novel ultrahigh-velocity railgun.

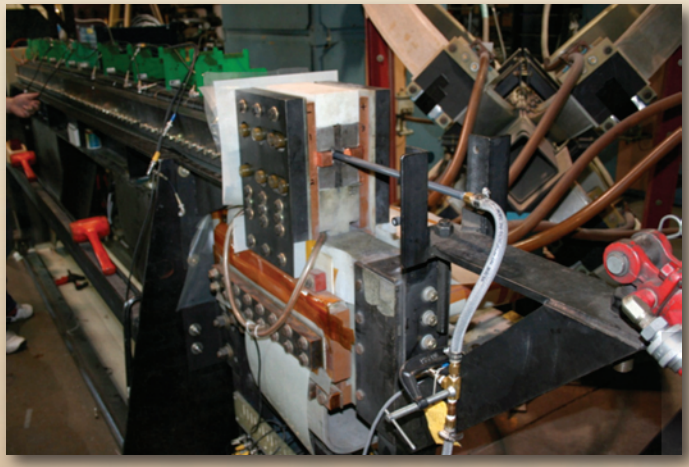

Figure 2. Novel ultrahigh-velocity railgun ready to fire. The hose connection provides the vacuum to the breech end of the internal railgun structure.

FY2009 Accomplishments and Results

Over the course of three years we modified ALE3D to include significant plasma physics and electromagnetics, including radiation heat transfer. These capabilities have been demonstrated on simulations of both the Fixed Hybrid Armature and full 3-D plasma-armature railguns. We have identified the remaining primary deficiency as radiation heat transfer in nearly transparent regions, which is being remedied through a related project. Through a combination of simulation and theory we identified a concept for a railgun using a hybrid armature (solid body with plasma brushes) that could overcome the velocity barrier, and built and tested a prototype. Unlike its predecessors, this railgun was designed to operate in hybrid mode throughout the launch process, using the concept of a barrel without sidewalls to eliminate insulator ablation. The accelerating armature was designed to lose significant mass throughout the acceleration process as a result of plasma-arc induced erosion, while maintaining acceleration.

The results of these experiments indicate that the projectile was able to operate in hybrid-mode past 4 km/s, even though more than 50% of the armature mass had been lost. Again in agreement with the design intent, the armature was able to operate at more than twice the theoretical "gouging velocity" without gouging the rails. The existing railgun facilities used for the test (IAP Research, Dayton OH) were not capable of operating at pressure levels less than 1 Torr without additional hardware, which was beyond the scope of the initial investigation. Larger sustained levels of breech voltage (and hence higher velocities) were found to be obtainable at higher pressures (lower levels of vacuum), indicating that for operation at pressures on the lower side of the Paschen minimum (70 mTorr or less) the inter-rail standoff voltage can be increased to levels that could sustain significantly greater velocities. The ultimate goal is to augment the magnetic field with an external circuit, thus reducing the required armature current and standoff voltage, and allowing for pure hybrid-mode to be sustained to velocities > 10 km/s.

Figures 1 through 4 illustrate our system and results.

Related References

1. Hawke, R. S., *et al.*, "Summary of EM Launcher Experiments Performed at LLNL," *IEEE Trans. on Magnetics*, **22**, 6, pp. 1510–1515, 1986.
2. Hawke, R. S., *et al.*, "Railgun Performance with a Two-Stage Light-Gas Gun Injector," *IEEE Transactions on Magnetics*, **27**, 1, pp. 28–32, January 1991.
3. Ostashev, V. E., *et al.*, "Velocity Limits in Plasma Armatures," in High Velocity Acceleration of Macrobodies: Theory, Practice and Perspectives, A. S. Anshakov and A. I. Fedorchenko, Eds., NOVA Science Publishers, Inc., New York, New York, 1995.
4. Parker, J. V., "Why Plasma Armature Railguns Don't Work (And What Can Be Done About It)," *IEEE Trans. on Magnetics*, **25**, 1, pp. 418–424, 1989.
5. Tang, V., J. M. Solberg, T. J. Ferriera, *et al.*, "Compact Collimated Fiber Optic Array Diagnostic for Railgun Plasma," *Review of Scientific Instruments*, **80**, 1, January 2009.

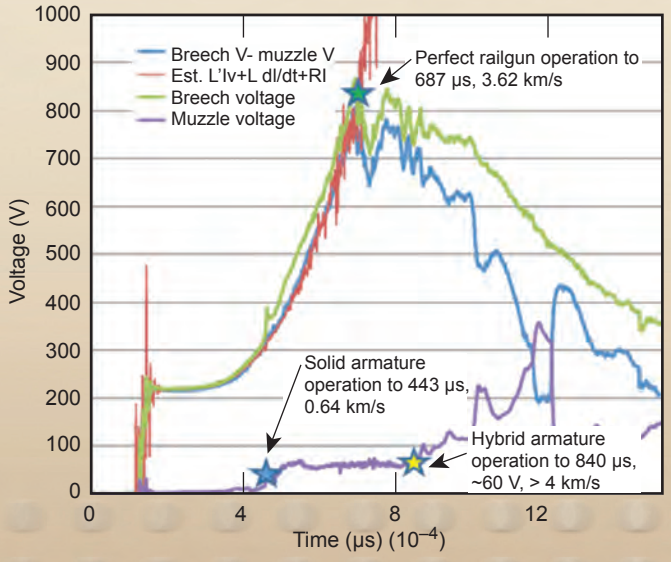

Figure 3. Plot illustrating hybrid mode operation past 4 km/s with low value of muzzle voltage and perfect railgun operation even with significant mass lost from the armature.

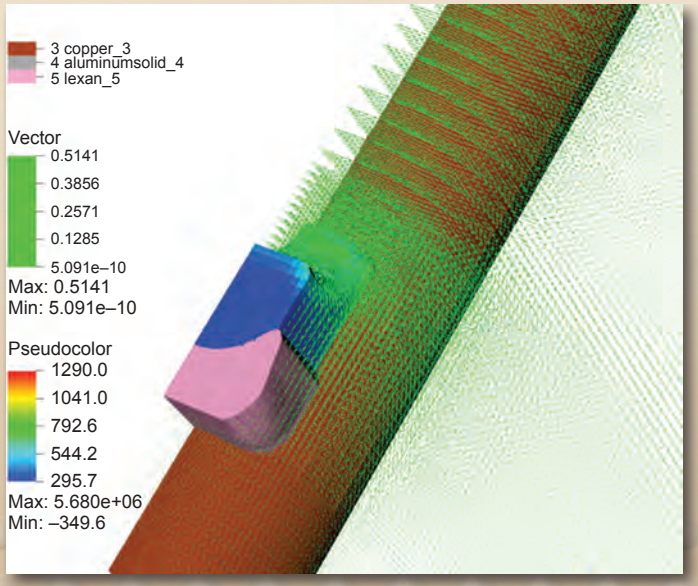

Figure 4. Novel ultrahigh-velocity railgun modeled by ALE3D. Solid armature mode before transition; armature beginning to melt near the trailing edge.

Vacuum Insulator Flashover

Timothy L. Houck
(925) 423-7905
houck1@llnl.gov

High-performance pulsed-power systems are used in numerous applications related to national security. The vacuum insulator is a critical component of such systems, often limiting peak performance. If designed incorrectly the insulator can be the weak link leading to failure of the entire system. Scientific knowledge developed from simple experiments provides understanding of important physics involved in insulator performance, but is not readily translated into a reliable tool for predicting operational performance. We are developing a computer model of electrical breakdown at the dielectric/vacuum interface. We are leveraging LLNL's advances in computational resources to bridge the gap between knowledge and application.

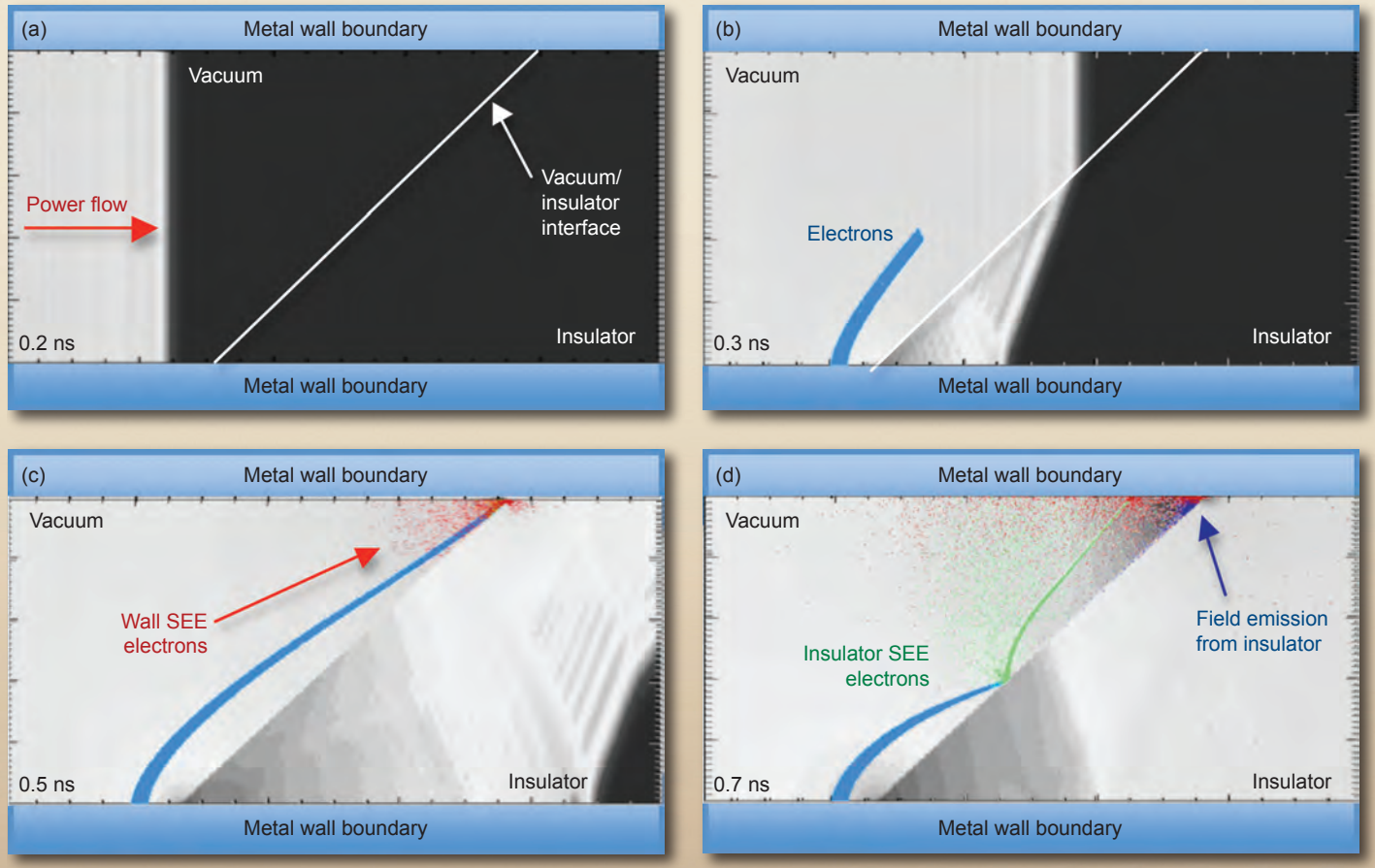

Figure 1. Power flow channel simulated with VORPAL. (a) Electromagnetic power flows from the left passing through a 45° angled insulator. The grey scale background indicates the relative strength of the electric field (white is high; black is zero). (b) Shortly before 0.3 ns simulation time, electrons (light blue) are emitted from a small area of the wall as a hypothesized perturbation. (c) These electrons cross the vacuum and are swept across the opposing wall producing secondary electrons (red). (d) At later times the emitted electrons strike the insulator, producing additional secondary electrons (green) and charging the insulator. This charging attracts the emitted electrons. Also, high fields near the upper face of the insulator cause field emission from the insulator (blue).

Project Goals

We wish to produce a computational methodology for designing high-voltage vacuum insulators for pulsed-power devices. We expect to demonstrate that a few basic physics phenomena are responsible for the initiation of electrical breakdown across the dielectric/vacuum interface, known as vacuum insulator flashover. Varying the geometry, materials, and environment used in simulations will show how different initiation mechanisms evolve. This tool will make it possible to study complex insulator designs in realistic operational applications and to predict performance. We will also deliver a proposed insulator design for the next generation of magnetic flux-compression generators.

Relevance to LLNL Mission

This project directly supports the Energy Manipulation pillar of the Science, Technology, and Engineering foundation. Our computational model enhances LLNL's status as a world-class center for high-voltage vacuum insulator design, development, and testing. Improved vacuum insulators will have immediate impact on explosively driven flux compressors and compact accelerator designs.

FY2009 Accomplishments and Results

A commercial 3-D, fully electromagnetic Particle-in-Cell (PIC) Code, VORPAL, was acquired and installed on an LLNL Linux cluster. We modified the source code of the Secondary Electron Emission (SEE) model for our application. This phenomenon produces electrons from a surface due to impact by incident electrons. If more electrons emerge from the surface than impact, an avalanche of electrons can be formed. For the materials of interest, this avalanche is considered one of the principle mechanisms of flashover.

A power flow channel simulated with VORPAL is shown in Fig. 1. The power enters from the left and passes through the insulator. Field emission from a small area of the metal wall boundary introduces electrons into the simulation. The magnetic field associated with the electromagnetic pulse bends the orbits of electrons, leading to impacts with the insulator. SEE occurs both on the insulator and on the metal wall. This simulation emphasizes several issues of flashover. The most important is the effect of SEE in generating an electron avalanche.

Next is the effect of the self-consistent magnetic field on the orbits of the electrons. For a electromagnetic power flow, both electric and magnetic fields will be present. Past design of insulators has often been accomplished with electrostatic modeling, neglecting the magnetic field. In low power flow systems this is a legitimate technique, but for high power systems important phenomena such as self-magnetic insulation will be overlooked.

Finally, although not apparent in the figure, the total current across the insulator is not sufficient to cause a complete voltage collapse. The final stage of flashover must involve plasma production in a desorbed gas layer on the insulator surface. Such a layer has been experimentally observed. Neutral gas ionization studies (Fig. 2) have started by simulating the propagation of an electron beam through argon and the resulting collisional ionization.

Related References

1. Perkins, M. P., T. L. Houck, J. B. Javedani, G. E. Vogtlin, and D. A. Goerz, "Progress on Simulating the Initiation of Vacuum Insulator Flashover," *Proc. 17th IEEE International Pulsed Power Conference*, 2009.
2. Nieter, C., and J. R. Cary, "VORPAL: a Versatile Plasma Simulation Code," *J. Comp. Phys.*, **196**, pp. 448–472, 2004.

FY2010 Proposed Work

The effect of electron interactions with a desorbed neutral gas will be the major focus area in the coming year. Water has been identified as a leading contaminate in vacuum systems. A self-consistent gas desorption model will be incorporated into the code. A desired goal is to determine an improved insulator through simulations and design a laboratory experiment to validate our results.

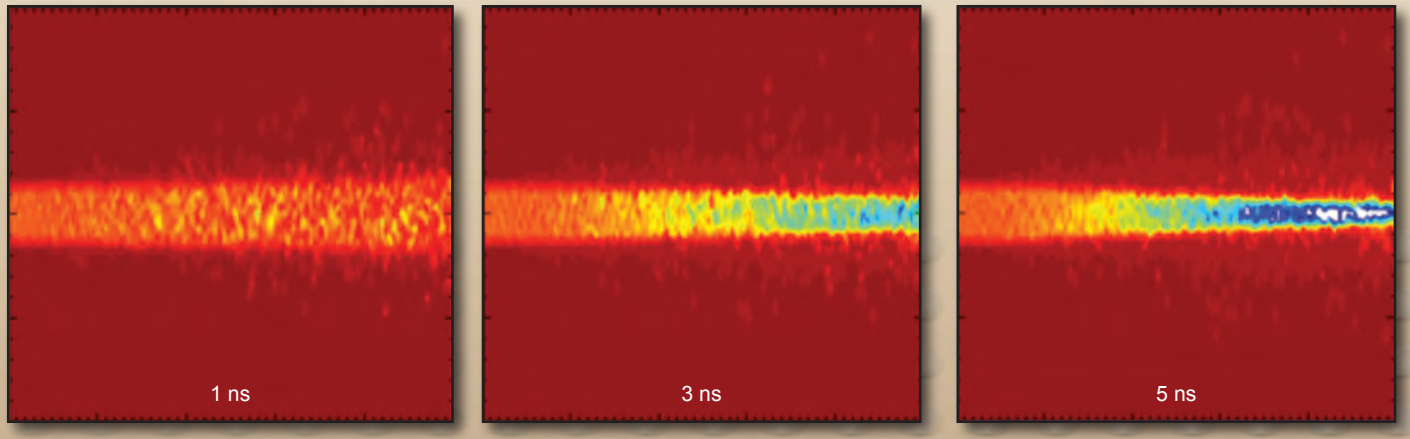

Figure 2. Simulation showing the effect of an energetic electron beam entering a volume of argon, ionizing the gas from the left. The color scale shows the current density with white high, red low. As time elapses the argon ions in the beam path focus the beam into a high density channel.

Author Index

Manuscript Date April 2010
Distribution Category UC-42

This work was performed under the auspices of the U.S. Department of Energy by Lawrence Livermore National Laboratory under Contract DE-AC52-07NA27344.
ST-09-0072

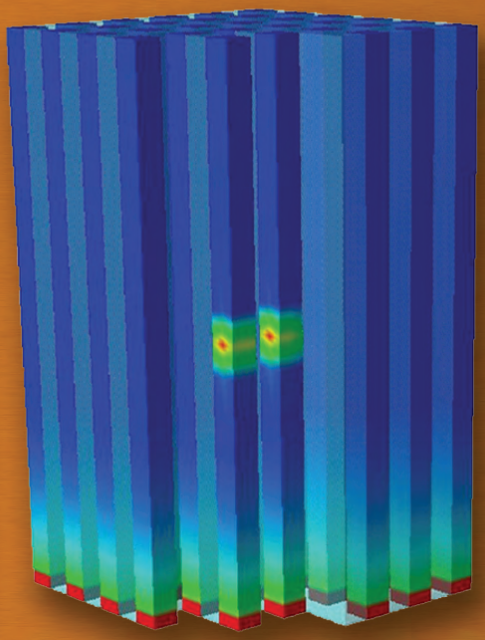

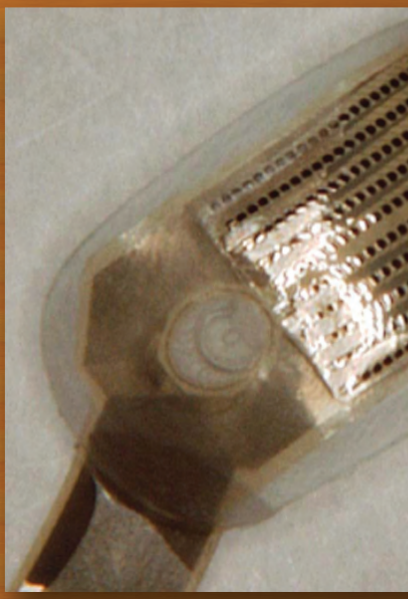

ENGINEERING
Lawrence Livermore National Laboratory
PO Box 808, L-151
Livermore, CA 94551-0808
http:www-eng.llnl.gov/